Impurity Diffusion in Single Crystal Zinc Oxide

Thomas Neset Sky

January 24, 2019

Thesis submitted for the degree of Philosophiæ Doctor

© Thomas Neset Sky, 2019

Series of dissertations submitted to the
Faculty of Mathematics and Natural Sciences, University of Oslo
No. 2075

ISSN 1501-7710

All rights reserved. No part of this publication may be
reproduced or transmitted, in any form or by any means, without permission.

Cover: Hanne Baadsgaard Utigard.
Print production: Reprosentralen, University of Oslo.

Dedicated to my late supervisor,
Bengt G. Svensson

Abstract

The diffusion of the impurities aluminum (Al), gallium (Ga), indium (In) and lithium (Li) in single crystal zinc oxide (ZnO) is studied by secondary ion mass spectrometry (SIMS) and positron annihilation spectroscopy (PAS). The experimental results reveal that the diffusion of the n-type dopants Al, Ga and In depends strongly upon the Fermi-level position with diffusion coefficients that depends quadratically on the dopant concentrations. The results strongly suggest that the diffusion of all these group III elements is mediated by double negatively charged zinc vacancies (V_{Zn}^{2-}) forming temporary dopant-vacancy pairs with a single negative charge. The diffusion of Li, on the other hand, is demonstrated to be highly controlled by the concentration and distribution of Ga, in Ga-doped ZnO, and a dissociative donor-vacancy assisted diffusion mechanism is proposed based on comparison between experimental and theoretical results using density functional theory (DFT).

A quadratic relationship is established between the Al-doping and the V_{Zn} concentration in Al-doped ZnO using direct observations by SIMS and PAS measurements. It is further demonstrated that the diffusion characteristics of Al is strongly affected in the presence of an increased background concentration of Ga, producing free-diffusion like behaviour, that is related to an effectively inexhaustible supply of mediating V_{Zn} at such conditions. Furthermore, the experimental diffusion results are compared with recent theoretical results (DFT-calculations) using a novel reaction-diffusion model. This method provides excellent agreement between experiment and theory and enables the extraction of detailed information concerning the impurity-defect microscopic interplay.

The experimental results unambiguously show that one of the most commonly used ZnO-based transparent conductive oxides (Al-doped ZnO) is accompanied by compensating V_{Zn}^{2-}, and it is further demonstrated that these compensating centers can be effectively removed by thermal treatment in zinc-rich ambient.

Acknowledgements

It has been over 6 years since Bengt G. Svensson introduced me to the field of semiconductor physics and accepted me as one of his students. I really do miss those discussions on diffusion problems we had in his densely packed and well-organized office, that could sometimes last for quite some time. Not to mention the surprisingly effective moments next to the coffee machine. Bengt really did devote time for his students, and his knowledge truly seemed unlimited. Thank you Bengt.

I especially want to thank my main supervisor Lasse Vines and my supervisor Klaus Magnus Johansen for guiding me through this endeavour. The attention you have given me on a day-to-day basis has been essential for this work. Your vast experience and knowledge in this field has made my days very enjoyable and stimulating. The best moments during my time here have undoubtedly been the round-table discussions we've had on fresh experimental results. I continue to be fascinated by your ideas and reasoning, and I am convinced that 'Light and Electricity from Novel Semiconductors' (LENS) will continue to flourish with your presence.

There are many to thank that has contributed to realizing this work. I would like to thank Ymir K. Frodason for the valuable discussions we've had on a more theoretical basis, and for your important contributions to the theoretical results of this work. Thank you Heine N. Riise for depositing the many different ZnO-doped thin films over the years. I would like to thank Filip Tuomisto, Vera Prozheeva and Natalie Segercrantz for your assistance and an enjoyable time with positrons at Aalto University, Finland. Thank you Thomas Aarholt and Øystein Prytz for the STEM analysis. Viktor Bobal knows how to fix just about everything in the lab, and your support in keeping the SIMS running has been instrumental for this PhD work. Thank you.

Finally, a big thanks to everyone at LENS for making this time a very enjoyable period in my life.

Publications

Appended papers

I. T. N. Sky, K. M. Johansen, H. N. Riise, B. G. Svensson, and L. Vines, *Gallium diffusion in zinc oxide via the paired dopant-vacancy mechanism*, Journal of Applied Physics 123, 055701 (2018)

II. T. N. Sky, K. M. Johansen, V. Venkatachalapathy, B. G. Svensson, F. Tuomisto and L. Vines, *Influence of Fermi-level position on Vacancy-Assisted Diffusion of Aluminum in Zinc Oxide*, PHYSICAL REVIEW B 98, 245204 (2018)

III. T. N. Sky, K. M. Johansen, Y. K. Frodason, H. N. Riise, B. G. Svensson, and L. Vines, *Diffusion of Indium in Single Crystal Zinc Oxide: a Comparison between Group III Donors*, Semicond. Sci. Technol. 34 025011 (2019)

IV. T. N. Sky, K. M. Johansen, Y. K. Frodason, B. G. Svensson, and L. Vines, *The Interaction between Lithium Acceptors and Gallium Donors in Zinc Oxide*, J. Appl. Phys. 124, 245702 (2018)

V. H. N. Riise, V. S. Olsen, A. Azarov, A. Galeckas, T. N. Sky, B. G. Svensson, and E. Monakhov, *Local homoepitaxy of zinc oxide thin films by magnetron sputtering*, Thin Solid Films, 601 (2016)

Papers not appended

F. Herklotz, K. M. Johansen, A. Galeckas, T. N. Sky and B. G. Svensson, *The influence of Fe impurities on the annealing of OHLi complexes in ZnO*, Physica status solidi. B, Basic research, 253(2) (2016)

S. Grini, N. Ross, T. N. Sky, C. Persson, C. Platzer-Bjørkman, and L. Vines, *Secondary ion mass spectrometry as a tool to study selenium gradient in* $Cu_2ZnSn(S,Se)_4$, Physica Status Solidi. C, Current topics in solid state physics, 14 (2017)

C. Zimmermann, J. Bonkerud, T. N. Sky, A. Hupfer, E. Monakhov, B.G. Svensson, L. Vines, and F.Herklotz, *Electrically-active defects in rutile* TiO_2 *studied by space-charge spectroscopy*, Journal of Applied Physics 123, 161572 (2018)

Contents

Acknowledgements **iii**

Publications **v**
Appended papers v
Papers not appended v

1 Introduction **1**

2 Zinc Oxide **5**
2.1 Single crystal growth 5
2.2 Crystal structure, fundamental properties and the bipolar problem 7
2.3 Transparent conductive properties 10

3 Impurity diffusion in solids **13**
3.1 An historical prelude 13
3.2 Phenomenological approach 14
3.3 Point defects and diffusion mechanisms 16
3.4 Diffusion coefficient 19
3.5 Isoconcentration diffusion 23
3.6 Reaction diffusion model 24
3.7 Impurity diffusion in ZnO: A brief review 27

4 Characterization techniques **35**
4.1 Secondary Ion Mass Spectrometry 35
4.1.1 Rationale 35
4.1.2 Sputtering 37
4.1.3 Analysis 38
4.1.4 Quantification 39
4.2 Positron Annihilation Spectroscopy 40
4.2.1 Rationale 40
4.2.2 Doppler broadening spectroscopy 42

5 Results **45**
5.1 Summary of appended papers 45
5.2 Preliminary results 48
5.2.1 Diffusion of Ga in Al-doped deposited thin films 48
5.2.2 Diffusion of Al under varied background levels of dopants 49
5.2.3 Diffusion of In under increased donor background concentration 50
5.3 Suggestions for further work 51

A Density functional theory **53**

B Thin film growth by sputter deposition **55**

C Scanning Transmission Electron Microscopy **57**

References **59**

Paper I **71**

Paper II **79**

Paper III **89**

Paper IV **97**

Paper V **105**

Chapter 1

Introduction

Semiconductors have been studied since the early nineteenth century, after it was observed an interesting and anomalous temperature dependence of the electrical conductivity for these solid materials [1]. It had been discovered that upon heating a semiconductor the electrical conductivity increased, which is the opposite of what had already been established for metals. However, it was not until the arrival of quantum theory of solids in the early 1930's [2] that this phenomenon could be fully explained as being caused by an exponential increase in the number of charge carriers with increasing temperature. About two decades later, the first germanium transistor was born, an event that can be considered as a start signal for the great semiconductor adventure that should result in increased human well-being, with improved communication, energy availability, productivity and health, to name a few.

The study of diffusion in semiconductors has played a significant role in the development of the fundamental understanding of these materials, and thus the realization of semiconductor-based devices. The diffusion of atoms in a crystal structure, may it be host species or impurities, is often mediated by intrinsic material related defects, such as vacant lattice sites or misplaced interstitial atoms. It is therefore possible by monitoring the diffusion of an impurity species to deduce valuable information about intrinsic defects that otherwise may be challenging or practically impossible to observe. Moreover, diffusion is essential for semiconductor processing, enabeling introduction of desired atoms or removal of undesired contaminants. To succesfully control atomic diffusion, means to describe the experimentally observed behaviour by any predictive model. As a first approximation, diffusion can be well described in a phenomenological manner by considering some of the transport laws of physics. However, in many cases, and especially in the case for impurity diffusion in semiconductors, this description does not hold,

and thermodynamical considerations are necessary to understand the microscopic interplay. That is, a more physical and atomistic approach to diffusion can be made by using a model that takes into account the microscopic interactions of all the species contributing to the process. In this work, such an approach have been realized by a system of reaction-diffusion equations that explicitly takes into account the underlying mechanisms of diffusion.

Zinc Oxide is a semiconducting and transparent material that has many intriguing properties, such as a high exciton binding energy and is easily amenable to produce high n-type conductivity. Perhaps the first use of ZnO for its semiconducting properties was in 'build-your-own radio sets' in the 1920s, where a Schottky barrier was created between a copper wire and a ZnO crystal in order to convert incoming alternating current radio waves to direct current signals [3]. An increasing investigation of ZnO crystals followed in the years to come, and in the early 1950's temperature dependent Hall measurements of ZnO crystals demonstrated the inherence of the already observed n-type nature of ZnO [4]. In the transition to the 21st century, ZnO gained enormous attention due to its promising potential for obtaining a wide bandgap p-n homojunction [5, 6, 7]. Although short wavelength optoelectronic devices based on gallium nitride (GaN) did already exist, prospects of using readily available ZnO single crystals at comparably low cost, to that of GaN substrates, incentivized the research. However, achieving stable and reliable p-type ZnO has proven to be notoriously difficult, and is still absent today.

Nevertheless, ZnO being a transparent semiconductor with a direct bandgap of 3.4 eV [8] has attracted much attention for its use as an n-type transparent conductive electrode, with applications in power electronics as well as in thin-film solar cells. High n-type conductive ZnO is readily made by impurity doping using the group III elements aluminum (Al), gallium (Ga) and indium (In) [9], producing transparent conductive electrodes that are considered a viable alternative to the present industry standard using the more scarce/expensive tin-doped indium oxide for transparent conducting based applications. However, self-compensation effects is known to arise in highly n-type doped ZnO [10], although not fully explained, which pose a limit to its conductivity and competitiveness as a transparent conductive electrode.

The present work experimentally investigates the fundamental and microscopic behaviour of these group III n-type dopants in single crystal ZnO, and directly demonstrates how they affect inherent defects in the material. Further, an impurity that is often present in ZnO is lithium (Li), and is in this work demonstrated to be highly controlled by the distribution of Ga in Ga-doped ZnO. These results mainly relies on the experimental techniques secondary ion mass spectrometry (SIMS) and positron annihilation spectroscopy (PAS), but also theoretical results from

density functional theory (DFT) is considered and compared to the experimental results.

This thesis is organized as follows. Chapter 2 gives an introduction to crystalline ZnO, focusing on its fundamental properties, advantages and challanges. Chapter 3 gives a general introduction to the theory of impurity diffusion in solids, and continues with a more detailed discussion of diffusion in semiconductors, including a brief review of impurity diffusion in ZnO. Chapter 4 presents a detailed description of the measurement techniques utilized in this work, SIMS and PAS. Chapter 5 gives a summary of the main results of the appended papers, and present preliminary/unbublished results. The Appendices A-C consists of techniques that have been important for the work, but where the experimental/theoretical work have been conducted by peers. Appendix A gives a brief introduction of DFT as the experimental results of dopant diffusion has been compared with available results from DFT. Moreover, impurity doped ZnO films have been used as a diffusion source in this work, and Appendix B and Appendix C gives a short introduction to the techniques used to respectively grow (sputter deposition) and analyze (scanning transmission electron microscopy) these films.

Chapter 2

Zinc Oxide

The group II-VI binary compound semiconductor ZnO crystalizes in either zinc-blende, rocksalt or wurtzite structures. The zinc-blend structure can be obtained only by growth on cubic substrates, and the rocksalt structure may be achieved under high pressures. At ambient conditions, however, the thermodynamically stable phase is the hexagonal wurtzite structure. In this work, single crystals of wurtzite ZnO have been used as host material in the study of diffusion of different impurities in ZnO. Therefore, it is appropriate to start out with a brief introduction to the methods used to obtain ZnO single crystal wafers. Then, the fundamental properties of wurtzite ZnO will be presented, before the practical challenges and advantages for using ZnO as a transparent semiconductor is discussed.

2.1 Single crystal growth

Single crystal ZnO can be grown in a variety of ways by utilizing different growth mechanisms, resulting in bulk ZnO crystals grown at different rates and with differing crystalline quality and impurity content. The three primary methods for ZnO bulk growth are through the pressurized melt growth, vapour phase growth and hydrothermal solution growth.

Growth by the pressurized melt method employs a modified Bridgman process [11], where ZnO powder is heated to temperatures exceeding its melting point (1975°C) using radio frequency heating. Under normal atmospheric conditions ZnO decomposes at this high temperature, yielding a reduction and deficiency of oxygen, and an overpressure of oxygen is needed to ensure equilibrium between the liquid ZnO and the oxygen containing atmosphere. Controlled crystallization

of the melt is then acheived by slowly reducing the temperature. Growth rates as high as 5 mm/h for ingots up to 50 mm in diameter has so far been made by this method [12, 11]. However, low angle grain boundaries and considerable differences in the material quality over the ingot are induced from the temperature gradient between the crucible and melt.

The vapour phase growth method involves heating polycrystalline ZnO either to cause sublimation under vacuum or under some specific atmosphere causing reaction and/or transport of the gas phase before it is depositied on a seed crystal [12, 11]. The preferred method for ZnO is the seeded chemical vapour transport method, where a mixture of hydrogen and an inert gas as the athmosphere, which serves as transport agents, is used to increase the growth rate. The polycrystalline feed powder is heated to $1150°$C in one end of a reactor forming zinc and water vapour, which is then transported to a colder part of the reactor to be deposited onto the seed crystal. Excellent crystalline quality with a low level of impurities can be made by this method. However, the comparatively slow growth rate of about 1mm/day results in a high cost of the wafers [12].

In the present work, hydrothermally (HT) grown ZnO wafers have been the host material for all diffusion studies. In the conventional HT method an aqueous solution containing the solvent/mineralizer of LiOH and KOH are used under elevated temperatures ($300 - 400°$C) and pressure ($80 - 100$ MPa) to dissolve and recrystalize ZnO material of high purity [13]. Figure 2.1 shows the cross section of the autoclave used in the HT growth method. Due to the presence of the mineralizers, the sealed autoclave is fitted with a sealed Pt inner container, preventing the mineralizers to react chemically with the steel and leading to impurities in the ZnO crystal. The lower part of the autoclave (dissolution zone) is maintained at a slightly higher temperature than the upper part (crystal growth zone), resulting in convection transport of ZnO towards the seeds. A baffle separating the feedstock and the seed crystal is used to ensure a more constant mass flow. To enhance the ionic processes, the water is kept in its supercritical state where it shows an enhanced acidity.

The HT method is scalable and thus an industrially viable technique that shows excellent crystalline quality. However, significant amounts of unintentionally incorporated Li impurities are inevitably present for those methods that uses this compound as mineralizer. A slightly different scheme for producing HT grown ZnO have been demonstrated using other mineralizers [14, 15], thus producing ZnO crystals with Li concentration $< 10^{15}$ cm^{-3}, as compared to $\sim 10^{17}$ cm^{-3} for the conventional HT method. Detailed information about this process was not available, but the authors in [14, 15] claim that in using their method the inner container in a conventional HT system have been replaced with a low-cost autoclave

liner. The same method also demonstrate growth of Ga-doped ZnO using ZnO and Ga_2O_3 powder as the feedstock, resulting in a uniform Ga concentration of $\sim 10^{19}$ cm^{-3} with near to perfect substitution of Ga ions with Zn ions [15].

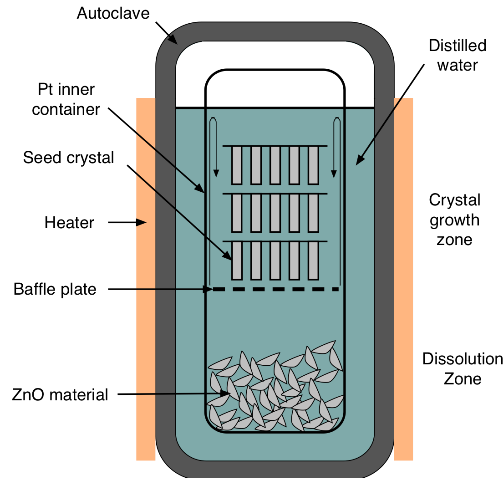

Figure 2.1: Schematic of the hydrothermal growth. Edited from [13].

2.2 Crystal structure, fundamental properties and the bipolar problem

At ambient conditions, ZnO favor a hexagonal wurtzite structure where each O ion is surrounded by four Zn ions at the corner of a tetrahedron, and vice versa, as illustrated in Fig.2.2. The lattice parameters describing the unit cell is given by a and b, with experimentally obtained values of 3.25 Å and 5.21 Å, respectively [5]. This gives a ratio $c/a = 1.603$, which deviates slightly from an ideal hexagonal closed packed structure ($\sqrt{8/3} = 1.633$). This distortion, together with the partly ionic nature of the bonds, results in a net dipole moment and cause ZnO to show a strong piezoelectric effect.

Each of the two atoms (Zn and O) contains a heavy nucleus surrounded by electrons that are bound to the nucleus by electromagnetic forces. Since two electrons cannot occupy the same state (Pauli exclusion principle [16]), this will result in electrons occupying different atomic orbitals. When a large number of Zn and O atoms come together to form a ZnO crystal, each of the atomic orbitals will split into many closely spaced energy levels, effectively forming a continuum/band of allowed levels [17]. It was the seminal work of Alan Wilson [2] in 1931 that

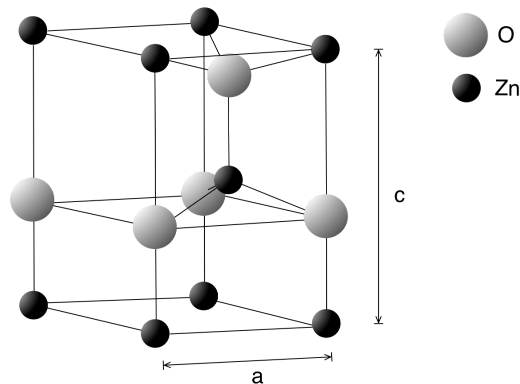

Figure 2.2: Wurtzite ZnO structure.

introduced the concept of band theory of solids, which enabled a fundamental understanding of semiconductors. Many such bands are formed, but the ones that determine the electrical conductivity are the two extremes: the valence band (VB) and the conduction band (CB), respectively representing the highest occupied and lowest unoccupied bands. For ZnO, the VB is composed of oxygen $2p$ orbitals and the conduction band is derived from zinc s orbitals, yielding a direct band gap of 3.4 eV [8].

The ability to conduct current depends on the number of available charge carriers. Charge transport can take place both by electrons in the CB or by holes (the absence of electrons) in the VB. If electrons are the main charge carriers, the semiconductor becomes n-type, and conversely, for holes being the main charge carrier this result in p-type material. To describe the electrical properties in a semiconductor, one considers a hypothetical energy level of an electron given by the Fermi-level position (ϵ_F) that have 50% probability of being occupied by an electron at any temperature. This means that in an n-type material ϵ_F is closer to the CB as compared to VB, and vice versa in p-type material. Importantly, the position of ϵ_F can be modified/controlled by introducing impurities that introduce shallow states in the material, i.e., close to either of the band edges, such that the impurity ionize at room temperature ($\sim$ 25 meV). Modulating the electrical properties of a semiconductor by intentional introduction of impurities is known as doping.

For ZnO, free/delocalized electrons are quite easily introduced by doping ZnO with heterovalent impurities like Al, Ga and In, producing highly conductive n-type material. P-type doping, on the other hand, is notoriously difficult. Within the scientific community of wide-band-gap semiconductors, ZnO is perhaps most known for its notorious p-type electrical conductivity problem. Stable and reason-

ably conductive p-type ZnO has not yet been achieved, and has undoubtedly intrigued and frustrated many materials scientists for decades. However, the p-type problem is not unique for ZnO. Oxides in general suffer from unipolar conductivity, with ZnO, Ga_2O_3, TiO_2, SnO_2 and In_2O_3 being inherently n-type, and Cu_2O inherent p-type-only.

The possibility to form p-n homojunctions in a semiconductor is necessary in order to produce competitive devices for e.g., light emission. Besides, the abundance of Zn and O together with the relative ease of large scale growth quality crystals, one can only imagine the huge number of viable technological opportunities such a triumph would have induced (e.g., opto-electronics, power and high-temperature electronics and solid state lighting).

The reason for the inherent n-type conductivity in ZnO has long been a controversial subject. From a fundamental perspective of the electronic structure, this asymmetry can be ascribed to the rather low position for the valance band maximum (VBM), as compared to the vacuum level [18]. This means that in order to provide holes into the valence band, an acceptor dopant with similar low-energy atomic orbitals as that comprising the valence band (oxygen $2p$-orbitals) is required. These are, apparently, not abundant.

Intrinsic defects, such as oxygen vacancies (V_O), have also been speculated to be the origin of the unintentional n-type conductivity [19]. This notion arised due to experimental observations that the electrical conductivity of as-grown ZnO was influenced by varying the oxygen partial pressure. On the other hand, more recent results conclude that V_O is a deep double donor [20, 21], and will thus not contribute to the free electron concentration at room temperature. Zn interstitials (Zn_i) is a shallow donor, but can also be ruled out as the source of the n-type conductivity due to its high formation energy in n-type ZnO and a quite low migration barrier ($0.55 - 0.70$ eV [22, 23]), ensuring out-diffusion even at room temperature.

Without any likely native defects to hold responsible, the focus has shifted to residual impurities incorporated in the crystal during growth that may affect the electrical properties. Common residual impurities in HT grown ZnO are hydrogen (H; $< 5 \times 10^{17}$ cm^{-3}), lithium (Li; $\sim 10^{17}$ cm^{-3}), silicon (Si; $\sim 10^{16}$ cm^{-3}) and aluminum (Al; 3×10^{15} cm^{-3}) [12]. H, Si and Al may all increase the n-type conductivity acting as shallow donors [12, 24], while Li has been shown to hold amphoteric behaviour, acting as a donor in compensated materials and as an acceptor in n-ZnO, residing on interstitial site and substituting for Zn, respectively [25, 26].

2.3 Transparent conductive properties

Transparent electrodes are an essential part of any flat-panel-display in our living rooms, as well as for touch-panels that can be found in most people's pockets. These electrodes are almost exclusively made of transparent conductive oxides (TCO's), i.e., oxide-based transparent and conductive semiconductors, and is largely dominated by indium-tin-oxide (ITO or Sn-doped In_2O_3). To be suitable for transparent electrode applications the TCO material should have a band gap above $\sim$ 3 eV and preferably an optical transmittance in the visible spectrum above 80%, with a free charge carrier concentration on the order of $10^{20} - 10^{21}$ cm^{-3} [27]. These characteristics can be obtained in donor-doped (B, Al, Ga and In) ZnO, and n-type ZnO has therefore been suggested as a viable alternative to ITO using abundant and inexpensive elements (see e.g., Minami *et al.* [28, 29]). Moreover, the low costs and the availability of large-scale deposition techniques (e.g., magnetron sputtering) for ZnO, have also given an incentive to use ZnO as a thin-film transparent electrode for improving the conversion efficiency of Si-based thin-film solar cells [30, 31, 32].

An early investigation by Minami *et al.* [9] of group III impurities in ZnO revealed that Al and Ga were more effective as n-type dopants ($2 - 5 \times 10^{-4}$ Ωcm) as compared to B (6×10^{-4} Ωcm) and In (8×10^{-4} Ωcm). Furthermore, a more recent study that compares Al- and Ga-doped ZnO report that Ga is more effective as an n-type dopant, as compared to Al [33]. This is corroborated by recent reports of the development of ZnO-based Liquid Crystal Displays (LCD), where Ga-doped ZnO thin films were demonstrated to yield comparable quality (although with slightly higher resistivity) to that of using conventional ITO based TCO's [34].

State of the art ZnO display a slightly higher resistivity to that obtained for ITO thin-films, and display also a higher thickness dependence of the resistivity, yielding a relative increase in resistivity for thinner films (typically below 200 nm) compared to that of ITO. Moreover, at elevated temperatures and in humid environments ZnO based TCO's reveal a higher instability of the resistivity [35, 36]. These issues should be controlled/understood in order to apply ZnO-based TCO's in devices.

It has previously been shown that highly Al- and Ga-doped ZnO are subject to self-compensation [10, 37, 38], resulting in an upper limit of the conductivity and thus reducing its applicability as a TCO. These sudies showed that V_{Zn} plays a role in the compensation, either as an isolated double acceptor or complexed with dopant impurities. In a more recent investigation of electron irradiated Al-doped ZnO, it was shown that $Al_{Zn}V_{Zn}$ is the prominent compensating defect in ZnO that

is thermally stable up to $250°$C [39, 40].

The formation of these donor-vacancy pairs, as well as their migration energetics and dissociative behaviour, have been explored in detail in this work and will be presented in Sec.5.1 and in the appended Papers I-IV.

Chapter 3

Impurity diffusion in solids

Impurity diffusion in semiconductors plays an important role in the realization of many technological applications. In the fabrication of microelectronic devices, controlled doping of the material is essential, and invariably involves the process of diffusion. Furthermore, the atomic mechanisms of impurity diffusion are often mediated by intrinsic point defects such as vacancies and self-interstitials. This implies that an understanding of impurity diffusion may also provide information of fundamental properties of the semiconductor. This chapter starts out with a discussion of diffusion in solids in general, before Sec.3.4 introduce the concept of charged point defects and thus turn the focus to semiconductors and ZnO in particular.

3.1 An historical prelude

The diffusion of impurities in solids has been practised since ancient times, with blacksmiths hardening iron through the diffusion phenomena of carbon (steel), albeit unaware of the underlying physics. This was long before diffusion had even been discovered as a phenomenon in the more easily observable substances, gases and liquids. The science of diffusion emerged in the early nineteenth century, with Thomas Graham's systematic studies of diffusion in gases and liquids. It was these experiments that inspired Adolf Fick to develop the mathematical framework a few decades later, as outlined in section 3.2. Another few decades later, William Chandler Roberts-Austen, a personal assistant of Graham, conducted for the first time a systematic study of solid-state diffusion: gold in solid lead. It was, however, not until Albert Einstein's interpretation of Brownian motion that the

atomistic approach of diffusion in general was born. Still, the birth of the atomistic framework of diffusion in solid materials emerged first after Max von Laue detected diffraction of X-rays in crystals in 1912. Shortly after, the concept of disorder in solid-state physics was introduced by Frenkel and Schottky (names that we will meet upon later in this chapter) to suggest that atomic defects are important for diffusion in crystals. This was soon supported by a simple interdiffusion experiment by Ernest Kirkendall, demonstrating a vacancy diffusion mechanism, and it was not long before this view was accepted over the original perceptions of direct exchange or ring mechanisms. For an enjoyable and thorough review of the history of diffusion, the reader is recommended "Heroes and Highlights in the History of Diffusion" by H. Mehrer and N. A. Stolwijk [41].

3.2 Phenomenological approach

The diffusion of an impurity A in a solid in one dimension can usually be described via the following relation between the diffusion flux J_A and the gradient of the concentration C_A of the impurity A:

$$J_A = -D_A \frac{\partial C_A}{\partial x}, \tag{3.1}$$

where D_A is the diffusion coefficient of impurity A expressing the amount of particles diffusing through a unit area in unit time (often given in cm^{2}s^{-1}) and x is the position. Equation (3.1) is known as Ficks first law of diffusion and was postulated based on the analogy with the Fourier heat equations and subsequently verified in a rather simple experiment using table salt in water [41].

Assuming that the species are conserved in the diffusion process, the rate of change in the concentration is then given by the flux:

$$\frac{\partial C_A}{\partial t} = \frac{\partial}{\partial x}(-J_A) = D_A \frac{\partial^2 C_A}{\partial x^2}, \tag{3.2}$$

where t is the time. Equation (3.2) is known as Fick's second law, and is expressed here assuming a position and concentration independent diffusivity. Rather than being driven by chemical gradients, it would arguably be more reasonable to assume that the diffusion is driven by gradients of free energy. That is, to minimize the free energy. A formulation of such thermodynamical consideration of diffusion can be found in Ref.[42], and from this a generalization of Fick's laws (i.e., for a chemical potential dependent flux) can be derived.

The diffusion model given by (3.2) is a second order linear partial differential equation, and both initial and boundary conditions are required for analytical solutions. There exists many analytical solutions to (3.2), which can be found in e.g., Ref.[43], for various boundaries and initial conditions. In particular, two different solutions that often find relevance in analysis of experiments are the 'finite source' and 'constant source' models. For both solutions it is assumed that the diffusion occurs in a semi-infinite sample, with an initial concentration of the diffusing species at $x = 0$ that is either finite or constant. In the case of a finite source of the diffusing species, the concentration after time t is described by

$$C_A(x,t) = \frac{M}{\sqrt{\pi D_A t}}\text{exp}\Big(-\frac{x^2}{4D_A t}\Big), \tag{3.3}$$

where M is the atoms per unit area. On the other hand, if the concentration at $x = 0$ is maintained at a constant concentration C_s, the solution of (3.2) is

$$C_A(x,t) = C_s\text{erfc}\Big(\frac{x}{2\sqrt{D_A t}}\Big), \tag{3.4}$$

where erfc is the complementary error function. Figure 3.1 compares the two diffusion models given in (3.3) and (3.4) for a given set of values of D_A and t.

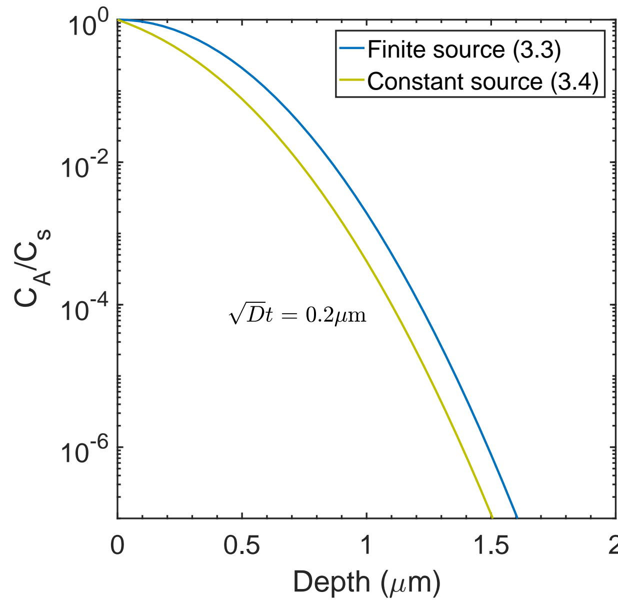

Figure 3.1: Comparison of the concentration vs depth profiles of the finite source and constant source diffusion models, as given in (3.3) and (3.4), respectively.

3.3 Point defects and diffusion mechanisms

By definition, a point defect in a crystal is an entity that causes an interruption in the lattice periodicity [44]. From statistical thermodynamics it is predicted that for any temperature T above 0 K, a crystal structure under thermal equilibrium will contain a finite concentration of point defects, as this disordering minimizes the Gibbs free energy (G) of the crystal. Accordingly, the equilibrium concentration of any given point defect X can be expressed as [45]

$$C_X = C_s \theta_X \, e^{(-G_X^f/k_B T)} = C_s \theta_X \, e^{(S_X^f/k_B)} e^{(-H_X^f/k_B T)}, \tag{3.5}$$

where C_s is the number of available lattice sites, θ_X accounts for the internal degrees of freedom of the point defect (e.g., $\theta_X = 1$ for monovacancies while it typically take a higher value for an interstitial, due to the various possible interstitial positions per lattice site), S_X^f is the formation entropy attributed to lattice vibrations, H_X^f is the enthalpy of formation, $k_B = 8.617 \times 10^{-5}$ eV/K [46] is the Boltzmann constant and T is the temperature in Kelvin.

The simplest form of point defects are often the most prevailing ones, and arguably the most understood. They include (i) a vacant lattice site (vacancy), (ii) a host atom displaced from its regular substitutional lattice site (interstitial) or (iii) an impurity occupying substitutional or interstitial site. The vacancy can be formed by two different mechanisms, from a surface (Schottky process) or by the dissociation of a substitutional atom into an interstitial, thus leaving behind a vacancy (Frenkel process). For interstitials, in addition to the Frenkel process, they may also similarly be formed by the Schottky process by removing an atom from the surface and moving it into the interstitial position of the crystal.

It is well known that native point defects play a crucial role in the diffusion of impurities, in particular for ionized impurities (dopants). Given the inherent presence of point defects, and provided that at least one of them is mobile at a given T, the mobile defect may be able to assist the migration of an otherwise stationary atom. For instance, assume that at a given T an impurity (A) on a substitutional site is unable to move via direct exchange with a neighboring atom, while the native vacancy (V) and self-interstitial (I) are mobile. Then, the following reactions may take place to produce mobile impurity species:

$$\mathrm{V} + \mathrm{A} \rightleftharpoons \mathrm{AV} \tag{3.6a}$$

$$\mathrm{I} + \mathrm{A} \rightleftharpoons \mathrm{A_i} \text{ or } \mathrm{AI} \tag{3.6b}$$

$$\mathrm{A} \rightleftharpoons \mathrm{V} + (\mathrm{A_i} \text{ or } \mathrm{AI}), \tag{3.6c}$$

Where AV and AI are the impurity point defect pairs, and A_i is the impurity in an interstitial position. The first reaction represents vacancy mediated diffusion. The

second reaction represents diffusion via interstitials, and it may occur either by forming a mobile AI pair or by a kick-out mechanism to form a mobile isolated A_i. The last reaction is known as a dissociative reaction and is a competing process to the kick-out reaction (b) for diffusion via mobile interstitials. In this work, we show that the diffusion of the impurities Al, Ga and In in ZnO can be explained by (3.6a), while the diffusion of the smaller impurity Li can be explained by (3.6b) and (3.6c).

The model given in (3.2) is generally adequate for describing impurity diffusion under low impurity concentration conditions. For semiconductors, however, as the dopant concentration increases to or above the intrinsic carrier concentration n_i of the semiconductor, Fick's second law with a constant diffusion coefficient often fails. At such extrinsic conditions it is beneficial to consider the detailed defect interplay between the impurity and the crystals native defects, as outlined in the reactions (3.6) above. If we in the following (for simplicity) only consider reaction (3.6a) and make the assumption that all impurity diffusion occurs through the formed AV pair, that is, A is considered immobile, we can write the following continuity equation for the concentration of AV pairs as

$$\frac{\partial C_{AV}}{\partial t} = D_{AV}\frac{\partial^2 C_{AV}}{\partial x^2} - \frac{\partial C_A}{\partial t}, \tag{3.7}$$

where

$$\frac{\partial C_A}{\partial t} = k_A C_{AV} - k_{AV} C_V C_A \tag{3.8}$$

expresses the reaction (association and dissociation) between A and V, and where C_A, C_{AV} and C_V are the concentration of substitutional impurities, impurity-vacancy pairs and vacancies, respectively. The term k_A in (3.8) is a reaction rate constant that represents the dissociation rate of the pairs and is given by

$$k_A = \nu_0 e^{-E_d(AV)/k_B T}, \tag{3.9}$$

where ν_0 is the characteristic frequency of the lattice ($\sim 10^{13}$ s^{-1}) and $E_d(AV)$ is the dissociation energy required to break up the pair, usually defined as the binding energy (E_b) plus the lower migration barrier (E_m) of the two constituents:

$$E_d(AV) = E_b(AV) + \min\{E_m(A), E_m(V)\}. \tag{3.10}$$

The other reaction rate constant in (3.8), k_{AV}, represents the formation rate of the pairs and can be expressed in terms of the cross section for the impurity to capture a vacancy ($4\pi R_c$) and the diffusion coefficient of the vacancy (D_V). The diffusivity of V may in turn be expressed by $D_V = \nu_0 c^2 e^{-E_m(V)/k_B T}$ (see Sec.3.4), where c is the jump distance equal to 3.25 Å in ZnO, thus giving

$$k_{AV} = 4\pi R_c \nu_0 a^2 e^{-E_m(V)/k_B T}. \tag{3.11}$$

Since only the fraction of impurities A that at any given instant of time exist in a AV state are available to contribute to diffusion, it may be useful to estimate the probability for an impurity A to be in the AV state. By considering diffusion under steady state conditions ($\partial C_A/\partial t = 0$), it is possible to find an equilibrium concentration of impurity-vacancy pairs (solving (3.8)):

$$C_{AV}^{\text{eq}} = \frac{k_{AV} C_V^{\text{eq}} C_A^{\text{eq}}}{k_A}. \tag{3.12}$$

It can be shown that this in turn can be expressed by [47, 45]

$$C_{AV}^{\text{eq}} = \theta_{\text{AV}} \frac{C_{\text{A}}^{\text{eq}} C_{\text{V}}^{\text{eq}}}{N_s} e^{E_b(\text{AV})/k_B T}, \tag{3.13}$$

which is valid when $E_m(V) < E_m(A)$ (see (3.10)). Here, θ_{AV} is a factor that takes into account the number of equivalent ways to form the complex at a particular site and N_s is the number of available substitutional lattice sites ($N_s = 4.15 \times 10^{22}$ cm^{-3} for ZnO).

If we now consider the case where the concentration of vacancies associated with impurities (AV) is greater than the concentration of vacancies (V), this necessarily represents a situation where the vacancies spend most of their time next to the impurities. According to (3.13), this depends of the doping level, the binding energy of the pair and the temperature. A reasonable estimate of the doping levels at which the pairs are prevalent can be made by solving (3.13) for the situation at which the number of AV pairs is equal to the number of unassociated V ($C_{\text{AV}}/C_{\text{V}} = 1$):

$$\theta_{\text{AV}} C_{\text{A}}^{\text{eq}} = N_s e^{-E_b(\text{AV})/k_B T}. \tag{3.14}$$

A plot of $\theta_{AV} C_{\text{A}}^{\text{eq}}$ vs. $1/T$ is shown in Fig.3.2 for different binding energies of the AV pair. From this it is expected that for impurity-vacancy binding energies in the order of 1 eV will cause the migrating vacancies to spend most of their time next to impurties already at relatively low impurity concentrations and even at elevated temperatures.

In Fig.3.2, the apparent solid solubility of Al, Ga and In at elevated temperatures obtained experimentally by SIMS in this work (see Papers I-III), i.e., the equilibrium doping levels, are compared to (3.14) for different values of dopant-vacancy binding energies. Interestingly, previous experimental and theoretical results [40, 39] indicate that $E_b(AV)$ exceeds 1 eV for all these dopants. This means that the AV pair is expected to be the prevailing vacancy-related defect at these conditions. This is further supported in our work (Papers I-III), where we show that the dopant diffusion under various conditions can be explained solely by the AV diffusion mechanism in (3.6a).

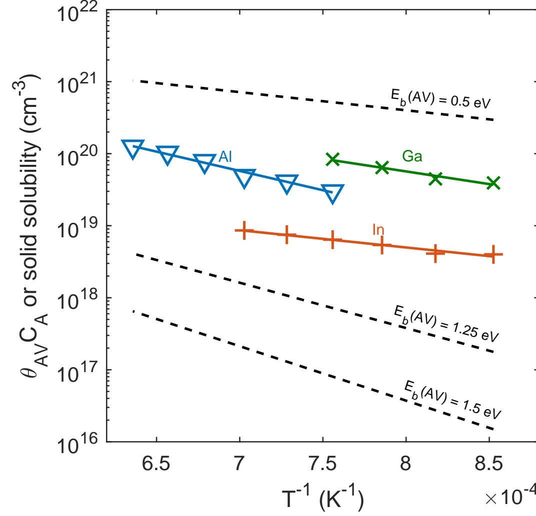

Figure 3.2: Solid solubility (solid line and symbols) for Al, Ga and In in ZnO (SIMS) in the temperature range 900-1150°C. Dashed lines, for different binding energies of the AV pair, represents lower estimates of the dopant concentration where C_{AV} equals C_{V}.

3.4 Diffusion coefficient

Impurity diffusion in crystalline materials involve the atomic exchange with intrinsic lattice imperfections, which in turn implies that a microscopic consideration is often necessary to describe the diffusion. In case of the diffusion through a vacancy mediated mechanism (3.6a), the diffusion process includes both the formation energy of the associated vacancy and the migration barrier for the exhcange process. Thus, a succesful jump requires an energy that exceeds the Gibb's free energy (G) for this process. The diffusion coefficient of an impurity A can be expressed as [48]

$$D_A = ge^{-\Delta G_A/k_BT}, \tag{3.15}$$

where g is a geometric factor. The Gibbs free energy can in turn be expressed in terms of the enthalpy (H) and entropy (S) through $\Delta G = \Delta H - T\Delta S$. This makes it possible to split the right side of Eq.(3.15) into a temperature independent term (S) and a temperature dependent term (H):

$$D_A = g\exp\left(\frac{\Delta S_f + \Delta S_m}{k_B}\right)\exp\left(-\frac{\Delta H_f - E_b + \Delta H_m}{k_BT}\right) = D_0\exp\left(-\frac{E_a}{k_BT}\right), \tag{3.16}$$

where all the temperature independent factors have been grouped together into a diffusion constant D_0. Note that D_0 is merely a structural entity [48]: $D_0^{\text{ZnO [0001]}} = (3/4)f'c^2\Gamma_0 e^{S/k_B}$, where $f' \leq 1$ is a correlation factor, $\Gamma_0 \approx 10^{13}$ s^{-1} being the typical phonon frequency and S the entropy contribution. For $S = 0$ and $f' = 1$, this results in $D_0 \approx 10^{-2}$ cm^{2}s^{-1}. In (3.16), the activation energy E_a is the overall energy required for a successful jump, including the formation of the mobile species (ΔH_f), reduced by the binding energy between the constituents (E_b), if any, plus the migration barrier for the jump (E_m). Similar subscripts (f and m) are used for the entropy S.

Equation (3.16) is best known as the 'Arrhenius relation', after the Swedish scientist Svante Arrhenius. In 1889, Arrhenius compared his own results of reaction rates of sugar cane in an acid media [49] with several previous studies of the kinetics of chemical reactions that he found in the literature and showed that in each case the temperature and rate constant could be correlated by one simple equation [50, 51]. A few decades later, in a diffusion study of thorium in tungsten in 1922 (a topic that was of high interest for improving the electron emission in electron microscopes), see Ref.[51] and references therein, it was noted that the best explanation to the diffusion of thorium in tungsten was a linear relation between ln(D) and $1/T$, cf. (3.16). This may be the first time the Arrhenius relation was used to explain impurity duffusion in a solid. From (3.16) it is clear that by modelling the temperature variation of diffusion coefficients it is possible to estimate a value for E_a, an experimental procedure that is known as isochronal (equal durations) diffusion studies. This has been an instrumental endeavour in Papers I-IV. A closely related approach that is reported in Paper I is isothermal (constant temperatures) diffusion studies, whereby the the treatment time is varied to examine any variation in the diffusion coefficient, i.e., to investigate any deviation from steady-state conditions.

Interestingly, a linear relation between E_a and ln(D_0) exists that is frequently observed for impurity diffusion experiments in solids. This relation is commonly referred to as the Meyer-Neldel (MN) rule or the compensation law, as suggested by W. Meyer and H. Neldel in 1937 in their investigation of the temperature dependence of electric conductivity in different oxides, including polycrystalline n-type ZnO rods, see e.g., Ref.[52]. This relation has been observed in different thermally activated processes, such as carrier trapping in crystalline semiconductors [53, 54, 55]. In the case of impurity diffusion in solids this correlation has been observed in a large number of materials [51]. The phenomenas of the MN rule was more recently discussed by J. Philibert [51], where he pose the question whether this apparent ubiquitous relation simply appears as a trivial fact, or if there is some deeper physical meaning hidden behind the formula. Although the physical meaning of the MN-rule, and thus the proportionality between the acti-

vation enthalpy and entropy, in the case for solid state impurity diffusion remains questionable, the rule can be used as a consistency check of impurity diffusion measurements (exemplified for ZnO in Fig.3.6 in Sec.3.7).

In semiconductors, point defects may be charged. In fact, this was implicitly considered when introducing the binding energy $E_b(AX)$ in (3.10) above. It means that the relative concentration of defects at thermal equilibrium is a function of the Fermi-level position ϵ_F. This proves especially important for the diffusion of ionized impurities (dopants) under extrinsic conditions, i.e., when $C_A \geq n_i$. Under these circumstances, the dopant itself influence the local ϵ_F, and thus the relative concentration of native defects. The formation enthalpy for a defect X with a charge q is given by [56]

$$\Delta H_f(X^q) = \Delta H_{f,0}(X^q) + q\epsilon_F, \tag{3.17}$$

where $\Delta H_{f,0}(X^q)$ is the formation enthalpy at the valence band edge (E_v). ϵ_F can in turn be approximated as

$$\epsilon_F = E_c + k_B T \ln\left(\frac{n}{N_c}\right), \tag{3.18}$$

where E_c is the position of the conduction band edge relative to E_v (i.e., the band gap), n is the charge carrier concentration and N_c is the conduction band effective density of states: [57]

$$N_c = 2\left(\frac{2\pi m_n^* k_B T}{h^2}\right)^{3/2}, \tag{3.19}$$

where $h = 4.135\,667\,43 \times 10^{-15}$ eVs [46] is the Planck constant and $m_e^* = 0.28 m_e$ [58, 59] is the electron effective mass, with $m_e = 9.109\,383\,56 \times 10^{-31}$ kg [46] being the invariant electron mass.

Equation (3.17) shows that the diffusion formation enthalpy depends on ϵ_F, and hence the diffusivity in (3.16) will be a function of ϵ_F. Therefore, the diffusion of dopants under extrinsic doping conditions will introduce a spatial variation in ϵ_F, which implies the existence of an electric field and an energy band bending arising from the non-uniform dopant distribution. In an early attempt to explain dopant diffusion under extrinsic conditions it was included an electric field factor H that enhanced or retarded the diffusion, taking values between 1 (intrinsic regime) and 2 (far-extrinsic regime) [60].

In a review paper by Seeger and Chik [61] in 1968, it was pointed out (likely for the first time) that as defects in silicon and germanium ionize, each charge state could result in a separate contribution to the overall diffusivity. This notion was further developed by the fast-growing semiconductor community in the following

years and later summarized and applied by Fair (e.g., Ref.[62]), suggesting the effective diffusion coefficient to be the sum of several diffusivities:

$$D_A^* = H\left[D^i_{A^+X^0} + D^i_{A^+X^-}\left(\frac{n}{n_i}\right) + D^i_{A^+X^{2-}}\left(\frac{n}{n_i}\right)^2\right], \tag{3.20}$$

where D^i is the diffusivity under intrinsic conditions and n is the free electron concentration. The relation (3.20) is therefore often reffered to as the Fair model, or Fair's vacancy model as it played an important part in explaining many vacancy mediated diffusion phenomenas in silicon [62]. In (3.20), only donor dopants and their diffusion through three mobile defects A^+X^0, A^+X^- and A^+X^{2-} have been considered, but it can easily be extended to apply for higher order charge states and in the case for acceptors dopants. For a derivation of (3.20), see e.g., Fahey *et al.*[45], where it is assumed that n is determined solely by the diffusing dopant concentration and that equilibrium condition is established. In (3.20) the superscript i denotes intrinsic conditions, and $n_i = \sqrt{N_C N_V}\exp\big(-\frac{E_g}{2k_BT}\big)$ is the intrinsic carrier concentration with N_C and N_V being the effective density of states at the conduction- and valence band edge, respectively.

Figure 3.3 shows the concentration-dependence of D_A^* for the different charge states in (3.20). It should be emphasised that it is the difference in charge between the dopant A and the controlling diffusing species which defines the charge state dependence of the diffusion mechanisms in (3.6). For instance, assume that the diffusion of Al in ZnO takes place at the Zn sub-lattice by the vacancy mediated mechanism in (3.6a), with the immobile Al_{Zn} being a single donor (+) and that the V_{Zn} is a double acceptor (2-). Then, if the resulting concentration vs depth profiles can be modelled by $D_{\text{Al}}^* \propto C_{\text{Al}}^2$ (cf. Fig.3.3), it is the difference in charge between Al_{Zn}^+ and the formed $(\text{Al}_{\text{Zn}}\text{V}_{\text{Zn}})^-$ pair that causes the shape of the profile. A misconception that is sometimes encountered is that the correct term is given simply by the charge of the mediating defect alone (e.g., $\text{V}_{\text{Zn}}^{2-}$).

As this framework can be quite effective to get an idea of likely vs unlikely dopant diffusion mechanisms based only on SIMS profiles, it may be beneficial to continue with another example and consider what diffusion mechanisms could possibly result in the concave (e.g., $D_A^* \propto C_A^{2-}$) profile in Fig.3.3 (green curve). Apparently, it must represent a situation where the dopant migration is effectively retarded by its own presence. For instance, consider the following dissociative diffusion mechanism (cf. (3.6c)):

$$\text{Al}_{\text{Zn}}^+ \rightleftharpoons \text{Al}_i^{3+} + \text{V}_{\text{Zn}}^{2-}. \tag{3.21}$$

Here, two very different dopant diffusion profiles could possibly be the result, depending on which of the mobile defects on the right hand side of (3.21) that

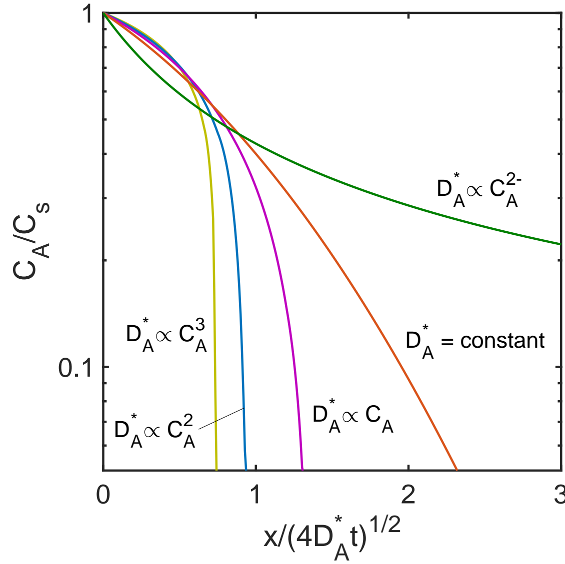

Figure 3.3: Normalized diffusion profiles for the different effective diffusion coefficients as given by equation (3.20), with $C_A = n$.

is the controlling/limiting species (i.e, the one with the lower transport capacity DC). If Al_i^{3+} was the controlling process, this would yield $D^*_{\mathrm{Al}} \propto C^{2-}_{\mathrm{Al}}$ and concave diffusion profiles. On the other hand, with $\mathrm{V}^{2-}_{\mathrm{Zn}}$ being the controlling process this would result in $D^*_{\mathrm{Al}} \propto C^3_{\mathrm{Al}}$ and very abrupt and convex diffusion profiles. For a thorough review and a systematic derivation of possible shapes of dopant-diffusion profiles, please see Refs.[63, 64].

3.5 Isoconcentration diffusion

In the above discussion we considered diffusion of dopants to take place in an initially intrinsic-like sample where the concentration of residual donor or acceptor impurities are much lower than that of the resulting dopant profiles. This situation involves a chemical gradient of the dopants, and is often the most relevant situation in device fabrication. In view of equation (3.20) above, this corresponds to n being solely determined by the dopant under study and not influenced by any background impurities. In contrast, isoconcentration diffusion represents dopant diffusion with no chemical gradient of dopants. This can be achieved by e.g., diffusing a certain isotope dopant species into a sample that is uniformly predoped to a desired concentration with a different isotope of the same element. Hence, the indiffusing dopants will not cause any change in ϵ_F, as the indiffusion is as-

sociated with an equal outdiffusion of the other isotope. This yields diffusion profiles that can often readily be described by an analytic solution to Fick's second law (3.2), for instance, an erfc(x)-profile in the case of a constant source (see (3.4)).

One of the earliest reports of isoconcentration diffusion experiments emerged in the early 1960's in a study of gallium arsenide (GaAs), where the diffusion of radioactive ^{65}Zn was studied in GaAs heavily doped with nonradioactive Zn [65]. In the following decades, many similar studies were performed for both n- and p-type dopants in silicon (Si) [45]. For instance, the diffusion of the n-type dopant arsenic (As) was studied by using ^{76}As in heavily doped ^{75}As backgrounds [66]. Common to all these studies is that they demonstrated (either implicitly or explicitly) a concentration dependence of the effective diffusivity that could be expressed in a similar form as D_A^* in (3.20).

Another more quasi-isoconcentration approach can be performed by studying the diffusion of dopant species in a region predoped with dopants having the same electronic configuration (causing similar doping), but being a different element. For instance, in a study of Ga diffusion in boron (B) doped Si it was observed an increase in the Ga diffusivity as a function of the hole concentration [67], demonstrating that isoconcentration experiments may be performed also without the need for isotopically enriched samples/conditions.

The main advantage of the isoconcentration diffusion technique is that it facilitates the interpretation of dopant diffusion. For instance, by performing a series of such experiments with different background concentration of dopants, one may attempt to construct a plot of D_A^* vs n/n_i and deduce the prevailing charge state(s) responsible for the diffusion. Moreover, comparing isoconcentration diffusion results with results from concentration-gradient diffusion experiments conducted under similar ambient conditions, provides a powerful method to reveal the fundamental defect interplay and thus determine the mechanism of diffusion.

3.6 Reaction diffusion model

The system of reaction-diffusion (RD) equations that was introduced in (3.7) and (3.8) provided a procedure for describing impurity/dopant diffusion both under initially intrinsic (concentration-gradient) and initially extrinsic (isoconcentration) conditions. In addition to being able to establish the main charge state(s) that are involved in the diffusion process, which is what Fair's model in (3.20) may provide, the RD model also allow for complete description of the diffusion

interplay (i.e, the diffusion mechanism). This is not, however, a straightforward endeavour as it requires knowledge of the concentration and diffusivity of the mediating defect, which is usually unknown. Another variable that must be know beforehand is the portion of the mediating defect that is associated with the dopant species at equilibrium conditions. As can be seen in the expression for the equilibrium concentration of AV pairs in (3.13), this requires that the binding energy E_b(AV) is known.

Modelling of impurity diffusion by a RD type approach has been performed for a variety of different materials and dopants [66, 68, 69, 65]. Usually, the issue regarding unknown distribution of vacancies is overcome by assuming that it is more or less constant [70], which is a good assumption when the vacancy is sufficiently mobile. However, for concentration-gradient diffusion experiments this is not enough to solve the full system of RD equations to obtain the diffusivity and solubility of the AV pairs, and one have often resorted to isoconcentration measurements which directly provides the solubility and diffusivity of the dopant-vacancy pair by modelling using erfc profiles.

A new approach to the RD modelling was recently suggested by Johansen *et al.*[71] which uses theoretical results obtained from DFT (see Appendix A for a short introduction to DFT) to estimate the abundance of mediating defects and their binding energy with dopants. This direct link with DFT-predictions enables numerical concentration-distribution profiles of the mediating defect to be estimated, which combined with experimental results can be used to solve the system of RD equations. In the case of dopant diffusion in ZnO involving doubly negatively charged zinc vacancies (V_{Zn}^{2-}), see (3.6a) and (3.6c), $C_{V_{Zn}^{2-}}(x,t)$ can be estimated from DFT-predictions of the V_{Zn}^{2-} formation energy ($E_f(V_{Zn}^{2-})$):

$$C_{V_{Zn}}(x,t) = N_s e^{-(E_f(V_{Zn}^{2-})/k_BT)} \left(\frac{n(x,t)}{N_c(T)}\right)^2, \tag{3.22}$$

where N_s is the number of substitutional zinc lattice sites and n accounts for the charge neutrality of the system:

$$n = jC_{A^j} + kC_{V^k} + lC_{AV^l} + mC_{B^m}, \tag{3.23}$$

with the charge states $j,k,l,m \in \{0,\pm1,\pm2,...\}$ and C_B is the effective background concentration of residual impurities. The vacancy formation energy can in turn be expressed by (cf. (3.17))

$$E_f(V_{Zn}^{2-}) = E_{f,0}(V_{Zn}^{2-}) - 2\epsilon_F, \tag{3.24}$$

where $E_{f,0}(V_{Zn}^{2-})$ is the formation energy at the valence band edge, set to 7.0 eV in our simulations as guided by previous DFT reports [21, 72, 73, 74], and with

ϵ_F given by (3.18) above. Figure 3.4 shows the formation energy of some relevant defects in ZnO, as obtained from DFT calculations and reported in Paper IV. From this it is expected that the -2 charge state is the most favourable state for the V_{Zn} at normal/n-type conditions (high Fermi-levels). Furthermore, at the simulated temperatures (in the range 900-1150°C in the present work), the band gap of ZnO (3.3 eV at 295 K) varies between 2.77–2.64 eV, assuming a similar temperature dependence for the band gap narrowing (-0.52 meV/°C) as that reported up to 500°C [75]. In the simulations, it is further considered a fixed valence band edge, that is, the absolute value for the conduction band edge equates the band gap at all temperatures.

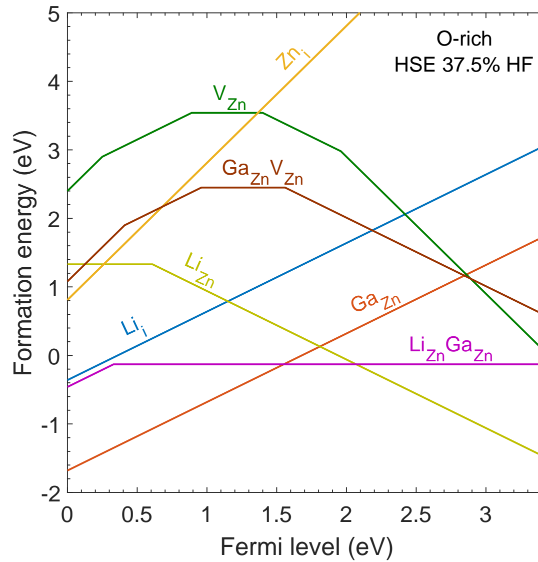

Figure 3.4: Formation energy as a function of Fermi-level position for some typical defects in ZnO, as reported in Paper IV.

With this framework at hand, that is, bridging experimental- and theoretical results, it is possible to obtain detailed information about the impurity-vacancy interplay. Fig.3.5(a) schematically illustrates the vacancy mediated diffusion mechanism for an impurity A, as introduced in (3.6a). To move A via V it requires the formation and presence of a V as a neighbour. That is, V must form at some site in the crystal and approach the more stable A. The associated V must then either (i) perform a direct exchange with A and dissociate or (ii) exchange and rotate around A. In a first approximation, the overall activation energy for the diffusion of A can be expressed as a sum of all the above processes:

$$E_a = E_{\mathrm{f}}(V) + E_m(V) + E_m(AV) - E_d(AV), \tag{3.25}$$

where $E_{\mathrm{f}}(V)$ is the formation energy of V, $E_m(V)$ and $E_m(AV)$ are the migration barrier for V and the barrier for the migration of AV, respectively, while $E_d(AV)$ is the energy necessary to dissociate the pair. The dissociation barrier can in turn be approximated as

$$E_d(AV) = E_b(AV) + E_m(V) - k_B T, \tag{3.26}$$

where $E_b(AV)$ is the binding energy of the pair and the term $k_B T$ arises due to the slightly reduced (by the amount of $k_B T \sim 0.1$ eV) potential energy of the dissociated V at a distance R_c (effective capture radius) from A. Inserting (3.26) into (3.25) gives

$$E_a = E_{\mathrm{f}}(V) - E_b(AV) + E_m(AV) + k_B T, \tag{3.27}$$

where the two first terms on the right hand site are estimated from theoretical predictions and $E_m(AV)$ is directly extracted from the RD-modelling (fitting parameter) of the experimental concentration vs depth profiles (SIMS). In Paper I we demonstrate that the sum of all the terms on the right hand side obtained using the RD model is in good agreement with that obtained when analysing the experimental data using the more common Fair's model (3.20).

A similar treatment for the dissociative mechanism in (3.6c) yields a reduced process, as illustrated in Fig.3.5(b). For a dissociative mechanism, the overall activation energy for diffusion is equal to the dissociation energy barrier, i.e., the difference in energy between substitutional and interstitial sites (removal energy E_r), and then either the remaining vacancy or the displaced atom must overcome their respective migration barriers (the lower one will be decisive at comparable concentrations). Paper IV adress the diffusion of Li in ZnO through this type of dissociative diffusion mechanism.

3.7 Impurity diffusion in ZnO: A brief review

ZnO is one of the earlier crystalline systems to be systematically studied by impurity diffusion, with one of the first reported experiments performed by the pioneers D. G. Thomas and J. J. Lander at Bell Labs in the late 1950s for the elements hydrogen (H), indium (In) and lithium (Li) [76, 77, 78]. To monitor the diffusion, they measured the increase in the electrical conductivity after doping of vapor phase ZnO crystals. For H, an activation energy of 0.91 eV was obtained, with a reasonable diffusion constant of 3×10^{-2} cm^{2}s^{-1}, demonstrating a fast diffusion process. It can be noted that this was only about a decade after the discovery and new notion of point defect mediated diffusion, established by Kirkendall [41].

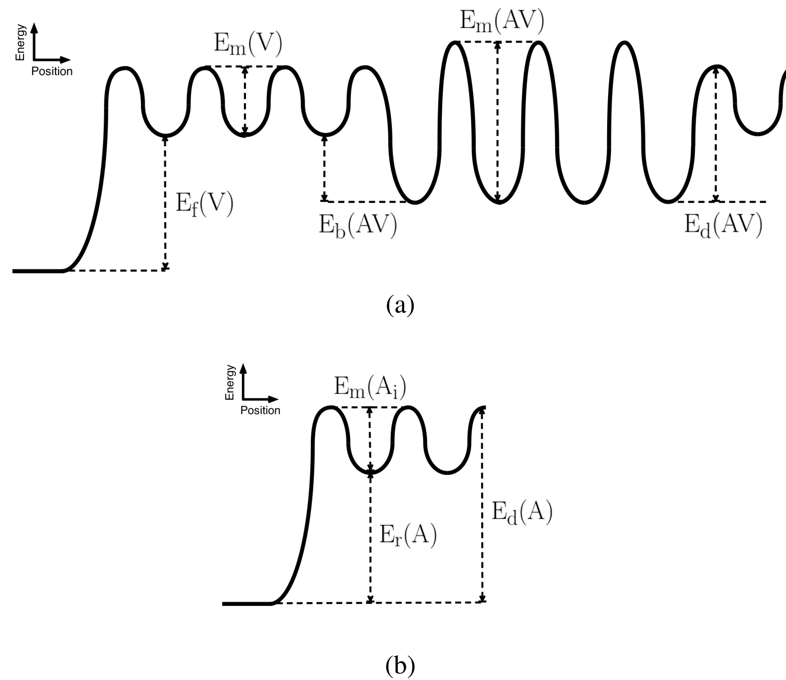

Figure 3.5: Energy diagram illustrating the involved processes for (a) the vacancy mediated diffusion mechanism and (b) the dissociative diffusion mechanism.

More recently, the diffusion of the chemically equivalent deuterium (^{2}H) was studied by Ip *et al.*[79] and Nickel [80], where ^{2}H plasma-exposed ZnO samples (vapor phase and melt-growth) were analyzed by SIMS. In both reports, the diffusion of ^{2}H was found to hold an activation energy as low as ~ 0.2 eV. However, the corresponding pre-exponential factor was on the order of $\times 10^{-8}$ cm^{2}s^{-1}, which raise the question whether the results do reflect the actual migration barrier for hydrogen diffusion or perhaps a more complex process. However, Nickel [80] also studied the out-diffusion of H_2, which indicated that the migration barrier is above 0.8 eV, in accordance with the initial study by Thomas and Lander [76]. Following the deuterium-SIMS approach, Johansen *et al.*[81] studied ^{2}H implanted HT grown ZnO and reported a diffusion activation energy of 0.85 eV and a prefactor of 2.5×10^{-2} cm^{2}s^{-1}, which is closer to that reported by Thomas and Lander. Johansen *et al.* also demonstrated that the migration of ^{2}H could be explained by a trap-limited diffusion model with Li as the responsible trap, forming ^{2}H-Li pairs.

H is undoubtedly a fast diffusing species (interstitial) in ZnO, with significant diffusion taking place already at 300°C [81]. The accumulated results, and especially the insights provided by Johansen *et al.*[81] regarding the H-Li interplay,

indicates that the large discrepancy of E_a and D_0 reported in the literature may be due to the different content of residual Li in the different samples used. All the reported activation energies and pre-exponential factors are summarized in Table 3.1, and in Fig.3.6 the values can be seen to fall on a trend line in a Meyer-Neldel plot.

Similar to H, Li is another element that is usually (unintentionally) incorporated into the crystal during growth. However, Li is mainly found in significant concentrations in the HT method ($\sim 1-5\times10^{17}$ cm^{-3}), while H is invariably present ($< 5\times10^{17}$ cm^{-3}) [12]. An early study by Lander [78] reported $E_a = 0.98$ and $D_0 = 2\times10^{-2}$ cm^{2}s^{-1} for the diffusion of Li in the presence of Zn-vapor. The diffusion coefficients were obtained by following the change in conductivity of the indiffused crystal as a function of time. The diffusion was performed under Zn-rich conditions, ensuring Li to be in the interstitial donor configuration (Li_i^+), thus facilitating the interpretation of the extracted activation energy, i.e., the migration barrier of Li interstitials. Moreover, Lander demonstrated that similar experiments performed in air restricted the diffusion of Li and resulted in a sharp boundary between an indiffused compensated region and the inner unaffected/intrinsic region.

More recently, Sakaguchi *et al.*[82, 83] studied Li diffusion in oxygen implanted undoped and Al-doped (3.2×10^{19} cm^{-3}) ZnO. They found that the diffusion of Li was slower in Al-doped ZnO, and reported diffusion activation energies of 2.5 eV (undoped) and 3.2 eV (Al-doped) that was explained by Li diffusion via V_{Zn}. This was, however, not further discussed, but based on these results it would be logical to assume that Al-related defects and/or V_{Zn} may act as a trap for mobile Li interstitials (i.e., V_{Zn} is expected to increase by the Al-doping). This becomes even more evident when taking into account the recent Li diffusion experiments performed by Knutsen *et al.*[84] under oxygen rich conditions. In line with Lander, Knutsen clearly demonstrated electrically compensated indiffused Li-regions, but could also reveal (due to the detailed SIMS-characterization) a highly abrupt diffusion front separating the unaffected inner bulk. Interestingly, it was found that the characteristic level where the concentration of Li changes abruptly correlated with the concentration of donors in the material, indicating that Li diffuse fast in the compensated region (in the form of Li_i^+) and that the diffusion front acts as a sink for these Li_i that converts into more stable Li_{Zn}^-. The diffusion of Li was described by assuming Li_i^+ to be the mobile species and Li_{Zn}^+ immobile at the studied temperatures (≤ 600°C). This resulted in an activation energy of 1.34 eV for the diffusion of Li, slightly higher than that obtained by Lander, which may be assigned to the opposite ambient experimental conditions used.

Sodium (Na) is another group I element that has been observed to behave quite

Impurity	D_0 (cm^2/s)	E_a (eV)	Method	Reference
H / ^{2}H	3×10^{-2}	0.91	Conductivity	Thomas *et al.*[76]
	2.5×10^{-8}	0.17	SIMS	Ip *et al.*[79]
	3×10^{-8}	0.23	SIMS	Nickel [80]
	2.5×10^{-2}	0.85	SIMS	Johansen *et al.* [81]
Li	2×10^{-2}	0.98	Conductivity	Lander [78]
	4.7×10^{-2}	2.5	SIMS	Sakaguchi *et al.* [82]
	4.6	3.2	SIMS	Sakaguchi *et al.* [83]
	1.5×10^{-2}	1.34	SIMS	Knutsen *et al.* [84]
Mn	3.2×10^{-3}	2.87	AAS	Kleinlein *et al.* [88]
Co	10	3.98	AAS	Kleinlein *et al.* [88]
Ni	6×10^{4}	4.4	SIMS	Sky [89]
Cu	2×10^{7}	4.8	AAS	Müller *et al.* [90]
	15	2.7	SIMS	Enoksen [91]
Al	5.3×10^{-2}	2.74	Photometry	Norman [92]
	0.3	3.3	SIMS	Paper II
Ga	3.6×10^{4}	3.75	Photometry	Norman [92]
	2.7×10^{-6}	1.47	SIMS	Nakagawa *et al.*[93]
	8×10^{-2}	3.0	SIMS	Paper I
Ag	5	2.6	SIMS	Azarov *et al.* [94]
In	2.5×10^{2}	3.16	Conductivity	Thomas [77]
	1.1	2.68	SIMS	Sakaguchi *et al.* [95]
	2.9×10^{-7}	1.17	SIMS	Nakagawa *et al.* [96]
	4×10^{-2}	2.2	SIMS	Paper III

Table 3.1: Experimentally obtained diffusion constants and activation energies for impurities in ZnO. AAS: 'atom absorption spectroscopy'.

similar to that of Li, competing for the same trapping sites (Zn-site) in the n-type ZnO lattice [85]. A diffusion activation energy of ~ 1.7 eV has been reported for Na (no prefactor could be obtained) [86]. Furthermore, the next element in the same group in the periodic table, potassium (K), has been observed to be more or less immobile for heat treatments up to $900°$C in K-implanted ZnO [87], indicating a substantially higher diffusion activation energy as compared to that of Li and Na (diffusing already at $450°$C).

Studies of transition metal impurities in ZnO has mainly been motivated by theoretical predictions of transition-metal-doped ZnO being a promising system in order to obtain a dilute magnetic semiconductor that may work at room temperature [97, 5]. The diffusion of Manganese (Mn) and Cobalt (Co) have been studied

by Kleinlein *et al.*[88] using atom absorption spectroscopy (AAS), and reported diffusion activation energies of 2.87 eV and 3.98 eV, respectively.

The diffusion of nickel (Ni) has previously been shown to be strongly affected by the ambient condition [89], with a reported diffusion activation energy of 4.3 eV, where both a vacancy mediated and an interstitial mechanism was suggested [89]. Further, copper (Cu) and silver (Ag) are other transition metals that has received attention for their potential for p-type doping. For Cu, a diffusion activation energy of 4.8 eV with a prefactor of 2×10^7 cm^{2}s^{-1} have been found in an early report [90]. Here it was also observed by conductivity measurements that an increase in the Cu concentration resulted in a concurrent decrease in the electrical conductivity. For Ag implanted ZnO, the diffusion of Ag has been shown to exhibit a trap-limited diffusion process (i.e., a diccosiative diffusion mechanism) where the traps was suggsted to be Li_{Zn} and V_{Zn}, yielding a diffusion activation energy of 2.6 eV with a pre-exponential factor of 5 cm^{2}s^{-1} [94].

The diffusion of the donor dopants aluminum (Al) and gallium (Ga) was first reported by V. J. Norman [92], where the total amounts of Al/Ga were analysed using dichromate photometry (the material was dissolved and excess electrons effectively counted). A diffusion activation energy of 2.74 eV and 3.75 eV for Al and Ga were obtained, respectively.

Recently, Nakagawa *et al.*[93] used SIMS to measure Ga-implanted ZnO single crystals, revealing a concentration-dependent diffusion of Ga. An activation energy of 1.47 eV with a rather low prefactor of 2.7×10^{-6}cm^{2}s^{-1} was reported. Two models were proposed for explaining the diffusion of Ga: a kick out mechanism (3.6b) and a vacancy mechanism (3.6a). It must be noted that the diffusion coefficients reported in [93] have been obtained by using the Fair method using only the quadratic term (3.20), however, their simulated curves do not comply with such dependence. Moreover, and more importantly, the reported values used for the intrinsic carrier concentrations are not those of ZnO, but actually corresponds to the values for Si. This makes the results by Nakagawa dubious.

Continuing with group III elements, the diffusion of indium (In) was first reported by Thomas [77] about two years after his contributions on H diffusion in ZnO. He report a diffusion activation energy of 3.16 eV employing conductivity measurements, and also used Hall effect measurements (room temperature) to reveal apparent solid solubilities ranging from $10^{17} - 2 \times 10^{19}$ cm^{-3} after indiffusion heat treatments of $800 - 1300$°C.

More recently, Sakaguchi *et al.*[95] reported on a diffusion activation energy of 2.68 eV for In implanted ZnO characterized by SIMS. The shape of the diffusion profiles were very similar to that observed for Ga in [93], but the diffusion

coefficients were extracted using a simplified method by assuming free-diffusion and relating the diffusion constant only to the final profile depth (i.e., excluding the solid solubility). A few years later, also Nakagawa *et al.*[96] report on a very similar study, but obtained a considerably lower activation energy of 1.17 eV. However, it must be noted that a closer look at the experimental data reported in the two studies, reveal that the experimental data are identical (SIMS profiles can be seen to show identical noise). The two studies share co-authors, and it is therefore surprising that the results are presented as individual and unconnected events with significantly different results. It is of our opinion that the former study (using the simple modelling) is most reliable, as the modelling performed by Nakagawa *et al.* use unrealistic values for n_i (Si), as discussed above for Ga. Besides, the questionable diffusion prefactor of 2.9×10^{-7}cm^{2}s^{-1} obtained by Nakagawa *et al.* substantiate this notion.

Figure 3.6 shows a plot of ln(D_0) vs E_a that have been collected from available data in the literature, together with our results reported Papers I-III (see Tab.3.1). The experimental data can be seen follow a Meyer-Neldel trend line, i.e., a linear relation between the activation entropy S ($\propto$ ln(D_0)) and the activation energy E_a (see Sec.3.4 and (3.16)). It should be noted that for many of the impurities the values scatter substantially between the different reports, e.g., the reported activation energy for In varies from 1.17 eV to 3.16 eV. However, the plot demonstrate that the activation entropy is reduced accordingly, which indicate that different experimental conditions may be responsible for at least some of the inconsistency in E_a (e.g., E_a may depend on the Fermi-level position). However, values for D_0 that is far from the theoretical value of $\sim 10^{-2}$ cm^{2}s^{-1} (for $S = 0$), especially on the low side since S cannot be negative, may rather indicate inaccuracy in the experiment and/or modelling.

It is worth noting that all the elements presented in Tab.3.1 and Fig.3.6 have been assigned to diffuse either as interstitials or mediated by zinc vacancies. Reports of impurity diffusion taking place at the oxygen sub-lattice are scarce, and to our knowledge absent if you look for diffusion coefficients. It is not surprising that the above elements prefer Zn or interstitial sites, they are after all impurities with small or similar ionic radius as the Zn cation. It is more so that those impurities that do tend to occupy O-site have proven to be stable within a reasonable temperature range (≤ 1300°C).

It is not the intention for this thesis to give a complete overview of the work done by the many reports on O-substituting impurities, but it can be noted that few/none of the reports presents experimental diffusion activation energies. A few words on the topic may still be appropriate; A straightforward explanation for the challenge in observing O sub-lattice diffusion may be discussed in terms of

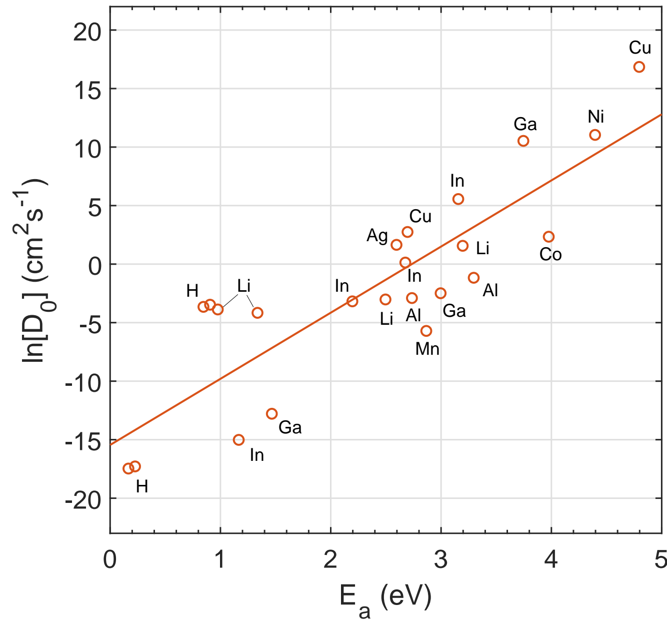

Figure 3.6: Logarithm of the diffusion constant vs diffusion activation energy for different impurities in ZnO, demonstrating a Meyer-Neldel relation.

the availability of O vacancies (V_O), which under normal conditions (n-type ZnO in air) are much lower than that of V_{Zn} [21]. A high formation energy of V_O are not the only component that would suppress V_O-mediated impurity diffusion, but also the migration barrier for V_O diffusion is determed by the effective availability of V_O. Both previous experimental and theoretical studies suggests that these values are high, especially the formation component [39, 40, 21], and that O self-diffusion takes place by means of an interstitial mechanism [98, 99, 100]. Hence, the diffusion of impurities substituting O-site seems to have to dissociate into their interstitial configuration in order to migrate (see (3.6b) and (3.6c)), thus explaining the stability and lack of reports on their diffusion activation energies. Moreover, interstitials are often more challenging to experimentally observe (fast diffusing species) and thereby more difficult to study, especially if the diffusion initiation process (dissociation) requires high temperature conditions.

Chapter 4

Characterization techniques

This work has mainly relied on two experimental techniques. Sec.4.1 will introduce secondary ion mass spectrometry (SIMS) which has been used to measure atomic concentrations vs depth distributions, a method that enables the observation of impurity diffusion with high precision. Sec.4.2 gives an introduction to positron annihilation spectroscopy (PAS), a method that has been used to directly observe open volume defects, that is, defects that often mediate the diffusion of impurities. Therefore, combining these techniques may provied valuable information about the detailed interplay between impurities and inherent open volume defects.

4.1 Secondary Ion Mass Spectrometry

SIMS is a technique that can be used to directly observe elements in a solid material, providing up to parts per billion sensitivity. Combined with a high depth resolution (in the range of 10 nm or better) and a dynamic range of 5 orders of magnitude, this technique has shown to be very valuable for many applications. SIMS has played an instrumental role in the fundamental understanding of crystalline materials, as it is an excellent tool for obtaining accurate concentration vs depth distributions of all elements and their isotopes.

4.1.1 Rationale

The first mass spectrometer was developed in 1913 by J. J. Thomson [101, 102], where the ions were separated by passing through a magnetic field. Different

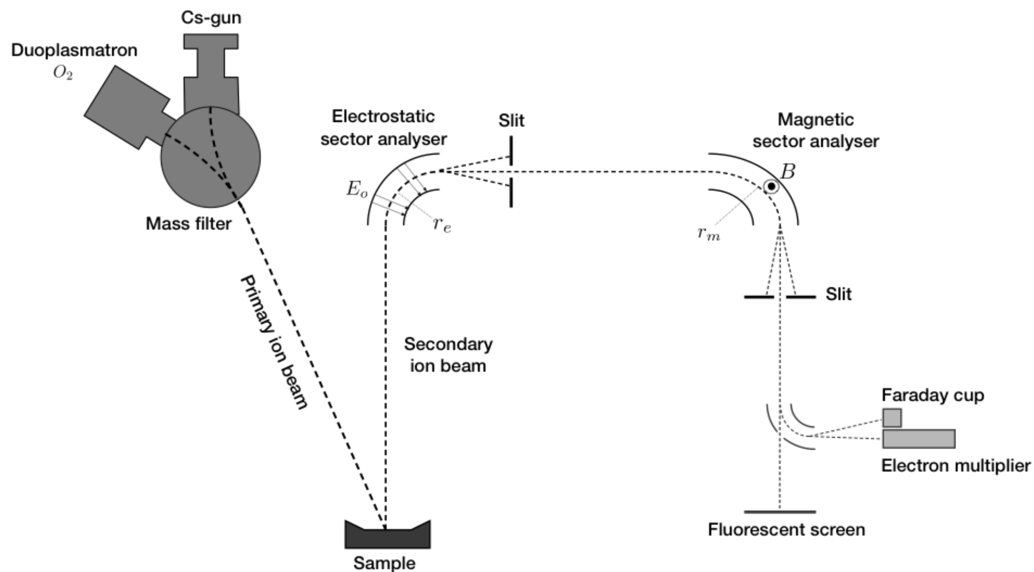

Figure 4.1: Simplified schematics of the Cameca IMS-7f SIMS.

methods evolved in the following decades, and the earliest report of SIMS was reported in 1931 [103]. Here it was demonstrated that ionized atoms from a solid material could be produced by bombarding the material by other ions, a process that is now known as sputtering. Mainly three different SIMS instrumentations were developed in the years to come, time-of-flight, quadropole and magnetic sector.

In this work, a magnetic sector SIMS (Cameca IMS-7f) has been used. A sketch of this instrument is shown in Figure 4.1. A focused ion beam (primary) is used to sputter a solid surface while collecting and analyzing the ejected ions by forming a secondary ion beam. The secondary ions are then separated in a mass spectrometer before the ion intensity is measured as a function of time or position of the primary ion beam on the target. This makes it is possible to record a mass spectrum, lateral impurity distributions with typically a few μm resolution and impurity depth profiles with nm resolution. Moreover, by the use of standard samples, absolute concentrations with less than $\pm 10\%$ error in accuracy can be obtained [102].

In the magnetic sector SIMS used in the present work, the primary ions are generated by either a duoplasmatron (O_2) or a Cs-gun and focused onto the sample (Fig.4.1). The primary ion beam is rastered over an area up to $500 \times 500 \mu m^2$, forming a crater in the sample as a function of time. Ionized species ejected

from the sample surface can then be accelerated towards the analysers and detectors, forming a secondary ion beam. The base pressure in the sample chamber is $\sim 10^{-9}$ mbar, allowing a sufficient long mean free path for the ions, and more importantly ensuring a reduced deposition rate of ambient species onto the sample surface. The secondary ions (e.g., single ions or larger ionized molecules) are mass separated by passing through an electrostatic sector analyser (energy filtering) before they proceed towards a magnetic sector analyser (mass filtering). Finally, the secondary ions are detected either by an electron multiplier, a Faraday cup, or by a fluorescent screen. In this work, a 10 keV O_2^+ ion beam have mainly been used, i.e., the potential difference between the source and sample. Furthermore, in the case for highly resistive samples, the primary ion beam may result in a build-up of positive charge, and the excess charge must be removed or compensated for proper analysis. In the Cameca IMS-7f, this may be resolved by a built-in normalized electron gun that is projected onto the sample for charge compensation.

4.1.2 Sputtering

When an energetic ion impinges onto a solid surface, it sets the directly impacted target atoms in motion. This, in turn, set other target atoms in motion and a collision cascade will evolve. For the typical energies applied in SIMS ($5 - 15$ keV), this causes some of the target atoms/species in the near surface region to obtain enough momentum in the outward direction to surmount the surface barrier height and leave the material [104], a process that is known as sputtering. The average number of ejected target atoms per primary impinging ion (Y) will depend on the energy and mass of the primary ions, the target atoms mass and surface barrier hight for escape, as well as the primary beam angle of incidence. The sputtering yield Y is typically in the range of 1-10 atoms/ion [102].

The collision cascade model, as originally reported in 1969 by Sigmund [105], led to a quite good understanding of the sputtering process. To analyze the sputtered species, however, they must be ionized, and this process is still not completely understood [102]. It has been established that the presence of reactive species such as Cs and O at the target surface will enhance the secondary ion yields for negative and positive ions, respectively. This means that the secondary ion yield can vary with the sample matrix itself (matrix effect), and is the main reason SIMS quantification must rely on standardized samples. Furthermore, the secondary ion yield also depends on the primary beam energy and the angle of incidence. In fact, the secondary ion yield and the sputtering yield has the opposite dependence on the angle of incidence, and to balance this, analysis is normally conducted with

an angle of incidence in the range $0° - 60°$ [102]. Typical secondary ion yield is on the order of $\gamma \sim 1\%$ (ionization probability) of Y, but may vary substantially [106, 102].

4.1.3 Analysis

Close to the sample surface there is an extraction electrode that accelerates the secondary ions formed near the surface of the sample towards the spectrometer. This secondary beam first passes through a set of apertures such that only secondary ions from the center of the crater ($\sim 30\%$ of the crater base) are detected. The secondary ions will then enter an electrostatic energy analyser (ESA), composed of two curved metallic plates at different potentials (see Fig. 4.1). The ions will experience a centripetal force

$$F = qE_0, \tag{4.1}$$

where E_0 is the electric field. The centripetal force exerted on an ion with mass m moving at tangential speed v_e through the ESA, along a path with curvature radius r_e can be expressed by

$$F = \frac{mv_e^2}{r_e}, \tag{4.2}$$

Combining (4.1) and (4.2) gives

$$qE_0 = \frac{mv_e^2}{r_e}, \tag{4.3}$$

which means that only ions with a kinetic energy matching r_e will be curved to pass through the ESA-exit slit and proceed for furtehr analysis. Upon entering the magnetic sector analyser (MSA), the ions will experience a Lorentz force from a magnetic field B that is perpendicular to the their path:

$$F = qv_mB, \tag{4.4}$$

where v_m is the tangential speed of ions through the MSA, and F is perpendicular to both the trajectory and the magnetic field. It then follows that

$$qB = \frac{mv_m}{r_m}. \tag{4.5}$$

It is reasonable to assume that no energy is lost when the ion travels between the ESA and MSA, such that $v_e = v_m$, and combining (4.3) and (4.5) results in

$$\frac{m}{q} = \frac{(r_mB)^2}{r_eE_0}. \tag{4.6}$$

This means that only ions satisfying (4.6) will travel all the way from the sample surface to the detector.

The purpose of the ESA is to narrow the range of ion energies that will enter the MSA, thus enabling high mass resolution, which may be further increased by reducing the MSA exit slit. Moreover, the energy distribution of the sputtered particles is typically higher for single ions, as compared to heavier/larger molecules. By aligning the ESA exit slit such that only the higher energy ions are accepted, this will suppress the undesired ionized molecules, that otherwise might have easily be mistaken for a faster-moving single ion (interference), i.e., it is the mass-to-charge ratio that is detected.

4.1.4 Quantification

The SIMS technique is not self-quantitative and requires the use of a reference sample. As discussed above, this is due to the unpredictable secondary ion yield (ionization process) that varies between matrices. The most reliable type of quantification is obtained by an ion implanted reference sample. That is, the element of interest is implanted into a similar matrix as that of the sample under study. Since the dose of the implanted ions can be obtained from the ion impanter, this allows for accurate determination of absolute concentrations, with less than $\pm 10\%$ error [102].

The intensity of ions I_A, for an element A, that reach the electron multiplier will depend on several parameters: the primary ion beam intensity I_p, an instrument transmission function T (e.g., the type of apertures used and the width of the slits), the sputtering yield Y and the ionization probability γ_A, and of course the concentration of the element (C_A). We may then express the measured intensity I_A as

$$I_A = I_p Y \gamma_A T C_A. \tag{4.7}$$

Since both C_A and γ_A are unknown, the atomic concentration can not be quantified directly from (4.7), and we must rely on a reference sample. By measuring the reference sample using similar conditions as for the sample under study, this directly provides a good measure of the four first proportionality factors on the right hand side of (4.7). These are usually grouped together into a sensitivity factor $SF = I_p Y \gamma T$, and enables the conversion from intensity (counts per second) to concentration (cm^{-3}). In addition, due to the delicate design of magnetic sector instruments (a distance of only 4.5 mm between sample holder and extraction electrode), a slight variation in the extraction of the ionized species may occur due to small variation in hights over a sample holder. This can be accounted for by

normalizing the impurity signal to the signal of a matrix species, and SF is then renamed to relative sensitivity factor (RSF).

During a SIMS depth profiling, the primary ion beam is contineously sputtering the sample surface, while the magnetic field is cycled through one or more values in accordance with the mass-to-charge ratio of interest. This yields one or more impurity profiles as a function of time. To convert time to depth, the depth of the crater has in this work been measured by a Dektak 8 stylus profilometer, after the SIMS measurement. This depth calibration is valid if the erosion rate is constant throughout the profile, which is reasonable to assume for a homogenuous material.

4.2 Positron Annihilation Spectroscopy

Positron Annihilation Spectroscopy (PAS) is a unique technique that can be used to directly observe open volume defects in any type of crystalline material. For semiconductors, open volume defects, especially in the form of single open lattice sites (vacancies), strongly affects the electrical properties of the material. In addition and as discussed in Sec.3.3, vacancies plays a predominant role in the diffusion of many impurities and dopants. The information that can be obtained from a PAS measurement is highly complementary to that gained by a SIMS measurement, i.e., the absence of an atom vs its presence, and thus the two techniques are well suited for diffusion studies.

4.2.1 Rationale

The first experimental observation of positrons was reported in 1932 [107], following the predictions of this electron antiparticle a few years earlier by Dirac [108]. In the late 1960s it became clear that positrons were sensitive to defects in metals, and since the early 1980s PAS has been widely used for defect investigations in semiconductors [109]. The radioactive β isotope ^{22}Na is normally used as the source of positrons in a PAS experiment. A positron and a neutrino is created through the decay of ^{22}Na, leaving behind an excited ^{22}Ne that in turn decay and emit a high-energy 1.27 MeV photon, which may conveniently be used as a start signal for the process. The created positrons have a wide energy spectrum with typical energies in the hundreds of keV range, and can be immediately used to probe deep into the bulk of a solid (hundreds of microns). Positrons impinging onto a solid surface results in the following implanted Makhovian distribution

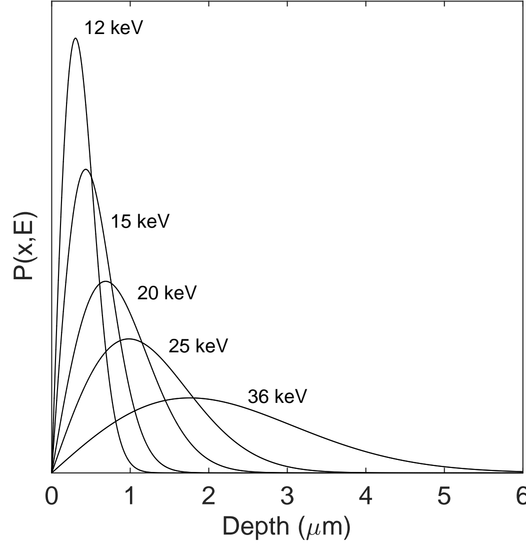

Figure 4.2: Calculated positron implantation profiles in ZnO for typical implantation energies in a Doppler broadening experiment.

[110, 111, 112],

$$P(x,E) = \frac{mx^{(m-1)}}{x_0^m} e^{-(x/x_0)^m}, \quad \text{with } x_0 = \frac{AE^r}{\rho\Gamma(1+\frac{1}{m})}. \tag{4.8}$$

Here, E is the positron energy given in keV, x and x_0 are depths in nm and $\rho = 5.606$ g/cm^3 is the density of ZnO. The empirical parameters m, A and r are material dependent and can be estimated by Monte Carlo simulations [110, 111]. They are usually set to $m = 2$, $A = 40$ μg/cm^2 keV^{-r} and $r = 1.6$, as they do not vary much between materials. Examples of Makhov profiles (4.8) in ZnO for moderate implantation energies are shown in Fig.4.2.

An energetic positron that suddenly finds itself in a crystal lattice will rapidly thermalize and survive until it meets and annihilate with an electron ($\sim$ a few hundreds picoseconds) which, importantly, emits two oppositely directed photons with an energy of about 511 keV. Hence, both a start and an end signal for the process are available to be detected by e.g., a scintillator or a semiconductor detector. Crucially though, if the positron is trapped by a vacancy (which is rather likely due to the absence of a positive/repulsive ion core), the lifetime of the positron increases (on the order of 20-80 picoseconds [113, 37]) as compared to annihilation in a 'perfect' lattice. This is because the positron lifetime is inversely proportional to the electron density, which is lower in the volume of a vacancy.

4.2.2 Doppler broadening spectroscopy

The discussion so far concerns a bulk measurement that is known as positron lifetime spectroscopy and is a technique that provides valuable information of both the size and concentration ($10^{15} - 10^{19}$ cm^{-3}) of vacancy related defects. Another method that is also frequently used, but for studying regions closer to the material surface, is slow-beam Doppler broadening spectroscopy. Here, the initial high-energetic positrons are slowed down and monochromated before they are electrostatically tuned to an energy in the range $0.1 - 50$ keV. In this way, the mean implantation depth can be varied from a few nanometers up to several micrometers, as described by (4.8). However, the moderation process (positron slow-down) limits the use of the lifetime aspect for this method, and one instead make use of the difference in the momentum distribution between valence electrons and core electrons. Since core electrons have a higher momentum than valence electrons, this will cause a broadening (Doppler shift) of the 511 keV annihilation line when positrons annihilate with core electrons. Now, in an open volume defect, the density of core electrons is comparatively low and annihilation with valence electrons is more likely, resulting in a sharper energy distribution for the annihilation line and thus the possibility to measure vacancy related defects also by the slow-beam technique.

In practice, the energy distribution is parametrized by a low-momentum shape parameter S and high-momentum parameter W, defined as the fraction of counts (with respect to the total number of counts in the line) in the central and wing region of the line, respectively, as illustrated in Fig.4.3. Because of the low momentum of the valence electrons, the S parameter is often referred to as the valence annihilation parameter. Conversely, the high momentum of the core electrons justifies W to sometimes be termed the core annihilation parameter. It should be noted that the resolution of a typical high purity germanium (HPGe) detector is around $1 - 1.5$ keV at 511 keV, which is considerable compared to the width of the annihilation line in Fig.4.3, and will therefore influence the line shape. In this work, a HPGe detector with a full width at half maximum (FWHM) of energy resolution 1.2 keV at 511 keV.

The absolute values of the S- and W parameters are meaningless as they depend strongly on the setup, and should therefore be normalized to a reference sample where no positron annihilation at vacancies is detected. There are various ways to present Doppler broadening spectroscopy results, either by plotting the S- or W parameter as a function of positron implantation energy/depth or by representing W as a function of S. A presentation by the former will show the distribution of the open volume defects as a function of depth. An increase in the S signal may be

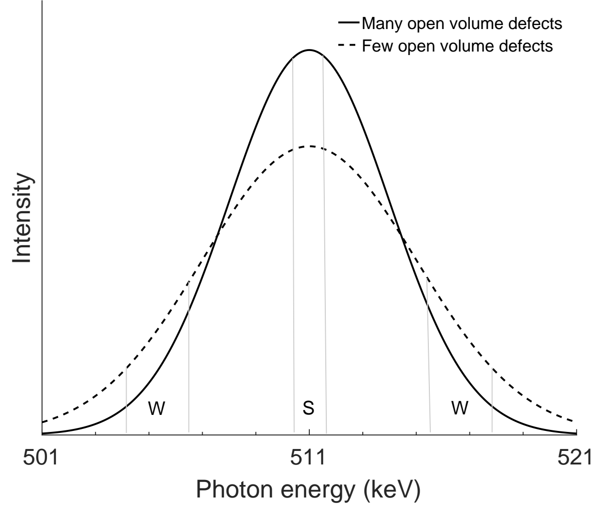

Figure 4.3: Sketch of the annihilation energy distribution, illustrating the annihilation line change between a defect lean material and open volume defect saturated material.

viewed as an increase in the concentration of vacancy related defects. However, a similar behaviour would also be observed if simply the size of the open volume of the defects increased, and one can therefore not conclude from the $S(E)$ plot alone. For this, also the W parameter need to be taken into account. In paper II we showed that by constructing a $W(S)$ plot for several ZnO samples with different n-type doping levels, all the values fall on the same line connecting the vacancy lean (lattice) and vacancy saturated cases, evidencing the V_{Zn} as the predominant open volume defect in those samples. It was then possible to estimate an absolute V_{Zn} concentration given by [114]

$$C_{V_{Zn}} = \frac{\rho}{\mu}\nu_L \frac{S - S_L}{S_V - S}, \quad (4.9)$$

where $\rho = 8.3 \times 10^{22}$ cm^{-3} is the atomic density of ZnO, $\mu = 3 \times 10^{15}$ s^{-1} is the positron trapping coefficient for negatively charged vacancies at room temperature, and $\nu_L = 5.9 \times 10^9$ s^{-1} is the annihilation rate in the ZnO lattice. $S_L = 1$ and $S_V = 1.050$ are used as the parameters for the ZnO lattice annihilation and the V_{Zn} annihilation, respectively [114, 37, 38, 115].

Chapter 5

Results

The results obtained in this work are presented in Papers I-V appended to the thesis. This chapter will start with a brief summary and discussion of each paper (Sec.5.1). This is followed by a few preliminary results in Sec.5.2, before suggestions for further work on this subject are given in Sec.5.3.

5.1 Summary of appended papers

Paper I This project started out by approaching an understanding of Ga diffusion in ZnO (Paper I). Although a few reports already existed in the literature, the reported diffusion activation energies varied considerably, with values for the pre-exponential factor extending over 10 orders of magnitude. There was clearly room for a better understanding of Ga-doped ZnO, especially considering the challenges associated with the instability of ZnO-based TCO's. The smaller, but similar, element Al had recently been explained in detail through a reaction diffusion model by Johansen *et al.*, and the stage was set to apply the method also to other alike dopants.

In Paper I we used SIMS to obtain Ga concentration vs depth profiles, both as a function of temperature (isothermal) and as a function of time (isothermal). The shape of the diffusion profiles was found to be similar to that observed for Al, revealing box-like indiffused regions, but comparably deeper. The diffusion could be easily described by the Fair model (3.20) using only the second-order term, demonstrating a quadratic relation between the Ga-doping and the Ga diffusivity. Given the prevailing notion that Ga is a single donor (Ga_{Zn}^{+}) and that V_{Zn} is a double negatively charged acceptor (V_{Zn}^{2-}) in n-ZnO, it may as a first approximation

seem reasonable to immediately conclude upon a vacancy mediated mechanism through the formation of $(Ga_{Zn}V_{Zn})^-$ pairs. However, there are in principle other mechanisms for Ga diffusion that would result in similar quadratic dependence between C_{Ga} and D_{Ga} (c.f., Sec.3.4). This issue may be resolved by performing the diffusion experiments under different isoconcentration conditions (which we report in Paper II). In Paper I, however, a different and novel approach was carried out; Here we applied the RD-model developed by Johansen *et al.*, which inherently implements theoretical results based on DFT calculations. The results in Paper I demonstrates that recent DFT-predictions are consistent with our experimental results for Ga-diffusion. The validity of the RD-model was confirmed by comparing with the Fair model, and yielded an activation energy of 3.0 eV for the diffusion of Ga. Importantly, the inherent microscopic character of the RD-model enabled the determination of the migration barrier of the $(Ga_{Zn}V_{Zn})^-$ pair, which was found to be 2.3 eV, in excellent agreement with DFT results [73].

Paper II It has been suggested that doping by group III elements (B, Al, Ga or In) cause a concurrent increase in the concentration of V_{Zn}^{2-}. However, a direct observation of the donor-vacancy relation, or more precisely the dependence of V_{Zn} on the Fermi-level position, has not been unambiguously proven before. In Paper II, we have used a combination of SIMS and PAS to investigate Al-doped ZnO. The results directly demonstrate a quadratic relation between the Al-doping (SIMS) and the V_{Zn} concentration (PAS), thus establishing that V_{Zn}^{2-} is indeed the prevalent intrinsic defect in highly n-type ZnO. Furthermore, Paper II also demonstrate the effect of the Fermi-level position on the diffusion of Al, which is in line with that predicted by the reaction diffusion model when the background concentration of donors, i.e. Ga, is increased. These quasi-isoconcentration diffusion results support the generality of the model, which goes beyond the capability of other models, e.g., the Fair model, that does not describe the physical processes involved in the observed diffusion of Al. In addition, in Paper II we experimentally show that the V_{Zn}'s can be controlled by the annealing ambient, which also has not been demonstrated experimentally before, although it is in line with the theoretical predictions where zinc rich conditions results in a higher formation energy of V_{Zn}.

Paper III A diffusion study of the next group III element, In, is reported in Paper III, where similar dopant indiffusion experiments were carried out, and reveals a significant faster diffusion for In, as compared to that of Al and Ga. The character of the In diffusion, however, are more or less identical to Al and Ga. On the other hand, the diffusion experiments of In were influenced by a transport limit of

mobile In available in the film. The lower dopant concentration of In as compared to Al and Ga revealed an inadequacy in our RD model, incapable of determining the dopant-vacancy migration barrier at these moderate n-type conditions. Nevertheless, the results for In diffusion demonstrated self-consistency in the theoretical predictions by Ref.[73]. Furthermore, investigation of the deposited In-doped film by scanning transmission electron spectroscopy (see Appendix C) revealed the formation of In-rich lines that may be assigned to the formation of inversion domain boundaries decorated with In.

Paper IV During the experimental investigation of Al diffusion into Ga-doped ZnO (Paper II), an interesting feature was observed for unintentionally introduced Li (a common contaminator in the tube furnace). As the Ga-doped ZnO bulk were initially free for any significant amounts of Li, the indiffusion of Li became quite apparent. In the literature, a fast interstitial diffusion of Li is reported for temperatures up to $600°C$. However, at higher temperatures, i.e., up to $1150°C$, a different and slower diffusion mechanism is observed and this is the main topic of Paper IV.

The observed diffusion mechanism of Li at temperatures above $1000°C$ resulted in new experiments by depositing Li-doped ZnO thin films on uniformly Ga-doped ZnO wafers. Paper IV report the results of Li diffusion experiments performed over a wide temperature interval ($500-1150°C$), demonstrating the Li diffusion to be dictated by the Ga distribution. In accordance with previous diffusion studies, our results support a fast diffusion for Li that can be attributed to an interstitial-type mechanism for heat treatments below $\sim 800°C$, and reveal very distinct in-diffused Li-doped box regions with a close to one-to-one correlation between the Li and Ga concentrations. Heat treatments at higher temperatures reveal the emergence of a different diffusion process that is assigned to a dissociative mechanism by using a modified RD-model that considers the dissociation of substitutional Li into mobile Li interstitials. From this, an activation energy of 4.6 eV is obtained for the dissociation process. This is in excellent agreement with the predictions of an activation barrier of 4.8 eV for the dissociation of neutral $Li_{Zn}Ga_{Zn}$, as obtained from the DFT results, thus suggesting $Li_{Zn}Ga_{Zn}$ to be the dominating Li-related defect in Ga-doped ZnO.

Paper V For all the diffusion experiments conducted in this work, a thin film of ZnO doped with either Al, Ga, In or Li was grown onto HT ZnO single crystals. The deposition of these films have been realized by the use of magnetron sputtering, which is explained in more detail in Appendix B. In Paper V we report a detailed description of the deposition technique that has been used in this work.

Here, it is demonstrated that films with excellent crystal quality can be grown by this method, with a lattice match and close to epitaxial interface between the film and bulk, which is highly beneficial when conducting detailed in-diffusion experiments (Papers I-IV).

5.2 Preliminary results

5.2.1 Diffusion of Ga in Al-doped deposited thin films

In the study of Al diffusion in Ga-doped ZnO (Paper II), Ga was observed to migrate the opposite direction, i.e., into the deposited thin film, forming erfc-like diffusion profiles within the Al-doped film. This was not the main topic of Paper II, but by using simple erfc-modelling of the $800 - 900$°C Ga profiles results in a diffusion activation energy of $E_a = 2.3$ eV, in excellent agreement with the results for the migration energy barrier of $(Ga_{Zn}V_{Zn})^-$ obtained in Paper I. This may also support our notion (Paper I) that the diffusion of Ga proceeds by $(Ga_{Zn}V_{Zn})^-$, since an effectively infinite supply of V_{Zn}^{2-} in the highly n-type film would result in an overall diffusion activation energy that equates the migration energy barrier, i.e., there would be effectively no energy barrier for the formation of V_{Zn}^{2-} (see Ch.3.5). Surprisingly, however, the absolute value for the diffusivities was about two orders of magnitude lower than that of Ga diffusion in undoped ZnO (Paper I). That is, the diffusion constant (pre-exponential factor) obtained for the diffusion of Ga in the Al-doped film is reduced by two orders of magnitude to that observed in undoped ZnO.

A tentative explanation for this observation is that the high concentration of Al dopants in the deposited film effectively behaves as scattering centers for the migrating $(Ga_{Zn}V_{Zn})^-$ pairs. That is, the high density of Al results in an effectively longer migration path for Ga, which mathematically would be equivalent to a reduced correlation factor and thus a lower diffusion prefactor. In an attempt to explain this retarded diffusion of Ga, new experiments were designed by reducing the Al-doping in the film to 1×10^{20} cm^{-3} and 1×10^{19} cm^{-3}, in addition to increasing the film thickness. Only the latter deposition resulted in a quality film that could be studied, and results are shown in Fig.5.1. As can be seen, the shape of the Ga-diffusion profiles into the deposited film (left side) takes a slightly different form than that of the erfc-function demonstrated in the more heavily Al-doped film in Paper II. It clearly reveal a more convex shape, which is what one would expect when transitioning towards more moderately or undoped ZnO (cf. Paper I). However, the quality and number of data points are substandard for determination

of diffusion activation energy, and new experiments have to be conducted if to be explored further.

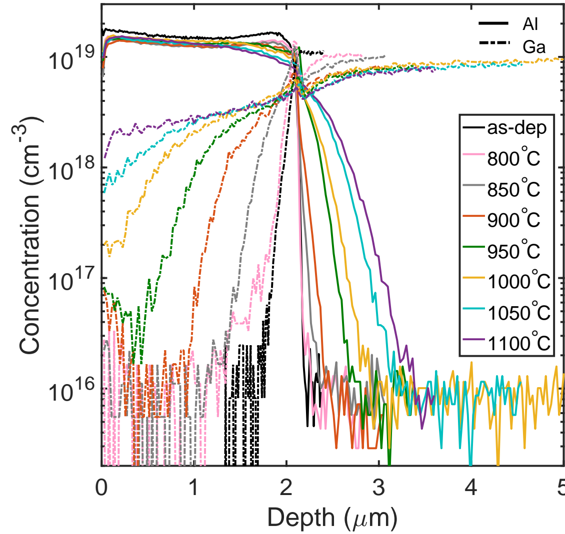

Figure 5.1: Al and Ga interdiffusion in the moderately Al-doped film deposited onto Ga-doped ZnO.

5.2.2 Diffusion of Al under varied background levels of dopants

In paper II we show that the diffusivity of Al is strongly affected by the presence of a background concentration of Ga (1×10^{19} cm^{-3}). However, experiments were also carried out with samples that were predoped with higher concentrations of Ga. Figure 5.2 shows the concentration vs depth profiles of Al and Ga in a similar system as that reported in Paper II, but with about one order of magnitude higher concentration of Ga. The results are consistent with that in Paper II with Ga starting to migrate into the deposited film at 800°C. The shape of the Al diffusion profiles also appears to resemble that of erfc-like profiles at high concentrations, but for low concentrations ($\sim 10^{18}$ cm^{-3}) the shape of the profiles takes a different (concave) form. This can, however, be ascribed to an instrumental artifact in the SIMS measurement, as the dynamic range of 5 orders of magnitude limits the measurement. As can be seen, this particular sample reveal a poor-quality feature at the film-bulk interface, complicating the SIMS measurements. It is therefore challenging to obtain quality modelling for these profiles, and new experiments should be performed in order to continue on this subject.

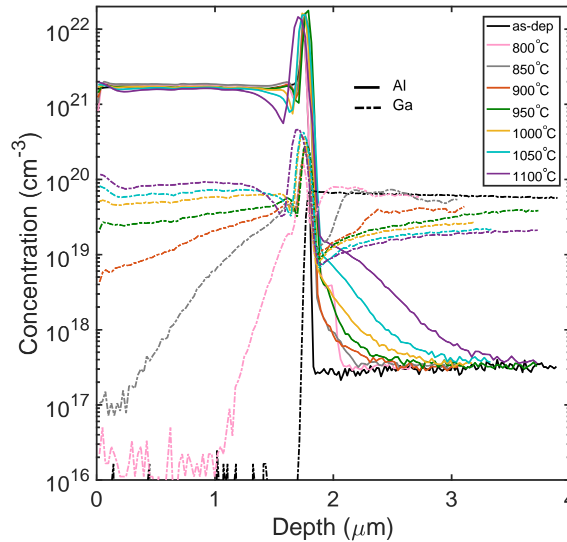

Figure 5.2: Al diffusion from heavily Al-doped deposited film into heavily Ga predoped (indiffused; $\sim 1 \times 10^{20}$ cm^{-3}) bulk.

5.2.3 Diffusion of In under increased donor background concentration

Similar to the Al diffusion in predoped ZnO (Paper II), this was also approached for the diffusion of In. The results, however, were much more incomprehensible, as can be seen in Fig.5.3. A diffusion is observed already at 800°C, with an increase in the concentration and depth as a function of temperature. The shape of the profiles also differs from that observed in undoped ZnO, resembling more of a free-diffusion like behaviour. Importantly, however, the concentration of In reveals a highly irregular In depth distribution. This may be a result of an inhomogeneous depth (and to some extent lateral) distribution of In. One possibility for these observation might be that In accumulates at local regions. However, this could not be directly observed in SIMS, so in that case its features must be smaller than the lateral resolution of a typical SIMS measurement ($< 1 - 3\mu$m).

The STEM results obtained from the In-doped ZnO film in Paper III, however, evidenced In-rich structures that was suggested to arise due to the formation of inversion boundary domains. It is tempting to speculate that this effect is also responsible for the peculiar In diffusion profiles obtained by SIMS in Fig.5.3. This, however, is merely speculations, and further studies should be conducted to understand this effect. It should be noted here that similar structures were observed also

for the Ga-doped film (Paper III), i.e., indications of inversion domain boundaries decorated by Ga. Moreover, inversion domain boundaries have previously been reported for several elements in ZnO, including In [116, 117], Fe [116, 117] and Li [118], suggesting that this is a rather common phenomenon in impurity doped ZnO.

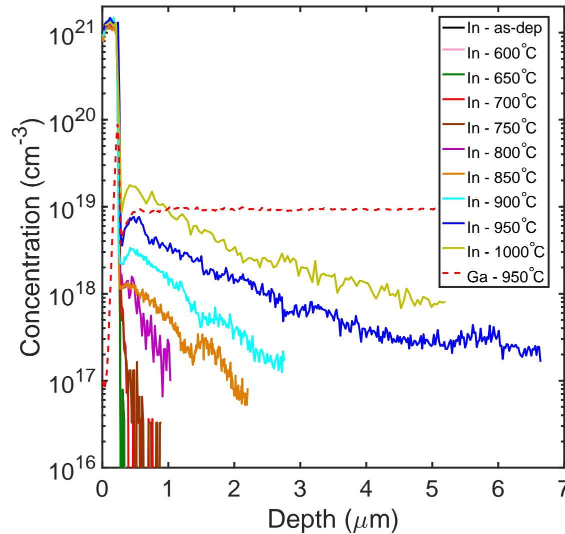

Figure 5.3: Concentration vs depth diffusion profiles of In in Ga-doped ZnO, from a 0.3μm thick In-doped ZnO deposited film.

5.3 Suggestions for further work

In paper IV we report that indiffusion of Li into Ga-containing ZnO up to $\sim 700°$C yields highly Li-doped regions with a very sharp drop in the Li concentation, separating the Li-containing and prestine bulk regions. The analysis performed at higher temperatures, indicated that the majority of Li in this region were configured as neutral $Li_{Zn}Ga_{Zn}$ pairs. That is, the indiffused Li, with a concentration similar to that of Ga, act as to neutralize the Ga donors, thus effectively compensate the material. This would imply the presence of an abrupt $n^{-} - n^{+}$ junction with a large potential gradient between the compensated and uncompensated region, resulting in an electric field pointing towards the surface.

These results may suggest a viable approach to create very abrupt isotype homojunctions with prospects of large built in voltage that is stable up to $\sim 700°$C. In addition, by increasing the background concentrations of Ga, may yield even

higher built in voltages. Importantly, however, further investigations using e.g., scanning spreading resistance profiling must be conducted in order to explore the electrical properties of the compensated region and proceed on this subject.

Furthermore, our results in Paper IV suggest that $Li_{Zn}Ga_{Zn}$ is the predominant Li-related defect in these samples (and not Li_{Zn}). Future investigations using e.g., photoluminescence conducted on similar structures may possibly provide signatures that can be compared to theoretical predictions and used to verify or disprove these results.

Paper II reports dopant diffusion under increased background donor concentrations, and Sec.5.2.2 above showed the attempts of a similar study under even higher background concentrations. Such experiments may be very valuable, since by studying e.g., Al diffusion under varying isoconcentration levels it should be possible to observe D_{Al} as a function of n. From this, one might construct a D_{Al} vs n plot where the relationship would yield the prevailing charge state for diffusion and hence enable a direct and unambiguous method to extract the charge state difference responsible for the diffusion mechanism.

On a more general note, the reaction-diffusion model has in this work proved successful for describing the vacancy mediated mechanism of donor dopants (Al, Ga and In) in Paper I-III, as well as for the dissociative diffusion mechanism of Li in Paper IV. A next step, would be to apply the model for other elements that also predominates the Zn sub-lattice. Moreover, it would certainly be interesting to test the model on impurities that prefers the O sub-lattice, e.g., nitrogen (although experimental results are scarce). A possible route could be to perform nitrogen diffusion studies in Zn-rich ambient, in order to increase the concentration of V_O. Finally, it should be emphasized that the reaction-diffusion model employed and further developed in the present work can in principle be applied also for other novel material systems, such as e.g., Ga_2O_3.

Appendix A

Density functional theory

Since the exeprimental results of impurity diffusion obtained in this work are frequently compared to results from density functional theory (DFT) calculations, it is appropriate with a short introduction to DFT.

On the basis of quantum mechanical considerations it is possible to investigate the electronic structure of a crystal lattice using computational modelling. This can be done quite effectively through the use of functionals of the electron density, a method known as DFT. The essence of such DFT calculation is to calculate the ground state energy for the valence electrons associated with the ions located at well defined positions in a crystal lattice.

DFT rests on a set of mathematical theorems proved by Hohenberg and Kohn in 1964 [119] together with a set of equations derived one year later by Kohn and Sham [120] in order to actually realize the electronic structure calculations. In brief, the theorems states that there exist a one-to-one mapping between the ground state wave function ψ and the ground state electron density n, and that the true electron density is the one that minimizes the energy of the overall functional [119]. This means that the energy of a single electron can be calculated by solving the single-particle Schödinger equation:[121, 16]

$$\left[-\frac{\hbar^2\nabla^2}{2m_e}+V^{\text{eff}}(\mathbf{r})\right]\psi_i=\varepsilon_i\psi_i, \tag{A.1}$$

where the first term is the kinetic energy operator and the second term is given by

$$V^{\text{eff}}(\mathbf{r})=V_{\text{ion}}(\mathbf{r})+e^2\int\frac{n(\mathbf{r}')}{|\mathbf{r}-\mathbf{r}'|}d^3r'+V_{XC}. \tag{A.2}$$

Here $V_{\text{ion}}(\mathbf{r})$ is the potential due to the ions, whereas the second term is the Hartree potential describing the electrostatic interaction between electrons. The final potential term in (A.2) is an exchange-correlation term V_{XC}. The exchange energy arise due to the Pauli exclusion principle (electrons cannot occupy identical states), while correlation energy effects must be taken into account because of the approximate representation of the electron-electron Coulomb repulsion in the Hartree potential.

The single-particle Schödinger equation / Kohn-Sham equations (A.1) will provide the wave functions ψ_i, which in turn provides the electron density by $n(\mathbf{r}) = \sum_i |\psi_i(\mathbf{r})|^2$. However, to solve (A.1) we need to know the electron density (Hartree potential). Hence the system needs to be solved iteratively, by first making an initial guess of $n(\mathbf{r})$, find ψ_i by solving (A.1), calculate the new $n(\mathbf{r})$ and compare/redo until the $n(\mathbf{r})$ has converged. When the two densities are the same (converged), this is the ground state $n(\mathbf{r})$, and the total energy of the system can be calculated.

Inconveniently though, the true form of the exchange-correlation energy functional is not known, and therefore nor does a solution of n($\mathbf{r}$). However, well functioning approximations for the V_{XC} term exist, and one commonly used is the local density approximation (LDA) where the energy functional depends only on the value of $n(\mathbf{r}')$ equal of that of a uniform electron gas (density same everywhere). More sophisticated approximations can be made by extending the LDA by also accounting for the gradient of $n(\mathbf{r}')$, known as generalized-gradient approximation (GGA).

Using LDA or GGA approximations is notoriously known to underestimate the band gap, especially in the case for wide band gap semiconductors such as ZnO [56]. This can be improved by using so-called hybrid functionals that intermix the exact Hartree-Fock (HF) exchange with the exchange-correlation from the LDA or GGA functionals. This method is a semi-empirical approach where the mixing parameters are adjusted empirically, that is, such that accurate band gaps and lattice parameters can be obtained. In this work, we have used the Heyd-Scuseria-Ernzerhof (HSE) hybrid functional [122], that intermixes a portion of the screened HF exchange with GGA functionals.

Appendix B

Thin film growth by sputter deposition

For all the impurity indiffusion experiments conducted in this work, a thin film of impurity doped ZnO was deposited by means of a sputter deposition technique. Therefore, it may be suitable with a short introduction of sputter deposition.

The growth of thin films by sputter deposition is a widely used technique in the manufacturing of thin-film based devices that requires both high throughput and good crystalline quality. The process of sputtering was presented in Sec.4.1.2 in the discussion of SIMS, where the sputtered/ejected and ionized target particles were analyzed carefully to obtain elemental information of the target material. For thin-film sputter deposition, however, the sputtered target material is directly deposited onto the surface of a neareby substrate.

By creating a plasma of positive ions (usually Ar^+) inside a pre-evacuated chamber between a negatively biased target material (cathode) and a substrate (anode), the positively charged ions in the plasma are accelerated toward the target material. When they strike the surface, target particles (atoms, ions and molecules) is ejected from the surface, and may travel accross the chamber to be deposited on the oppositely directed substrate. Secondary electrons are also released when Ar^+ bombard the target, and will instantly be accelerated away from the cathode. In this process, the secondary electrons may collide with neutral Ar atoms, thus ionizing additional atoms in the plasma, such that the plasma is self-sustaining while sputtering occurs.

Only a small fraction of the inert gas is ionized ($\sim 0.001\%$ [123]), which means that the sputter rate is rather low in this arrangement. This may be improved by applying a magnetic field accross the target, such that the released secondary

electrons will follow a helical path towards the anode. This arrangement is known as magnetron sputtering, and increases the secondary electrons pathlength and probability of collision with- and ionization of neutral Ar.

In this work, a Semicore Tri-Axis balanced field magnetron sputtering system has been used to deposit impurity-doped ZnO films onto single crystalline ZnO bulk wafers.

Appendix C

Scanning Transmission Electron Microscopy

In Paper III, the sputter deposited films were analysed by scanning transmission electron microscopy (STEM) imaging. It may therefore be appropriate with a brief introduction to the STEM technique.

STEM is a technique that scans a finely focused beam of electrons in a raster pattern accross a very thin sample. It is primarily the electrons that are transmitted through the sample that are imaged and analyzed. For that reason, the tickness of the sample should be below a few hundred nanometers, however, thinner is almost always better [124]. Resolutions as good as 0.05 nm can be achieved using this technique.

The electron column in a STEM setup includes an electron source and a set of electromagnetic lenses that forms the focused electron beam at the sample. During electron bombardement, the beam electrons that impinges the sample may be transmitted unaffected to form a bright field (BF) image on e.g., a fluorescent screen or a charged-coupled device camera, or they may be affected by several possible mechanisms. In particular, the electron beam may be elastically scattered by the nuclei of the target atoms. The transmitted beam electrons that happens to be scattered through a relatively large angle can be detected using a high angle annular dark field (HAADF) detector, where the intensity will be a function of the average atomic number of the probed volume, thus enabeling atomic contrast, or Z-contrast in the image. This method works well for distinguishing elements with significant difference in the atomic number, e.g., for In and Zn, and was used in Paper III to observe In-rich columns in the deposited In-doped ZnO film. For atoms with more similar atomic number, such as Ga and Zn, the HAADF method

may be challenging. However, elemental composition may also be obtained by analysing the characteristic X-rays that are emitted by sample atoms as they are ionized by the electron beam. An energy-dispersive X-ray (EDX) spectrometer is used to count and sort the charactersitic X-rays according to their energies, producing an energy spectrum with destinctive peaks for the elements present. This was utilized in the analysis of the Ga-doped ZnO deposited film, in order to confirm that the features observed in an angle annular dark field (ADF) detector were related to Ga-rich columns.

In this work, the STEM imaging was performed using a FEI Titan G2 60-300 at 300 kV with a convergence angle of 30 mrad, where the energy-dispersive X-ray spectroscopy was performed using a Bruker Super-X quad detector. The STEM samples were prepared by conventional means of grinding and polishing.

References

[1] Tudor Jenkins. A brief history of ... semiconductors. *Phys. Educ.*, 40(5):430, 2005.

[2] Alan Herries Wilson. The theory of electronic semi-conductors. *Proc. R. Soc. Lond. A*, 133(822):458–491, October 1931.

[3] Chennupati Jagadish and Stephen J. Pearton. *Zinc Oxide Bulk, Thin Films and Nanostructures: Processing, Properties, and Applications*. Elsevier, October 2011.

[4] Sol E. Harrison. Conductivity and Hall Effect of ZnO at Low Temperatures. *Phys. Rev.*, 93(1):52–62, January 1954.

[5] Ü Özgür, Ya I. Alivov, C. Liu, A. Teke, M. A. Reshchikov, S. Doğan, V. Avrutin, S.-J. Cho, and H. Morkoç. A comprehensive review of ZnO materials and devices. *Journal of Applied Physics*, 98(4):041301, August 2005.

[6] U. Ozgur, Daniel Hofstetter, and Hadis Morkoc. ZnO Devices and Applications: A Review of Current Status and Future Prospects. *Proceedings of the IEEE*, 98(7):1255–1268, July 2010.

[7] V. Avrutin, D.J. Silversmith, and Hadis Morkoc. Doping Asymmetry Problem in ZnO: Current Status and Outlook. *Proceedings of the IEEE*, 98(7):1269–1280, July 2010.

[8] S. J. Pearton, D. P. Norton, K. Ip, Y. W. Heo, and T. Steiner. Recent progress in processing and properties of ZnO. *Progress in Materials Science*, 50(3):293–340, March 2005.

[9] Tadatsugu Minami, Hirotoshi Sato, Hidehito Nanto, and Shinzo Takata. Group III Impurity Doped Zinc Oxide Thin Films Prepared by RF Magnetron Sputtering. *Jpn. J. Appl. Phys.*, 24(10A):L781, October 1985.

[10] D. C. Look, K. D. Leedy, L. Vines, B. G. Svensson, A. Zubiaga, F. Tuomisto, D. R. Doutt, and L. J. Brillson. Self-compensation in semiconductors: The Zn vacancy in Ga-doped ZnO. *Phys. Rev. B*, 84(11):115202, September 2011.

[11] J. Nause and B. Nemeth. Pressurized melt growth of ZnO boules. *Semicond. Sci. Technol.*, 20(4):S45, 2005.

[12] Lasse Vines and Andrej Kuznetsov. Bulk Growth and Impurities. In *Oxide Semiconductors*, volume 88, pages 67–104. ELSEVIER ACADEMIC PRESS INC 525 B STREET, SUITE 1900, SAN DIEGO, CA 92101-4495 USA, 2013.

[13] Katsumi Maeda, Mitsuru Sato, Ikuo Niikura, and Tsuguo Fukuda. Growth of 2 inch ZnO bulk single crystal by the hydrothermal method. *Semicond. Sci. Technol.*, 20(4):S49, 2005.

[14] Wenwen Lin, Dagui Chen, Jiye Zhang, Zhang Lin, Jiakui Huang, Wei Li, Yonghao Wang, and Feng Huang. Hydrothermal Growth of ZnO Single Crystals with High Carrier Mobility. *Crystal Growth & Design*, 9(10):4378–4383, October 2009.

[15] Wenwen Lin, Kai Ding, Zhang Lin, Jiye Zhang, Jiakui Huang, and Feng Huang. The growth and investigation on Ga-doped ZnO single crystals with high thermal stability and high carrier mobility. *CrystEngComm*, 13(10):3338–3341, 2011.

[16] David J. Griffiths. *Introduction to Quantum Mechanics*. Cambridge University Press, Cambridge, 2 edition edition, August 2016.

[17] Jenny Nelson. *PHYSICS OF SOLAR CELLS, THE*. ICP, London : River Edge, NJ, 1 edition edition, May 2003.

[18] Chris G. Van de Walle and J. Neugebauer. Universal alignment of hydrogen levels in semiconductors, insulators and solutions. *Nature*, 423(6940):626–628, June 2003.

[19] D. C. Look, J. W. Hemsky, and J. R. Sizelove. Residual Native Shallow Donor in ZnO. *Phys. Rev. Lett.*, 82(12):2552–2555, March 1999.

[20] A. F. Kohan, G. Ceder, D. Morgan, and Chris G. Van de Walle. First-principles study of native point defects in ZnO. *Phys. Rev. B*, 61(22):15019–15027, June 2000.

[21] Anderson Janotti and Chris G. Van de Walle. Native point defects in ZnO. *Phys. Rev. B*, 76(16):165202, October 2007.

[22] D. G. Thomas. Interstitial zinc in zinc oxide. *Journal of Physics and Chemistry of Solids*, 3(3):229–237, January 1957.

[23] C. Bhoodoo, A. Hupfer, L. Vines, E. V. Monakhov, and B. G. Svensson. Evolution kinetics of elementary point defects in ZnO implanted with low fluences of helium at cryogenic temperature. *Phys. Rev. B*, 94(20):205204, November 2016.

[24] M. D. McCluskey and S. J. Jokela. Sources of n-type conductivity in ZnO. *Physica B: Condensed Matter*, 401-402:355–357, December 2007.

[25] L. Vines, E. V. Monakhov, R. Schifano, W. Mtangi, F. D. Auret, and B. G. Svensson. Lithium and electrical properties of ZnO. *Journal of Applied Physics*, 107(10):103707, May 2010.

[26] K. M. Johansen, A. Zubiaga, I. Makkonen, F. Tuomisto, P. T. Neuvonen, K. E. Knutsen, E. V. Monakhov, A. Yu. Kuznetsov, and B. G. Svensson. Identification of substitutional Li in \$n\$-type ZnO and its role as an acceptor. *Phys. Rev. B*, 83(24):245208, June 2011.

[27] Tadatsugu Minami. Chapter Five - Transparent Conductive Oxides for Transparent Electrode Applications. In Bengt G. Svensson, Stephen J. Pearton, and Chennupati Jagadish, editors, *Semiconductors and Semimetals*, volume 88 of *Oxide Semiconductors*, pages 159–200. Elsevier, January 2013.

[28] Tadatsugu Minami. New n-Type Transparent Conducting Oxides. *MRS Bulletin*, 25(8):38–44, August 2000.

[29] Tadatsugu Minami. Substitution of transparent conducting oxide thin films for indium tin oxide transparent electrode applications. *Thin Solid Films*, 516(7):1314–1321, February 2008.

[30] Tadatsugu Minami, Toshihiro Miyata, Yuusuke Ohtani, and Takeshi Kuboi. Effect of thickness on the stability of transparent conducting impurity-doped ZnO thin films in a high humidity environment. *physica status solidi (RRL) – Rapid Research Letters*, 1(1):R31–R33, 2006.

[31] W. Beyer, J. Hüpkes, and H. Stiebig. Transparent conducting oxide films for thin film silicon photovoltaics. *Thin Solid Films*, 516(2):147–154, December 2007.

[32] Tadatsugu Minami, Toshihiro Miyata, and Jun-ichi Nomoto. Impurity-doped ZnO Thin Films Prepared by Physical Deposition Methods Appropriate for Transparent Electrode Applications in Thin-film Solar Cells. *IOP Conf. Ser.: Mater. Sci. Eng.*, 34(1):012001, 2012.

[33] Mercedes Gabás, Angel Landa-Cánovas, José Luis Costa-Krämer, Fernando Agulló-Rueda, Agustín R. González-Elipe, Pilar Díaz-Carrasco, Jorge Hernández-Moro, Israel Lorite, Pilar Herrero, Pedro Castillero, Angel Barranco, and José Ramón Ramos-Barrado. Differences in n-type doping efficiency between Al- and Ga-ZnO films. *Journal of Applied Physics*, 113(16):163709, April 2013.

[34] N. Yamamoto, H. Makino, S. Osone, A. Ujihara, T. Ito, H. Hokari, T. Maruyama, and T. Yamamoto. Development of Ga-doped ZnO transparent electrodes for liquid crystal display panels. *Thin Solid Films*, 520(12):4131–4138, April 2012.

[35] Tadatsugu Minami, Takeshi Kuboi, Toshihiro Miyata, and Yuusuke Ohtani. Stability in a high humidity environment of TCO thin films deposited at low temperatures. *phys. stat. sol. (a)*, 205(2):255–260, February 2008.

[36] Jun-ichi Nomoto, Manabu Konagai, Kenji Okada, Tomoyuki Ito, Toshihiro Miyata, and Tadatsugu Minami. Comparative study of resistivity characteristics between transparent conducting AZO and GZO thin films for use at high temperatures. *Thin Solid Films*, 518(11):2937–2940, March 2010.

[37] F. Tuomisto, V. Ranki, K. Saarinen, and D C. Look. Evidence of the Zn Vacancy Acting as the Dominant Acceptor in n-Type ZnO. *Phys. Rev. Lett.*, 91(20):205502, November 2003.

[38] F. Tuomisto, K. Saarinen, D. C. Look, and G. C. Farlow. Introduction and recovery of point defects in electron-irradiated ZnO. *Phys. Rev. B*, 72(8):085206, August 2005.

[39] J. E. Stehr, K. M. Johansen, T. S. Bjorheim, L. Vines, B. G. Svensson, W. M. Chen, and I. A. Buyanova. Zinc-Vacancy–Donor Complex: A Crucial Compensating Acceptor in ZnO. *Phys. Rev. Applied*, 2(2):021001, August 2014.

[40] J. E. Stehr, W. M. Chen, B. G. Svensson, and I. A. Buyanova. Thermal stability of the prominent compensating (AlZn–VZn) center in ZnO. *Journal of Applied Physics*, 119(10):105702, March 2016.

[41] Mehrer, H. Heroes and highlights in the history of diffusion. Diffusion Fundamentals. *Diffusion Fundamentals*, 11(1), 2009.

[42] Horng-Ming You, Ulrich M. Gösele, and Teh Y. Tan. Simulation of the transient indiffusion-segregation process of triply negatively charged Ga vacancies in GaAs and AlAs/GaAs superlattices. *Journal of Applied Physics*, 74(4):2461–2470, August 1993.

[43] J. Crank. *The Mathematics of Diffusion*. CLARENDON PRESS OXFORD, 2 edition, 1975.

[44] M. Lannoo. *Point Defects in Semiconductors I: Theoretical Aspects*. Springer Series in Solid-State Sciences. Springer-Verlag, Berlin Heidelberg, 1981.

[45] P. M. Fahey, P. B. Griffin, and J. D. Plummer. Point defects and dopant diffusion in silicon. *Rev. Mod. Phys.*, 61(2):289–384, April 1989.

[46] Carl Angell, Bjørn Ebbe Lian. Fysiske størrelser og enheter, March 2009.

[47] S. M. Hu. General Theory of Impurity Diffusion in Semiconductors via the Vacancy Mechanism. *Phys. Rev.*, 180(3):773–784, April 1969.

[48] Jean-Marc Philibert. *Atom movements - Diffusion and mass transport in solids*. EDP Sciences, December 2012.

[49] Svante Arrhenius. Über die Reaktionsgeschwindigkeit bei der Inversion von Rohrzucker durch Säuren. *Zeitschrift für Physikalische Chemie*, 4U(1):226–248, 1889.

[50] S. R. Logan. The origin and status of the Arrhenius equation. *J. Chem. Educ.*, 59(4):279, April 1982.

[51] Jean Philibert. Some Thoughts and/or Questions about Activation Energy and Pre-Exponential Factor, 2006.

[52] A. Yelon, B. Movaghar, and H. M. Branz. Origin and consequences of the compensation (Meyer-Neldel) law. *Phys. Rev. B*, 46(19):12244–12250, November 1992.

[53] K. L. Narasimhan and B. M. Arora. The capture cross-section and the Meyer-Neldel rule in III–V compound semiconductors. *Solid State Communications*, 55(7):615–617, August 1985.

[54] A. Yelon and B. Movaghar. Microscopic explanation of the compensation (Meyer-Neldel) rule. *Phys. Rev. Lett.*, 65(5):618–620, July 1990.

[55] Heidemarie Schmidt, Maria Wiebe, Beatrice Dittes, and Marius Grundmann. Meyer-Neldel rule in ZnO. *Appl. Phys. Lett.*, 91(23):232110, December 2007.

[56] Christoph Freysoldt, Blazej Grabowski, Tilmann Hickel, Jörg Neugebauer, Georg Kresse, Anderson Janotti, and Chris G. Van de Walle. First-principles calculations for point defects in solids. *Rev. Mod. Phys.*, 86(1):253–305, March 2014.

[57] Ben Streetman and Sanjay Banerjee. *Solid State Electronic Devices*. Prentice Hall, Upper Saddle River, N.J, 6 edition edition, August 2005.

[58] Kenneth J. Button, Daniel R. Cohn, Michael von Ortenbert, Benjamin Lax, E. Mollwo, and R. Helbig. Zeeman Splitting of Anomalous Shallow Bound States in ZnO. *Phys. Rev. Lett.*, 28(25):1637–1639, June 1972.

[59] G. Beni and T. M. Rice. Theory of electron-hole liquid in semiconductors. *Phys. Rev. B*, 18(2):768–785, July 1978.

[60] Kurt Lehovec and Alexis Slobodskoy. Diffusion of charged particles into a semiconductor under consideration of the built-in field. *Solid-State Electronics*, 3(1):45–50, July 1961.

[61] Seeger A. and Chik K. P. Diffusion Mechanisms and Point Defects in Silicon and Germanium. *physica status solidi (b)*, 29(2):455–542, 1968.

[62] R. B. Fair and J. C. C. Tsai. A Quantitative Model for the Diffusion of Phosphorus in Silicon and the Emitter Dip Effect. *J. Electrochem. Soc.*, 124(7):1107–1118, July 1977.

[63] U. M. Gosele. Fast Diffusion in Semiconductors. *Annual Review of Materials Science*, 18(1):257–282, 1988.

[64] H. Bracht. Self- and foreign-atom diffusion in semiconductor isotope heterostructures. I. Continuum theoretical calculations. *Phys. Rev. B*, 75(3):035210, January 2007.

[65] L. L. Chang and G. L. Pearson. Diffusion Mechanism of Zn in GaAs and GaP Based on Isoconcentration Diffusion Experiments. *Journal of Applied Physics*, 35(6):1960–1965, June 1964.

[66] B. J. Masters and J. M. Fairfield. Arsenic Isoconcentration Diffusion Studies in Silicon. *Journal of Applied Physics*, 40(6):2390–2394, May 1969.

[67] J. S. Makris and B. J. Masters. Gallium Diffusions into Silicon and Boron-Doped Silicon. *Journal of Applied Physics*, 42(10):3750–3754, September 1971.

[68] E. Antoncik. Theory of Isoconcentration Diffusion in Semiconductors. *J. Electrochem. Soc.*, 142(9):3170–3173, September 1995.

[69] A. Nylandsted Larsen, P. Kringho/j, J. Lundsgaard Hansen, and S. Yu. Shiryaev. Isoconcentration studies of antimony diffusion in silicon. *Journal of Applied Physics*, 81(5):2173–2178, March 1997.

[70] E. Antoncik. The influence of the solubility limit on diffusion of as implants in silicon. *Appl. Phys. A*, 56(4):291–298, April 1993.

[71] K. M. Johansen, L. Vines, T. S. Bjorheim, R. Schifano, and B. G. Svensson. Aluminum Migration and Intrinsic Defect Interaction in Single-Crystal Zinc Oxide. *Phys. Rev. Applied*, 3(2):024003, February 2015.

[72] D. O. Demchenko, B. Earles, H. Y. Liu, V. Avrutin, N. Izyumskaya, Ü. Özgür, and H. Morkoç. Impurity complexes and conductivity of Ga-doped ZnO. *Phys. Rev. B*, 84(7):075201, August 2011.

[73] Daniel Steiauf, John L. Lyons, Anderson Janotti, and Chris G. Van de Walle. First-principles study of vacancy-assisted impurity diffusion in ZnO. *APL Materials*, 2(9):096101, September 2014.

[74] Y. K. Frodason, K. M. Johansen, T. S. Bjørheim, B. G. Svensson, and A. Alkauskas. Zn vacancy as a polaronic hole trap in ZnO. *Phys. Rev. B*, 95(9):094105, March 2017.

[75] R. Hauschild, H. Priller, M. Decker, J. Brückner, H. Kalt, and C. Klingshirn. Temperature dependent band gap and homogeneous line broadening of the exciton emission in ZnO. *Phys. Status Solidi (c)*, 3(4):976–979, March 2006.

[76] D. G. Thomas and J. J. Lander. Hydrogen as a Donor in Zinc Oxide. *The Journal of Chemical Physics*, 25(6):1136–1142, December 1956.

[77] D. G. Thomas. The diffusion and precipitation of Indium in Zinc Oxide. *Journal of Physics and Chemistry of Solids*, 9(1):31–42, January 1959.

[78] J. J. Lander. Reactions of Lithium as a donor and an acceptor in ZnO. *Journal of Physics and Chemistry of Solids*, 15(3):324–334, October 1960.

[79] K. Ip, M. E. Overberg, Y. W. Heo, D. P. Norton, S. J. Pearton, C. E. Stutz, B. Luo, F. Ren, D. C. Look, and J. M. Zavada. Hydrogen incorporation and diffusivity in plasma-exposed bulk ZnO. *Appl. Phys. Lett.*, 82(3):385–387, January 2003.

[80] N. H. Nickel. Hydrogen migration in single crystal and polycrystalline zinc oxide. *Phys. Rev. B*, 73(19):195204, May 2006.

[81] K. M. Johansen, J. S. Christensen, E. V. Monakhov, A. Yu Kuznetsov, and B. G. Svensson. Deuterium diffusion and trapping in hydrothermally grown single crystalline ZnO. *Applied Physics Letters*, 93(15):152109, October 2008.

[82] Isao Sakaguchi, Yutaka Adachi, Takeshi Ogaki, Kenji Matsumoto, Shunichi Hishita, Hajime Haneda, and Naoki Ohashi. Impurity Contamination and Diffusion during Annealing in Implanted ZnO, 2009.

[83] Isao Sakaguchi, Ken Watanabe, Yutaka Adachi, Takeshi Ohgaki, Shunichi Hishita, Naoki Ohashi, and Hajime Haneda. Simultaneous Diffusion of Oxygen Tracer and Lithium Impurity in Aluminum Doped Zinc Oxide. *Jpn. J. Appl. Phys.*, 50(12R):125501, November 2011.

[84] K. E. Knutsen, K. M. Johansen, P. T. Neuvonen, B. G. Svensson, and A. Yu. Kuznetsov. Diffusion and configuration of Li in ZnO. *Journal of Applied Physics*, 113(2):023702, January 2013.

[85] Pekka T. Neuvonen, Lasse Vines, Andrej Yu. Kuznetsov, Bengt G. Svensson, Xiaolong Du, Filip Tuomisto, and Anders Hallén. Interaction between Na and Li in ZnO. *Appl. Phys. Lett.*, 95(24):242111, December 2009.

[86] Pekka Tapio Neuvonen, Lasse Vines, Klaus Magnus Johansen, Anders Hallén, Bengt Gunnar Svensson, and Andrej Yu. Kuznetsov. Transportation of Na and Li in Hydrothermally Grown ZnO. In *Symposium H – Zinc Oxide and Related Materials-2009*, volume 1201 of *MRS Online Proceedings Library*, January 2009.

[87] L. Vines, P.t. Neuvonen, A. Yu. Kuznetsov, J. Wong-Leung, C. Jagadish, and B.g. Svensson. Anomalous Diffusion of Intrinsic Defects in K+ Implanted ZnO using Li as Tracer. In *Symposium M – Oxide Semiconductors–Defects, Growth and Device Fabrication*, volume 1394 of *MRS Online Proceedings Library*, January 2012.

[88] F. W. Kleinlein and R. Helbig. Diffusionskonstante und charakteristische Absorption vor der Bandkante von Mn in ZnO-Kristallen. *Z. Physik*, 266(3):201–207, June 1974.

[89] Thomas Neset Sky. Nickel Diffusion and Configuration in Crystalline Zinc Oxide. *MSc thesis, Dep. of Physics University of Oslo*, 2014.

[90] G. Müller and R. Helbig. Über den Einbau von Kupfer in ZnO-Einkristallen. *Journal of Physics and Chemistry of Solids*, 32(8):1971–1977, January 1971.

[91] Eva Holthe Enoksen. Diffusjon av potensielle p-type dopantar i monokrystallinsk ZnO. *MSc thesis, Dep. of Physics University of Oslo*, 2016.

[92] VJ Norman. The diffusion of aluminium and gallium in zinc oxide. *Aust. J. Chem.*, 22(2):325–329, January 1969.

[93] Tsubasa Nakagawa, Isao Sakaguchi, Masashi Uematsu, Yoshiyuki Sato, Naoki Ohashi, Hajime Haneda, and Yuichi Ikuhara. Diffusion Model of Gallium in Single-Crystal ZnO Proposed from Analysis of Concentration-Dependent Profiles Based on the Fermi-Level Effect. *Jpn. J. Appl. Phys.*, 46(7R):4099, July 2007.

[94] Alexander Azarov, Lasse Vines, Protima Rauwel, Edouard Monakhov, and Bengt G. Svensson. Silver migration and trapping in ion implanted ZnO single crystals. *Journal of Applied Physics*, 119(18):185705, May 2016.

[95] I. Sakaguchi, D. Park, Y. Takata, S. Hishita, N. Ohashi, H. Haneda, and T. Mitsuhashi. An effect of annealing on In implanted ZnO. *Nuclear Instruments and Methods in Physics Research Section B: Beam Interactions with Materials and Atoms*, 206:153–156, May 2003.

[96] Tsubasa Nakagawa, Kenji Matsumoto, Isao Sakaguchi, Masashi Uematsu, Hajime Haneda, and Naoki Ohashi. Analysis of Indium Diffusion Profiles Based on the Fermi-Level Effect in Single-Crystal Zinc Oxide. *Jpn. J. Appl. Phys.*, 47(10R):7848, October 2008.

[97] C. Liu, F. Yun, and H. Morkoç. Ferromagnetism of ZnO and GaN: A Review. *J Mater Sci: Mater Electron*, 16(9):555, September 2005.

[98] Antônio Claret Soares Sabioni, Marcelo José Ferreira Ramos, and Wilmar Barbosa Ferraz. Oxygen diffusion in pure and doped ZnO. *Materials Research*, 6(2):173–178, June 2003.

[99] Antônio Claret Soares Sabioni. About the oxygen diffusion mechanism in ZnO. *Solid State Ionics*, 170(1–2):145–148, May 2004.

[100] Paul Erhart and Karsten Albe. First-principles study of migration mechanisms and diffusion of oxygen in zinc oxide. *Phys. Rev. B*, 73(11):115207, March 2006.

[101] Joseph John Thomson. Bakerian Lecture:—Rays of positive electricity. *Proc. R. Soc. Lond. A*, 89(607):1–20, August 1913.

[102] Fred Stevie. *Secondary Ion Mass Spectrometry: Applications for Depth Profiling and Surface Characterization*. Momentum Press, September 2015. Google-Books-ID: UXe0CgAAQBAJ.

[103] K. S. Woodcock. The Emission of Negative Ions under the Bombardment of Positive Ions. *Phys. Rev.*, 38(9):1696–1703, November 1931.

[104] PC Zalm. Special Issue Surface Science Techniques Secondary ion mass spectrometry. *Vacuum*, 45(6):753–772, June 1994.

[105] Peter Sigmund. Theory of Sputtering. I. Sputtering Yield of Amorphous and Polycrystalline Targets. *Phys. Rev.*, 184(2):383–416, August 1969.

[106] Margareta K. Linnarsson. Compound semiconductors : defects and relocation of atoms during growth sputtering and diffusion. *DIVA*, 1997.

[107] Carl D. Anderson. The Positive Electron. *Phys. Rev.*, 43(6):491–494, March 1933.

[108] Paul Adrien Maurice Dirac. The quantum theory of the electron. *Proc. R. Soc. Lond. A*, 117(778):610–624, February 1928.

[109] Filip Tuomisto and Ilja Makkonen. Defect identification in semiconductors with positron annihilation: Experiment and theory. *Rev. Mod. Phys.*, 85(4):1583–1631, November 2013.

[110] S. Valkealahti and R. M. Nieminen. Monte-Carlo calculations of keV electron and positron slowing down in solids. *Appl. Phys. A*, 32(2):95–106, October 1983.

[111] S. Valkealahti and R. M. Nieminen. Monte Carlo calculations of keV electron and positron slowing down in solids. II. *Appl. Phys. A*, 35(1):51–59, September 1984.

[112] H. E. Hansen and U. Ingerslev-Jensen. Penetration of fast electrons and positrons. *J. Phys. D: Appl. Phys.*, 16(7):1353, 1983.

[113] K. Saarinen, S. Kuisma, J. Mäkinen, P. Hautojärvi, M. Törnqvist, and C. Corbel. Introduction of metastable vacancy defects in electron-irradiated semi-insulating GaAs. *Phys. Rev. B*, 51(20):14152–14163, May 1995.

[114] Filip Tuomisto. Chapter Two - Open Volume Defects: Positron Annihilation Spectroscopy. In Bengt G. Svensson, Stephen J. Pearton, and Chennupati Jagadish, editors, *Semiconductors and Semimetals*, volume 88 of *Oxide Semiconductors*, pages 39–65. Elsevier, January 2013.

[115] A. Zubiaga, F. Tuomisto, V. A. Coleman, H. H. Tan, C. Jagadish, K. Koike, S. Sasa, M. Inoue, and M. Yano. Mechanisms of electrical isolation in O+-irradiated ZnO. *Phys. Rev. B*, 78(3):035125, July 2008.

[116] H. Schmid and W. Mader. Distribution of Fe and In dopants in ZnO: A combined EELS/EDS analysis. In Martina Luysberg, Karsten Tillmann, and Thomas Weirich, editors, *EMC 2008 14th European Microscopy Congress 1–5 September 2008, Aachen, Germany*, pages 431–432. Springer Berlin Heidelberg, 2008.

[117] H. Schmid, E. Okunishi, and W. Mader. Defect structures in ZnO studied by high-resolution structural and spectroscopic imaging. *Ultramicroscopy*, 127:76–84, April 2013.

[118] K. M. Johansen, H. Haug, Ø Prytz, P. T. Neuvonen, K. E. Knutsen, L. Vines, E. V. Monakhov, A. Yu Kuznetsov, and B. G. Svensson. Li and OH-Li Complexes in Hydrothermally Grown Single-Crystalline ZnO. *Journal of Elec Materi*, 40(4):429–432, November 2010.

[119] P. Hohenberg and W. Kohn. Inhomogeneous Electron Gas. *Phys. Rev.*, 136(3B):B864–B871, November 1964.

[120] W. Kohn and L. J. Sham. Self-Consistent Equations Including Exchange and Correlation Effects. *Phys. Rev.*, 140(4A):A1133–A1138, November 1965.

[121] David Sholl and Janice A. Steckel. *Density Functional Theory: A Practical Introduction*. Wiley-Interscience, Hoboken, N.J, 1 edition edition, April 2009.

[122] Jochen Heyd, Gustavo E. Scuseria, and Matthias Ernzerhof. Hybrid functionals based on a screened Coulomb potential. *The Journal of Chemical Physics*, 118(18):8207–8215, April 2003.

[123] Stephen A. Campbell. *Fabrication Engineering at the Micro- and Nanoscale*. Oxford University Press, New York, 4 edition edition, November 2012.

[124] Pratyusha Davuluri. An Introduction to Electron Microscopy, FEI, April 2018.

Paper I

Gallium diffusion in zinc oxide via the paired dopant-vacancy mechanism
T. N. Sky, K. M. Johansen, H. N. Riise, B. G. Svensson, and L. Vines
Journal of Applied Physics 123, 055701 (2018)

JOURNAL OF APPLIED PHYSICS 123, 055701 (2018)

Gallium diffusion in zinc oxide via the paired dopant-vacancy mechanism

T. N. Sky,[a)] K. M. Johansen, H. N. Riise, B. G. Svensson, and L. Vines
Department of Physics/Center for Materials Science and Nanotechnology, University of Oslo, P.O. Box 1048, Blindern, N-0316 Oslo, Norway

(Received 14 August 2017; accepted 19 January 2018; published online 2 February 2018)

Isochronal and isothermal diffusion experiments of gallium (Ga) in zinc oxide (ZnO) have been performed in the temperature range of 900–1050 °C. The samples used consisted of a sputter-deposited and highly Ga-doped ZnO film at the surface of a single-crystal bulk material. We use a novel reaction diffusion (RD) approach to demonstrate that the diffusion behavior of Ga in ZnO is consistent with zinc vacancy (V_{Zn}) mediation via the formation and dissociation of $Ga_{Zn}V_{Zn}$ complexes. In the RD modeling, experimental diffusion data are fitted utilizing recent density-functional-theory estimates of the V_{Zn} formation energy and the binding energy of $Ga_{Zn}V_{Zn}$. From the RD modeling, a migration energy of 2.3 eV is deduced for $Ga_{Zn}V_{Zn}$, and a total/effective activation energy of 3.0 eV is obtained for the Ga diffusion. Furthermore, and for comparison, employing the so-called Fair model, a total/effective activation energy of 2.7 eV is obtained for the Ga diffusion, reasonably close to the total value extracted from the RD-modeling. *Published by AIP Publishing.*
https://doi.org/10.1063/1.5000123

I. INTRODUCTION

Transparent and semiconducting zinc oxide (ZnO) has been extensively investigated over the past decades due to its desired and potential use in optoelectronic devices. Although the notorious n-type-only behavior of ZnO has impeded this realization, highly conductive n-type ZnO films used as a transparent conductive oxide (TCO) layer have been realized via doping by aluminium (Al) or gallium (Ga).[1–3] Controlling the dopant concentration and spatial distribution is essential for a vast range of applications and relies on an understanding of the diffusion process. For Al, both early studies and more recent ones, as well as density-functional-theory (DFT), report an activation energy for the diffusion in the range 2.6–2.7 eV.[4–6] For Ga, on the other hand, early work reported a pre-exponential factor and an activation energy of 10^4 cm^2 s^{-1} and 3.75 eV,[4] respectively. More recent results indicated corresponding values of 10^{-6} cm^2 s^{-1} and 1.47 eV,[7] while first-principles calculations estimated the activation energy to be 2.45 eV for Ga.[6] Hence, a significant discrepancy exists in the literature. Moreover, it has been shown that self-compensation occurs in Al and Ga doped ZnO,[5,8] thereby limiting its conductivity and applicability as TCO. For Al doping, the self-compensation is explained by the formation of zinc vacancies (V_{Zn}) and a complex between V_{Zn} and substitutional Al at the zinc sub-lattice (Al_{Zn}).[5,9] Further, the latter complex has been shown to be the main vehicle for Al diffusion.[5] The diffusion of an impurity atom and a vacancy as a paired complex was alluded in 1969 by Hu,[10] where it was proposed that the presence of Coulombic attraction between a charged vacancy and an oppositely charged dopant may tend to keep the vacancy in the vicinity of the dopant.

In this work, we combine experimental diffusion data and DFT data in a reaction diffusion (RD) model to show that the diffusion of Ga in monocrystalline ZnO is vacancy mediated via the formation and dissociation of a $Ga_{Zn}V_{Zn}$ complex. Moreover, quantitative estimates for the defect-dopant interplay are obtained due to the kinetics characteristics of the RD model used in the simulations.

II. EXPERIMENT

A thin film of Ga-doped ZnO (2×10^{21} cm^{-3}) was deposited onto hydrothermally grown single crystalline (0001-oriented) bulk ZnO samples (Tokyo Denpa) with a bulk resistivity of 1310 Ω cm. The deposition was performed in a Semicore magnetron sputtering system using a 99.95% pure Ga-doped ZnO target ($Zn_{0.9}Ga_{0.1}O$), resulting in a 1.6 μm thick Ga-doped ZnO film. After the deposition, a laser-cut was made at the backside of the sample followed by cleavage into several small samples with a typical size of 5×5 mm^2. One sample was sequentially heat treated for 30 min from 900 °C up to 1050 °C in stages of 50 °C to realize in-diffusion of Ga into the bulk material. In addition, a series of isothermal heat treatments for durations in the range of 20 min up to 5 h were performed on three different samples at 950, 1000, or 1050 °C. A Cameca IMS7f Secondary Ion Mass Spectrometer (SIMS) equipped with an O_2 primary ion beam source was used to measure the concentration vs. depth profiles of Ga. Using a secondary ion field aperture, the circular gated region was 33 μm diameter, ensuring a detected region only at the center of the 150 μm^2 sputtered crater bottom. Absolute concentration values of Ga were obtained by measuring a Ga ion implanted reference sample, ensuring less than ±10% error in accuracy. Due to the highly Ga-doped ZnO deposited film and a dynamic range of typically 5 orders of magnitude for the SIMS analysis, the residual Ga-concentration in the as-grown ZnO was determined prior to the thin-film deposition and was found to be $\sim 2 \times 10^{15}$ cm^{-3}. For depth calibration, the sputtered crater

[a)]t.n.sky@fys.uio.no

depths were measured by a Dektak 8 stylus profilometer and a constant erosion rate was assumed.

III. RESULTS AND DISCUSSION

Figure 1 shows the Ga concentration vs depth profiles for the sample heat treated sequentially for 30 min from 900 °C to 1050 °C. The characteristic box-like diffusion profiles, below the 1.6 μm thick deposited film, are similar to those observed in Al-diffused samples[5] and increase both in concentration and depth as a function of temperature. The large difference of more than one order of magnitude between the Ga concentration in the deposited film and in the bulk, which endures during the heat treatments, implies that a semi-infinite source condition is a valid assumption. However, a simple model assuming free diffusion from the semi-infinite source, giving solutions in the form of a complementary error function, fails to predict the abrupt diffusion front in Fig. 1, cf. also a similar conclusion for Al diffusion in ZnO.[5]

A. RD-model

In order to explain the diffusion of Ga and to gain physical insight into the defect reactions involved, we will primarily consider a RD type model,[5,11–13] combined with recent DFT calculations of Ga in ZnO.[6] The model is based on Fickian diffusion and adds a non-linear reaction term; for a theoretical outline of the RD model, see Refs. 5 and 11. In accordance with the work of Staiauf *et al.*,[6] we further presume that V_{Zn}^{-2} is the only mediating defect and take the dopant-vacancy complex to be the only vehicle for dopant migration, with a reaction according to

$$V_{Zn}^{-2} + Ga_{Zn}^{+} \rightleftharpoons (Ga_{Zn}V_{Zn})^{-}, \tag{1}$$

where Ga_{Zn}^{+} is regarded as immobile.

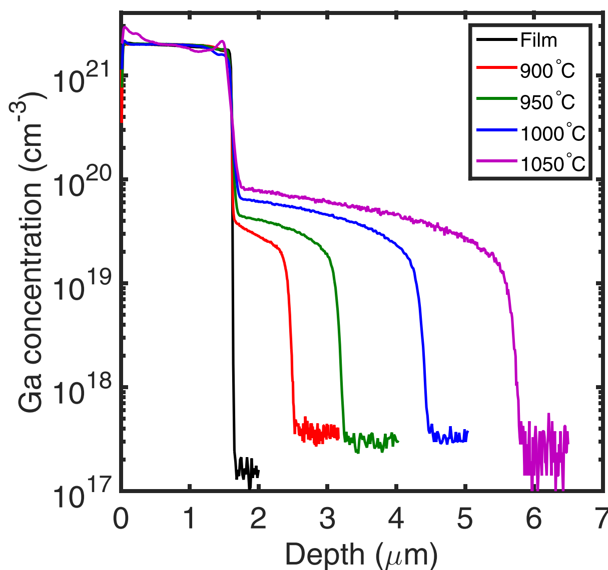

FIG. 1. Isochronal Ga diffusion profiles of the sample heat treated sequentially for 30 min from 900 °C to 1050 °C.

Here, it should also be emphasized that the deposited film of highly Ga-doped ZnO at the bulk crystal surface is considered as a source of $(Ga_{Zn}V_{Zn})^{-}$ complexes, and not of Ga_{Zn}^{+}, in our RD-modeling. That is, already formed $(Ga_{Zn}V_{Zn})^{-}$ complexes are injected into the bulk and their flux is treated as a boundary condition in the simulations. This assumption is corroborated by several theoretical and experimental results in the literature for the two analogous cases of Ga- and Al-doped ZnO.[5,8,9,14,15] Calculations based on DFT predict a significantly lower formation energy of $(Ga_{Zn}V_{Zn})^{-}$ and $(Al_{Zn}V_{Zn})^{-}$ complexes than that of isolated V_{Zn}^{-2} and Ga_{Zn}^{+} and V_{Zn}^{-2} and Al_{Zn}^{+}, respectively, in highly n-type samples under O-rich ambient conditions corresponding to those in the present experiments.[5,14,15] This prediction is supported by electron paramagnetic resonance (EPR) spectroscopy measurements revealing not only the atomic configuration of the $(Al_{Zn}V_{Zn})$ complex but also that it prevails over V_{Zn} and Al_{Zn} by several orders of magnitude in MeV electron-irradiated samples with an Al concentration in the mid 10^{17} cm^{-3} range.[9] Furthermore, employing synchrotron X-ray absorption measurements and DFT, T-Thienprasert *et al.*[15] evidenced that the $(Al_{Zn}V_{Zn})^{-}$ complex, acting as a deep compensating acceptor, is responsible for the suppressed net carrier concentration in highly Al-doped ZnO samples. Similar conclusions hold also for highly Ga-doped samples, where positron annihilation spectroscopy (PAS) studies revealed a concentration of point defects involving V_{Zn} in excess of 10^{19} cm^{-3} (this lower limit is due to saturation of the PAS signal).[8] On the basis of these arguments and to summarize, the reverse reaction in Eq. (1) is expected to be strongly suppressed in heavily Ga/Al-doped polycrystalline ZnO films, yielding a high steady-state concentration of $(Ga_{Zn}V_{Zn})^{-}$ [or $(Al_{Zn}V_{Zn})^{-}$] complexes.

B. Influence of the Fermi-level position

The abrupt front observed for all the diffusion profiles (Fig. 1) indicates that the Ga dopants induce a spatial variation of the charge carrier concentration (i.e., a Fermi level dependence). The high concentration of Ga donor dopants in the indiffused region (4×10^{19}–1×10^{20} cm^{-3}) is about 6 orders of magnitude higher than the net charge carrier concentration in the bulk (2×10^{13} cm^{-3}), where the latter is deduced from the measured resistivity of the as-received samples and assuming a bulk electron mobility of 100 cm^2/V s.

The double acceptor level of V_{Zn} is located in the lower part of the band gap,[16] and the double negative charge state is the prevailing one in n-type samples. The local concentration of V_{Zn}^{-2}, mediating the Ga diffusion in the ZnO bulk [cf. Eq. (1)], can be expressed via the local Fermi level position (ϵ_F) by

$$[V_{Zn}^{-2}] = N_{Zn} e^{-\frac{E_{f,0}(V_{Zn}^{-2}) - 2\epsilon_F}{k_B T}}, \tag{2}$$

where N_{Zn} is the total number of Zn sites per unit volume, $E_{f,0}(V_{Zn}^{-2})$ is the formation energy of V_{Zn}^{-2} at the valence band edge (i.e., when $\epsilon_F = 0$), k_B is the Boltzmann constant, and T is the absolute temperature. This means that the formation of V_{Zn}^{-2} is regarded as an instantaneous process with a local

equilibrium concentration governed by Eq. (2). Hence, ϵ_F has a decisive impact on the RD-modelling results. For the simulated curves, a fixed value of $E_{f,0}(V_{Zn}^{-2}) = 7.4\,eV$ is used, resulting in an adequate fit with the experimental data. This is also in reasonable agreement with previous DFT-predictions of $E_{f,0}(V_{Zn}^{-2})$ under O-rich conditions.[14,17] Moreover, a binding energy $E_b(Ga_{Zn}V_{Zn})^- = 1.25\,eV$ for the complex, as previously predicted by DFT-calculations,[6] is used as a fixed parameter in the RD-simulations.

C. Comparison between experimental and RD modelling results

Figure 2 shows the RD model fitted to the experimental isochronal diffusion profiles. The diffusion simulations adequately reproduce the experimental diffusion profiles and an activation energy of $E_{a,complex} = 2.3 \pm 0.1\,eV$ with a pre-exponential factor of $D_0 = 8^{+15}_{-5} \times 10^{-2}\,cm^2\,s^{-1}$ is extracted for the diffusion of $Ga_{Zn}V_{Zn}$ (Fig. 3). In the simulations (Fig. 2), the error of the fitted diffusivity values is comparable to the marker size (~3%), as determined by monitoring the agreement between the experimental and the fitted profiles when varying the diffusivity parameter.

Since the extracted $E_{a,complex}$-value represents the activation energy for diffusion of an already formed complex, i.e., the migration energy $E_m = E_{a,complex} = 2.3\,eV$, it enables a direct comparison with theoretical estimates. Here, it must be noted that the obtained migration energy E_m for $Ga_{Zn}V_{Zn}$ is not unique as it depends on the presumed values of $E_{f,0}(V_{Zn}^{-2})$ and $E_b(Ga_{Zn}V_{Zn})^-$ in the RD-simulations. However, using the DFT value of $E_b(Ga_{Zn}V_{Zn})^- = 1.25\,eV$ reported by Steiauf *et al.*,[6] our results are in excellent agreement with their theoretically predicted migration barrier of 2.23 eV (Ref. 6) for $Ga_{Zn}V_{Zn}$.

Figure 3 shows the present diffusivity values together with previously reported experimental data by Norman[4] and

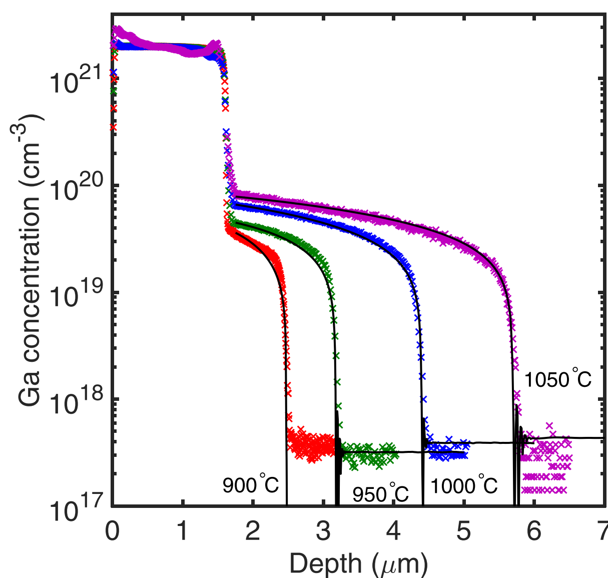

FIG. 2. RD model (solid lines) fitted to the experimental isochronal Ga diffusion profiles of the sample heat treated sequentially for 30 min from 900 °C to 1050 °C. The numerical accuracy of the fitted diffusivity values is better than 3%.

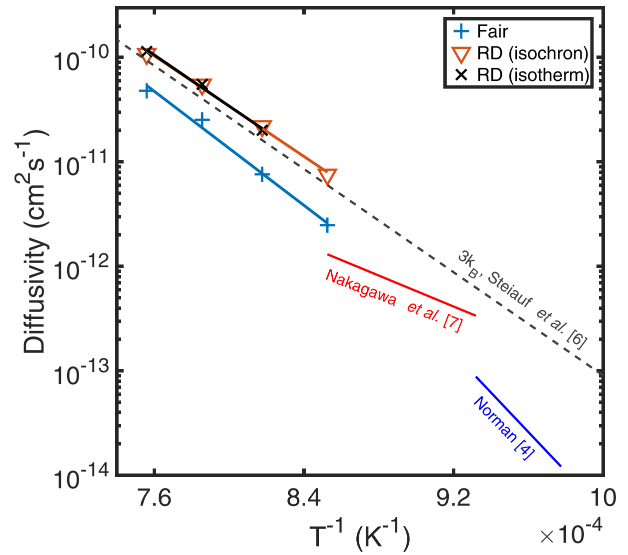

FIG. 3. Diffusivities of Ga and $Ga_{Zn}V_{Zn}$ (RD) in ZnO. For the calculated values from Steiauf *et al.*[6] ($E_a^{[Steiauf]} = 2.45\,eV$), the entropy contribution is set to $3k_B$, corresponding to a prefactor of $2 \times 10^{-1} cm^2\,s^{-1}$.

Nakagawa *et al.*[7] Theoretical data from first-principles calculations for the total activation energy[6] are also included for comparison. Note that D_0 is merely a structural entity,[18] $D_0^{ZnO[0001]} = (3/4) f c^2 \Gamma_0 e^{S/k_B}$, where $f \leq 1$ is a correlation factor, c is the jump distance equal to 3.25 Å in ZnO, $\Gamma_0 \approx 10^{13}\,s^{-1}$ being the typical phonon frequency, and S the entropy contribution. For $S = 0$ and $f = 1$, this results in $D_0 \approx 10^{-2}\,cm^2\,s^{-1}$, which is rather close to the value extracted from the RD modeling and suggests a jump process with a small entropy effect. The obtained diffusion parameters are listed in Table I, together with previously reported values by other authors. A solubility of the $Ga_{Zn}V_{Zn}$ complex is found to be $S_{Ga_{Zn}V_{Zn}} = 1 \times 10^{23} \exp(-1.1\,eV/k_B T)\,cm^{-3}$, which is about one order of magnitude lower than the measured chemical concentration of Ga.

Further, isothermal diffusion experiments were performed in order to reveal any transient processes. Figure 4 shows the experimental isothermal Ga diffusion profiles of three samples heat treated at 950, 1000, or 1050 °C, respectively, for durations in the range of 20 min to 5 h. Simulation

TABLE I. Extracted diffusion parameters for Ga in ZnO, together with previous theoretical and experimental results. With D_0 being the pre-exponential factor, E_m is the migration barrier for the exchange process of $Ga_{Zn}V_{Zn}$ and E_a is the total activation energy for diffusion.

	D_0 (cm²/s)	E_m (eV)	E_a (eV)
Fair	1	…	2.7 ± 0.1
RD (isochron)	8×10^{-2}	2.3 ± 0.1	3.0[d] ± 0.2
Theo[a]	…	2.23	2.45
Exp[b]	2.7×10^{-6}	…	1.47
Exp[c]	3.6×10^{4}	…	3.75

[a] Steiauf *et al.*[6]
[b] Nakagawa *et al.*[7]
[c] Norman.[4]
[d] Obtained from Eq. (5).

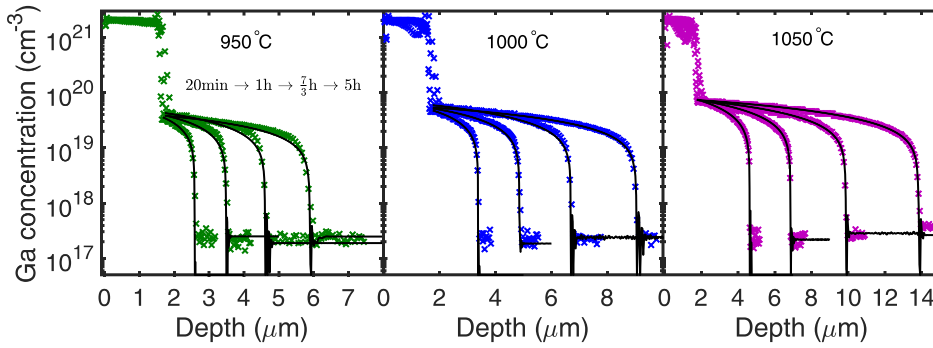

FIG. 4. Isothermal Ga diffusion profiles of the three samples heat treated sequentially for durations in the range of 20 min to 5 h at 950 °C, 1000 °C, or 1050 °C. The solid lines are the simulation results from our RD modeling. The numerical accuracy of the fitted diffusivity values is better than 3%.

results obtained from the RD model are also included in Fig. 4, and they follow closely the experimental data. A square-root of time dependence holds for the isothermal diffusion profiles, which supports the assumption that local equilibrium of the reaction in Eq. (1) is rapidly established. A migration barrier of $E_m = 2.3$ eV with a pre-exponential factor of 1×10^{-1} cm^2 s^{-1} is obtained from the isothermal data, substantiating the validity of the results deduced from the isochronal experiment in Fig. 2. The corresponding diffusivities, where each value is taken as the mean of the set of measurements at different times, are displayed in Fig. 3. In this regard, we note that the slightly abnormal shape of the 900 °C isochronal experiment (Figs. 1 and 2) may be due to initial transient effects at this low temperature before steady state is fully established. However, based on the consistent trend of the Arrhenius behavior of the extracted diffusivities (Fig. 3), we consider the 900 °C experiment to primarily reflect a similar diffusion behavior as that at the higher temperatures.

In addition to provide a value for the $Ga_{Zn}V_{Zn}$ migration barrier, the RD model has also been applied to estimate the total activation energy for the Ga diffusion, E_a. As schematically illustrated in Fig. 5, to move Ga_{Zn} via V_{Zn}, it requires the formation and presence of a V_{Zn} as a next-nearest neighbour. That is, V_{Zn} must form at some site and subsequently approach the Ga_{Zn}. The associated V_{Zn} must then either (i) exchange with Ga_{Zn} and dissociate or (ii) exchange and rotate around the Ga_{Zn}. In a first approximation, the total activation energy for the diffusion of Ga can be expressed as a sum of all the above processes

$$E_a = E_f(V_{Zn}^{-2}) + E_m(V_{Zn}^{-2}) + E_m(Ga_{Zn}V_{Zn})^- \\ -E_d(Ga_{Zn}V_{Zn})^-, \quad (3)$$

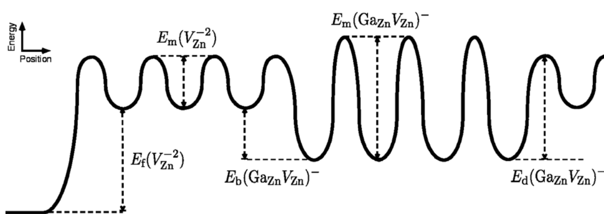

FIG. 5. Energy diagram illustrating the involved processes for the diffusion of Ga. From left: the formation of V_{Zn}^{-2}, the migration of V_{Zn}^{-2}, the binding of V_{Zn}^{-2} with Ga_{Zn}^+, the migration of $(Ga_{Zn}V_{Zn})^-$, and the dissociation of the complex.

where $E_f(V_{Zn}^{-2})$ is the formation energy of V_{Zn}^{-2}, $E_m(V_{Zn}^{-2})$ and $E_m(Ga_{Zn}V_{Zn})^-$ are the migration barrier for V_{Zn}^{-2} and the barrier for the migration of $(Ga_{Zn}V_{Zn})^-$, respectively, while $E_d(Ga_{Zn}V_{Zn})^-$ is the energy required to dissociate the complex. The dissociation barrier can in turn be approximated as

$$E_d(Ga_{Zn}V_{Zn})^- = E_b(Ga_{Zn}V_{Zn})^- + E_m(V_{Zn}^{-2}) - k_BT, \quad (4)$$

where $E_b(Ga_{Zn}V_{Zn})^-$ is the binding energy of the complex. In the modeling, we use an effective capture radius of $R_c = 1$ nm for the trapping of V_{Zn}^{-2} by Ga_{Zn}^+, leading to the inclusion of k_{BT} in Eq. (4). This term arises due to the slightly reduced (by the amount of k_BT) potential energy of the dissociated V_{Zn}^{-2} at a distance R_c from Ga^+ (see Ref. 19 for a general formalism). Inserting Eq. (4) into Eq. (3) gives

$$E_a = E_f(V_{Zn}^{-2}) - E_b(Ga_{Zn}V_{Zn})^- + E_m(Ga_{Zn}V_{Zn})^- + k_BT. \quad (5)$$

Here, $E_f(V_{Zn}^{-2})$ is extracted from $E_{f,0}(V_{Zn}^{-2})$ and the Fermi level position at the interface between the diffusion source and the bulk crystal ($E_f(V_{Zn}^{-2}) = E_{f,0}(V_{Zn}^{-2}) - 2\epsilon_F$) is found to be 1.85 eV. With $k_BT = 0.1$ eV, we obtain a total activation energy of $E_a = 3.0$ eV for the diffusion of Ga in ZnO. Interestingly, the difference in E_a between our data and the theoretical ones in Ref. 6 can be attributed to a difference in $E_{f,0}(V_{Zn}^{-2})$ used in the calculations of $E_f(V_{Zn}^{-2})$. Furthermore, we obtain an upper limit for $E_d(Ga_{Zn}V_{Zn})^-$ of 3.05 eV, whereupon the model begins to deviate from the experimental data. Hence, in accord with Eq. (4), $E_m(V_{Zn}^{-2})$ cannot exceed 3.05 – 1.25 + 0.1 = 1.9 eV and $E_m(Ga_{Zn}V_{Zn})^-$ is the limiting migration barrier for the diffusion of Ga at these conditions (as schematically illustrated in Fig. 5). This conclusion is also fully supported by the quadratic Ga-concentration dependence of the Ga diffusivity, in accordance with several general and comprehensive studies of the concentration dependence of dopant diffusion in semiconductors.[11–13] In particular, it becomes evident that V_{Zn}^{-2} cannot be the defect controlling/limiting the migration process as this results in Ga diffusion profiles of very different shape than the experimental ones.[11]

D. Comparison between experimental and Fair modelling results

In order to further substantiate the results obtained from our RD model, we also analyse the experimental data using

another and more common approach to model dopant diffusion in semiconductors. The approach assumes each dopant to be in its isolated configuration, which is a valid approximation given that only a small fraction of the dopants exist in defect complexes. If one further accounts for the electric field arising from the non-uniform dopant distribution, giving rise to energy band bending, the dopant diffusion is described as a sum of the different charge state contributions.[20] In other words, the effective diffusion coefficient can be regarded as concentration dependent.[11] This is often denoted as the Fair model.[21] Considering only a double negatively charged defect X mediating the diffusion, the effective Ga diffusivity becomes

$$D_{\mathrm{Ga}} = HD^{i}_{\mathrm{Ga}^{+}X^{-2}}\left(\frac{n}{n_i}\right)^2. \quad (6)$$

In Eq. (6), H is a correction factor arising from the spatially varying Fermi level, taking values between 1 (intrinsic regime) and 2 (far-extrinsic regime). The superscript i denotes intrinsic conditions. n is the free carrier concentration, and $n_i = \sqrt{N_C N_V}\exp\left(-\frac{E_g}{2k_BT}\right)$ is the intrinsic carrier concentration with N_C and N_V being the effective density of states at the conduction- and valence band edge, respectively. The $(n/n_i)^2$ term is proportional to the number of double negatively charged defects and reflects the probability-of-existence of, e.g., V_{Zn}^{-2}. The ZnO band gap E_g equals 3.4 eV at room temperature but is significantly reduced at the diffusion temperatures employed. We have used data from band gap measurements of ZnO in the temperature range of 100–500 °C by Hauschild *et al.*[22] and then assumed a similar linear dependence at higher temperatures: $\Delta E_g(T) = 80.5 - 0.52\,T$ (meV).

As can be seen in Fig. 6, Fair's model [Eq. (6)] adequately reproduces the experimental data recorded after 30 min at 1000 °C (isochronal annealing) but gives a slightly higher concentration close to the diffusion tail as compared to that of the RD model. An activation energy of $E_a = 2.7$ eV with a pre-exponential factor of $D_0 = 1\,\mathrm{cm^2\,s^{-1}}$ is obtained for D_{Ga} (see Fig. 3), where complete ionization of Ga_{Zn} is assumed (i.e., n is taken to be given by the solid solubility of Ga, $n = S_{Ga} = 7\times10^{22}\exp(-0.8\,\mathrm{eV}/k_BT)\,\mathrm{cm^{-3}}$). D_{Ga} extracted from Eq. (6) is an effective (or apparent) diffusion coefficient given by the product of the equilibrium concentration and the diffusivity of $(Ga_{Zn}V_{Zn})^-$ divided by the concentration of Ga_{Zn}^+.[11,20] Hence, the E_a value of 2.7 eV does not only contain the activation energy for migration of $(Ga_{Zn}V_{Zn})^-$ but also the difference between the formation energies of $(Ga_{Zn}V_{Zn})^-$ and Ga_{Zn}^+. Thus, a direct comparison with the results from the RD-modeling and $E_m(Ga_{Zn}V_{Zn})^-$ is not valid. However, if $E_m(Ga_{Zn}V_{Zn})^-$ is assumed to be 2.3 eV, as extracted from the RD-modeling and in close agreement with the DFT predication by Steiauf *et al.*,[6] one obtains $E_f(Ga_{Zn}V_{Zn})^- - E_f(Ga_{Zn}^+) \approx 0.4$ eV at the temperatures of diffusion. Indeed, such a relatively small difference between $E_f(Ga_{Zn}V_{Zn})^-$ and $E_f(Ga_{Zn}^+)$ is fully consistent with the DFT results by Demchenko *et al.*[14] under O-rich conditions, accounting for the E_g narrowing with temperature and that extrinsic conditions still prevail in the highly Ga-doped ZnO films during diffusion, i.e., ϵ_F remains close to the conduction band edge. Moreover and despite some uncertainty, it is interesting to note that the total (or effective) value of 3.0 ± 0.2 eV for the Ga diffusion extracted from the RD-modeling[Eq. (5) and Table I] is in fair/reasonable agreement with the effective value of 2.7 ± 0.1 eV from the Fair modeling. The discrepancy between the two values (3.0 versus 2.7 eV) is essentially within the accuracy of data analysis of the two approaches, especially considering the limited accuracy of DFT estimates and the high concentration of $(Ga_{Zn}V_{Zn})^-$ complexes. The latter may also partly violate the implicit assumption regarding a much lower concentration of $(Ga_{Zn}V_{Zn})^-$ complexes than that of Ga_{Zn}^+ donors made in the Fair modeling.

As previously discussed, the donor dopant concentration is about 6 orders of magnitude higher in the indiffused region compared to that of the bulk. In addition, as demonstrated in Fig. 6 by the comparison between the RD-type model [Eq. (1)] and the Fair model [Eq. (6)], a quadratic dependence between the Ga diffusivity and the Ga concentration adequately explains the experimental Ga diffusion profile. Hence, the modelling results provide strong support for a V_{Zn}^{-2}-mediated diffusion of Ga with an exponential dependence on the Fermi-level position (ϵ_F). However, for an unambiguous conclusion on the diffusion mechanism and especially the ϵ_F dependence, isoconcentration diffusion experiments with ϵ_F pinned at given positions are desirable. Indeed, using undoped and *in situ* doped isotopic heterostructure ZnO samples, Azarov *et al.*[23] have recently shown experimentally that the Zn self-diffusion is enhanced by several orders of magnitude as ϵ_F is shifted towards the conduction band edge. Accordingly, V_{Zn}^{-2} was regarded as the mediating defect of the Zn self-diffusion and an upper limit of 1.5 eV was determined for $E_m(V_{Zn}^{-2})$, fully consistent with our modelling results. Moreover, preliminary PAS and SIMS

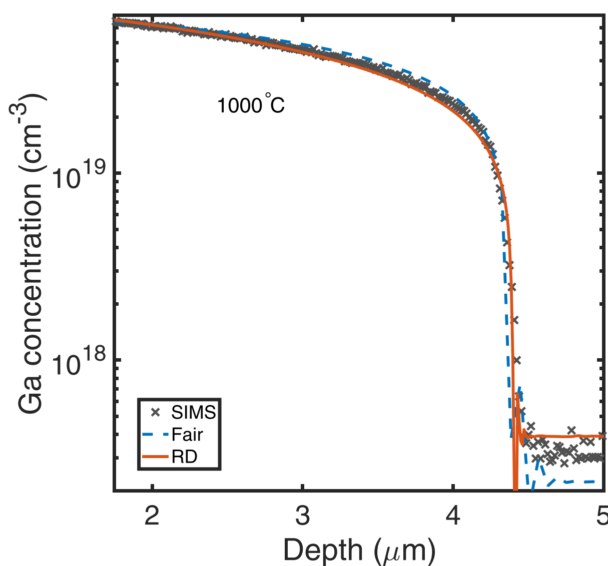

FIG. 6. Comparison of the Fair model and the reaction diffusion (RD) model, as fitted to the experimentally obtained SIMS profile after the 1000 °C (isochronal) treatment. Note that the data from the deposited film have been excluded for clarity.

data for Al-doped ZnO samples reveal a quadratic relation between the V_{Zn} and Al concentrations,[24] corroborating V_{Zn}^{-2} as a prime defect promoting Al diffusion. A similar result is also anticipated for Ga-doped ZnO samples and further studies on this subject are being pursued.

IV. SUMMARY

The diffusion of Ga in monocrystalline ZnO is found to be well described as vacancy mediated through the formation (and subsequent dissociation) of an intermediate dopant-vacancy complex. Both simulation results from our RD model and from Fair's model suggest that the diffusion of Ga proceeds by one single mechanism throughout the studied temperature interval, 900–1050 °C. From the RD-simulations, this mechanism is suggested to be driven by V_{Zn}^{-2} through the diffusion of $(Ga_{Zn}V_{Zn})^{-}$. Utilizing DFT estimates of $E_f(V_{Zn}^{-2})$ and $E_b(Ga_{Zn}V_{Zn})^{-}$, a migration barrier of $E_m = 2.3$ eV with a pre-exponential factor of 8×10^{-2} cm^2 s^{-1} is deduced for the $(Ga_{Zn}V_{Zn})^{-}$ complex from the RD-modeling, in close agreement with results from recent first principles calculations.[6] The Fair modeling gives a total/effective energy of 2.7 ± 0.1 eV for Ga diffusion in ZnO which is in reasonable agreement with the total/effective value of 3.0 ± 0.2 eV obtained from the RD-modeling. Previous experimental values in the literature for the total/effective activation energy of Ga diffusion in ZnO scatter over a range of more than 2 eV (Refs. 4 and 7) and our value is approximately in the middle of this range.

ACKNOWLEDGMENTS

Financial support from the Research Council of Norway for funding of the DYNAZOx-project (Grant No. 221992), Salient (Grant No. 239895), the University of Oslo, and the Norwegian Micro- and Nano-Fabrication Facility (NorFab 245963) is gratefully acknowledged.

[1]T. Minami, H. Sato, H. Nanto, and S. Takata, Jpn. J. Appl. Phys., Part 2 **24**, L781 (1985), ISSN 1347-4065.
[2]H. Y. Liu, V. Avrutin, N. Izyumskaya, M. A. Reshchikov, Ü. Özgür, and H. Morkoç, Phys. Status Solidi RRL **4**, 70 (2010), ISSN 1862-6270.
[3]J. Nomoto, M. Konagai, K. Okada, T. Ito, T. Miyata, and T. Minami, Thin Solid Films **518**, 2937 (2010), ISSN 0040-6090.
[4]V. Norman, Aust. J. Chem. **22**, 325 (1969).
[5]K. M. Johansen, L. Vines, T. S. Bjørheim, R. Schifano, and B. G. Svensson, Phys. Rev. Appl. **3**, 024003 (2015).
[6]D. Steiauf, J. L. Lyons, A. Janotti, and C. G V d. Walle, APL Mater. **2**, 096101 (2014), ISSN 2166-532X.
[7]T. Nakagawa, I. Sakaguchi, M. Uematsu, Y. Sato, N. Ohashi, H. Haneda, and Y. Ikuhara, Jpn. J. Appl. Phys., Part 1 **46**, 4099 (2007), ISSN 1347-4065.
[8]D. C. Look, K. D. Leedy, L. Vines, B. G. Svensson, A. Zubiaga, F. Tuomisto, D. R. Doutt, and L. J. Brillson, Phys. Rev. B **84**, 115202 (2011).
[9]J. E. Stehr, K. M. Johansen, T. S. Bjørheim, L. Vines, B. G. Svensson, W. M. Chen, and I. A. Buyanova, Phys. Rev. Appl. **2**, 021001 (2014).
[10]S. M. Hu, Phys. Rev. **180**, 773 (1969).
[11]H. Bracht, Phys. Rev. B **75**, 035210 (2007).
[12]M. Uematsu, J. Appl. Phys. **82**, 2228 (1997), ISSN 0021-8979, 1089-7550.
[13]U. M. Gosele, Annu. Rev. Mater. Sci. **18**, 257 (1988).
[14]D. O. Demchenko, B. Earles, H. Y. Liu, V. Avrutin, N. Izyumskaya, Ü. Özgür, and H. Morkoç, Phys. Rev. B **84**, 075201 (2011).
[15]J. T-Thienprasert, S. Rujirawat, W. Klysubun, J. N. Duenow, T. J. Coutts, S. B. Zhang, D. C. Look, and S. Limpijumnong, Phys. Rev. Lett. **110**, 055502 (2013).
[16]A. Janotti and C. G. Van de Walle, Phys. Rev. B **76**, 165202 (2007).
[17]Y. K. Frodason, K. M. Johansen, T. S. Bjørheim, B. G. Svensson, and A. Alkauskas, Phys. Rev. B **95**, 094105 (2017).
[18]J. Philibert, *Atom Movements – Diffusion and Mass Transport in Solids* (Les Editions De Physique, 1991).
[19]M. Janson, Ph.D. thesis, KTH, Royal Institute of Technology, 2003.
[20]P. M. Fahey, P. B. Griffin, and J. D. Plummer, Rev. Mod. Phys. **61**, 289 (1989).
[21]R. B. Fair and J. C. C. Tsai, J. Electrochem. Soc. **124**, 1107 (1977), ISSN 0013-4651, 1945-7111.
[22]R. Hauschild, H. Priller, M. Decker, J. Brückner, H. Kalt, and C. Klingshirn, Phys. Status Solidi C **3**, 976 (2006), ISSN 1610-1642.
[23]A. Azarov, V. Venkatachalapathy, Z. Mei, L. Liu, X. Du, A. Galeckas, E. Monakhov, B. G. Svensson, and A. Kuznetsov, Phys. Rev. B **94**, 195208 (2016).
[24]T. N. Sky, K. M. Johansen, F. Tuomisto, B. G. Svensson, and L. Vines, "Influence of Fermi-level position on vacancy-assisted diffusion of aluminum in zinc oxide" (unpublished).

Paper II

Influence of Fermi-level position on Vacancy-Assisted Diffusion of Aluminum in Zinc Oxide
T. N. Sky, K. M. Johansen, V. Venkatachalapathy, B. G. Svensson, F. Tuomisto and L. Vines
PHYSICAL REVIEW B 98, 245204 (2018)

Influence of Fermi level position on vacancy-assisted diffusion of aluminum in zinc oxide

T. N. Sky,* K. M. Johansen, V. Venkatachalapathy, B. G. Svensson, and L. Vines
Department of Physics and Center for Materials Science and Nanotechnology, University of Oslo, P.O. Box 1048 Blindern, N-0316 Oslo, Norway

F. Tuomisto
Department of Applied Physics, Aalto University, P.O. Box 15100, FI-00076 Aalto, Espoo, Finland

(Received 23 March 2018; revised manuscript received 4 December 2018; published 28 December 2018)

The influence of Fermi level position and annealing ambient on the zinc vacancy V_{Zn} generation and Al diffusion is studied in monocrystalline zinc oxide (ZnO). From secondary-ion mass spectrometry and positron annihilation spectroscopy results, a quadratic dependence between the concentrations of V_{Zn} and Al is established, demonstrating the Fermi level dependence of the formation of the electrically compensating -2 charge state of V_{Zn} in conductive n-type ZnO crystals. In contrast, thermal treatment in the zinc-rich ambient is shown to efficiently reduce the V_{Zn} concentration and related complexes. Using a reaction-diffusion model, the diffusion characteristics of Al at different donor background concentrations are fully accounted for by mobile $(Al_{Zn}V_{Zn})^-$ pairs. These pairs form via the migration and reaction of isolated V_{Zn}^{2-} with the essentially immobile Al_{Zn}^+. We obtain a migration barrier for the $(Al_{Zn}V_{Zn})^-$ pair of 2.4 ± 0.2 eV, in good agreement with theoretical predictions. In addition to strongly alter the shape of the Al diffusion profiles, increasing the donor background concentration also results in an enhanced effective Al diffusivity, attributed to a reduction in the V_{Zn}^{2-} formation energy as the Fermi level position increases.

DOI: 10.1103/PhysRevB.98.245204

I. INTRODUCTION

Vacancy-assisted impurity diffusion in semiconductors plays a central role in both device processing and fundamental understanding of the defect interplay. This is particularly true for semiconducting oxides like zinc oxide (ZnO) [1–8], where highly conductive n-type crystals (n-ZnO) can be realized by doping with, e.g., Al or Ga [9] and can be used in optoelectronics and photovoltaics. It is known, however, that self-compensation effects arise in highly doped ZnO [10], which pose a limit to the conductivity, although the exact mechanism remains somewhat controversial. For Al-containing ZnO, this has been attributed to the formation of zinc vacancies V_{Zn} and/or a complex between V_{Zn} and Al at the zinc site $(Al_{Zn}V_{Zn})$ [11].

Regardless of the crystal growth technique used, ZnO is notoriously known to exhibit n-type conductivity. Intrinsic defects such as oxygen vacancies V_O have long been speculated to be the origin of the unintentional n-type behavior [12]. However, more recent results conclude that V_O is a deep double donor [13,14], not contributing to the free-carrier concentration at room temperature. Also Zn_i can be ruled out as the source of the n-type conductivity due to its high formation energy in n-ZnO and low migration barrier of 0.55–0.70 eV [15,16], ensuring migration even at room temperature. The focus has therefore shifted to residual impurities that may affect the electrical properties. Common residual impurities in hydrothermally grown ZnO are hydrogen ($<5 \times 10^{17}$ cm^{-3}), lithium ($\sim 10^{17}$ cm^{-3}), silicon ($\sim 10^{16}$ cm^{-3}), and aluminum (3×10^{15} cm^{-3}) [17]. H, Si, and Al may all increase the n-type conductivity acting as shallow donors [17], while Li has been shown to primarily reside on the zinc site acting as an acceptor in n-ZnO [18,19].

V_{Zn} is considered to be a deep acceptor in n-ZnO, with theoretical studies predicting the V_{Zn} to be in the double negatively charged state (V_{Zn}^{2-}) [13,14,20–22]. This double-acceptor behavior has also been indicated experimentally by comparing positron annihilation spectroscopy results with Hall effect data [10,23,24]. Furthermore, recent diffusion studies of Al [4] and Ga [25] in ZnO have demonstrated a quadratic dependence of the apparent diffusion coefficient on the concentration of Al or Ga. In Refs. [4,25], it was further suggested that V_{Zn}^{2-} is the dominant vehicle for the diffusion of Al/Ga through the formation of an intermittent substitutional dopant-vacancy complex.

Moreover, calculations based on density functional theory (DFT) predict the formation energy of V_{Zn} to be highly dependent not only on the Fermi level position but also on the chemical potential or annealing ambient [14]. Hence, this can be utilized to control dopant diffusion in oxides [14]. Indeed, the boiling point of zinc is sufficiently low to obtain a Zn-rich ambient during typical diffusion processes, and accordingly, ZnO is one of the few systems where metal-rich conditions can apply in practice. Thus, ZnO is an attractive model system to study the influence of the Fermi level position and ambient on impurity diffusion via charged vacancies.

In this work, we first use positron annihilation spectroscopy (PAS) and secondary-ion mass spectrometry (SIMS)

*t.n.sky@fys.uio.no

2469-9950/2018/98(24)/245204(8) ©2018 American Physical Society

to directly observe a quadratic dependence between the V_{Zn}– and Al dopant concentrations in n-ZnO and hence the Fermi level dependence of the V_{Zn}^{2-} formation energy. Second, quasi-isoconcentration diffusion experiments have been performed in which the diffusion of Al occurs in monocrystalline ZnO containing a uniform background concentration of Ga. This enables control of the Fermi level position independently of the diffusing dopant under study. As a result, the diffusion of Al in ZnO is strongly evidenced to be mediated by V_{Zn}^{2-}, and it is suggested that this occurs through the formation of mobile and intermittent $(Al_{Zn}V_{Zn})^-$ pairs.

II. EXPERIMENT

A thin film of Al-doped ZnO with a thickness of 1.5 μm was deposited by sputtering onto different hydrothermally (HT) grown single-crystalline bulk ZnO (0001-oriented) wafers. A Semicore magnetron sputtering system was used to cosputter a 99.99% pure ZnO target with a 99.95% pure Al target to obtain a high-quality ZnO film containing 2×10^{21} cm^{-3} Al, as determined by SIMS. After deposition, one wafer (Tokyo Denpa) with a resistivity of 1310 Ω cm and measured residual bulk Al, Ga, H, Li, and Si concentrations of 3×10^{15}, 2×10^{15}, $< 5 \times 10^{17}$, 2×10^{17}, and $\leqslant 10^{16}$ cm^{-3}, respectively, was cleaved by a laser cutter into samples with a typical size of 5×5 mm^2. The samples were then heat treated for a duration of 80 h at 1050 °C (Al-1050) or for 3 h at 1200 °C (Al-1200) in air before the deposited films were removed by chemical etching in a HCl solution followed by mechanical polishing and a HF dip. In addition, one Al-1050 sample was subsequently heat treated in a zinc ambient at 900 °C (AlZn-900) for a duration of 2 h. For reference, one as-grown HT (Tokyo Denpa) bulk sample was treated for 3 h at 1200 °C in air (AsG-1200), while another HT (SPC GoodWill) bulk sample was treated for 2 h at 900 °C in a zinc ambient (Zn-900).

Another HT bulk wafer was obtained from the authors of Ref. [26] and grown by a modified HT method [26] to yield wafers with an as-grown uniform Ga concentration of 1×10^{19} cm^{-3} and a resistivity of 7×10^{-3} Ω cm. This wafer, labeled predoped, was subjected to a similar (but shorter) Al-doped ZnO film deposition as described above for the Tokyo Denpa wafer to yield a 0.8-μm-thick film. This was followed by sequential (isochronal) heat treatments for 30 min from 700 °C up to 1150 °C in intervals of 50 °C. It should be noted that the slightly different HT growth technique used for the predoped sample results in a lower residual Li concentration ($< 1 \times 10^{15}$ cm^{-3}) compared to 2×10^{17} cm^{-3} for the Tokyo Denpa wafer. Table I outlines the detailed workflow of the different samples used.

Doppler broadening PAS was used to estimate the concentration and depth distribution of V_{Zn} and V_{Zn}-related complexes, where monoenergetic positrons (energy varied between 0.5 and 36 keV) were implanted into the bulk surface (0001 oriented) at room temperature. The Doppler broadened annihilation peak was measured with a HPGe detector (FWHM of energy resolution of 1.2 at 511 keV) and analyzed by the conventional S and W parameters. Here, S is defined as the fraction of the counts in the central region (corresponding to electron-positron momentum of <0.4 a.u.) of the annihilation line to the total number of counts in the spectrum [27]. Similarly, W represents the fraction of the counts in the wing region (corresponding to electron-positron momentum >1.6–2.0 a.u.) [27].

TABLE I. Detailed overview of the experimental sample sequential treatments.

Sample	Film	Anneal	Polished	Anneal
Al-1050	Al:ZnO	80 h, 1050 °C	yes	
Al-1200	Al:ZnO	3 h, 1200 °C	yes	
AlZn-900	Al:ZnO	80 h, 1050 °C	yes	2 h, 900 °C
AsG-1200		3 h, 1200 °C		
Zn-900		2 h, 900°C		
Predoped	Al:ZnO	$\frac{1}{2}$ h, 700 °C → 1150°C		

To monitor the depth redistributions of Al and Ga, a Cameca IMS 7f SIMS instrument equipped with an O_2 primary ion beam source was used. Absolute concentrations were obtained by measuring separate Al- and Ga-implanted reference samples, ensuring less than ±10% error in accuracy. A Dektak 8 stylus profilometer was used to measure the sputtered crater depths, and a constant erosion rate as a function of time was assumed.

III. RESULTS AND DISCUSSION

A. Formation of V_{Zn}

Figure 1 shows the Al concentration vs depth profiles for the samples heat treated at 1050 °C (Al-1050) and 1200 °C (Al-1200) for 80 and 3 h, respectively. Also shown are the Al profiles in the reference samples AsG-1200 and Zn-900. The Al concentration is almost uniform at a level of $\sim 2 \times 10^{19}$

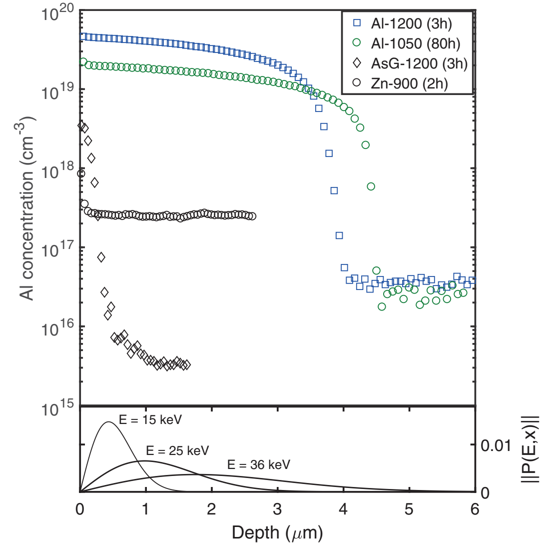

FIG. 1. Al concentration vs depth profiles of the intentionally doped samples Al-1050 and Al-1200 and of the reference samples AsG-1200 and Zn-900, as measured by SIMS. Also shown (solid lines in the bottom panel) are the calculated positron implantation profiles $P(x, E)$ for a representative range of implantation energies E.

and $\sim 4 \times 10^{19}$ cm^{-3} in the first 4–5 μm for samples Al-1050 and Al-1200, respectively. For AsG-1200 and Zn-900, the Al concentration is several orders of magnitude lower. Note that the Zn-900 sample originates from a different supplier (SPC GoodWill) than AsG-1200 and exhibits a higher as-grown residual Al concentration ($\sim 2 \times 10^{17}$ cm^{-3}).

In the event of monoenergetic positrons impinging onto a solid surface, the resulting implanted positron distribution can be expressed by a Makhov profile [28–30]. A representative selection of the Makhov profiles is included in the bottom panel of Fig. 1 (solid lines), illustrating the probing depth of the implanted positrons in a Doppler broadening measurement. The results of the Doppler broadening PAS measurements, as given by the S parameter vs positron implantation energy, are shown in Fig. 2 for the different samples presented in Fig. 1, together with that for the AlZn-900 sample. In addition, the results for a vapor phase bulk ZnO sample (ZnO lattice) are included, referencing the V_{Zn}-lean extremity (cf. [23]). The signal originating from the first $\sim$300 nm below the surface is affected by surface annihilations and, in particular, recombination with defects induced from mechanical polishing [31]. For that reason, only data points corresponding to $15 \leqslant E \leqslant 36$ keV will be discussed below. The inset in Fig. 2 shows the corresponding S-W plot, where all the data follow the same line connecting the vacancy-lean (ZnO lattice) and V_{Zn}-saturated cases. This indicates that V_{Zn} or complexes with a similar open volume are the dominating defect in samples Al-1050, Al-1200, and AsG-1200. A high S-parameter value is found for the intentionally Al doped samples, indicating an increased concentration of V_{Zn} and/or V_{Zn}-related complexes. Interestingly, V_{Zn} disappears below the detection limit ($<10^{15}$ cm^{-3}) in the Al-doped sample after subsequent treatments in Zn-rich ambient at 900 °C for 2 h (AlZn-900). This demonstrates introduction of Zn interstitials and recombination with V_{Zn} during the Zn-rich treatment and hence an increased formation energy of V_{Zn} under Zn-rich conditions, as proposed by DFT results [14]. Thus, thermal treatments in a Zn-rich ambient appear to be a viable route for reducing the concentration of V_{Zn} and related complexes. Here, it should be underlined that the presence of Al_{Zn} as 1 of the 12 next-nearest neighbors to V_{Zn} [11] is not resolved by the PAS measurement [32]. Hence, it is not possible to discern an isolated V_{Zn} from a $Al_{Zn}V_{Zn}$ pair using the PAS results.

Sample Al-1200, which exhibits the highest Al concentration (Fig. 1), also reveals the highest relative concentration of V_{Zn} (Fig. 2). This is in agreement with first-principles calculations [13,14,20–22] predicting a decrease in the V_{Zn}^{2-} and V_{Zn}^{-} formation energy as the Fermi level position increases. From the PAS results (Fig. 2), the V_{Zn} concentration can be estimated using [27]

$$C_{V_{Zn}} = \frac{\rho}{\mu}\lambda_B \frac{S - S_L}{S_V - S}, \tag{1}$$

where $\rho = 8.3 \times 10^{22}$ cm^{-3} is the atomic density of ZnO, $\mu = 3 \times 10^{15}$ s^{-1} is the positron trapping coefficient for negatively charged vacancies at room temperature, and $\lambda_B = 6 \times 10^9$ s^{-1} is the annihilation rate in the ZnO lattice. S is the measured S parameter, and $S_L = 1$ and $S_V = 1.050$ are used as the normalized parameters for the ZnO lattice annihilation and the V_{Zn} annihilation, respectively [23,24,32,33]. Figure 3 shows the estimated V_{Zn} concentration from Eq. (1) vs the corresponding weighted mean of the Al concentration for samples Al-1050 and Al-1200 at different positron implantation energies. The weighted mean concentration is determined by weighting the measured Al profiles by the Makhov profiles (see Fig. 1). As evident from Fig. 3, there is a strong relation between the concentrations of V_{Zn} and Al. Assuming that the charge carrier concentration is in an extrinsic regime, that is, governed by the Al concentration, the slope of the line b

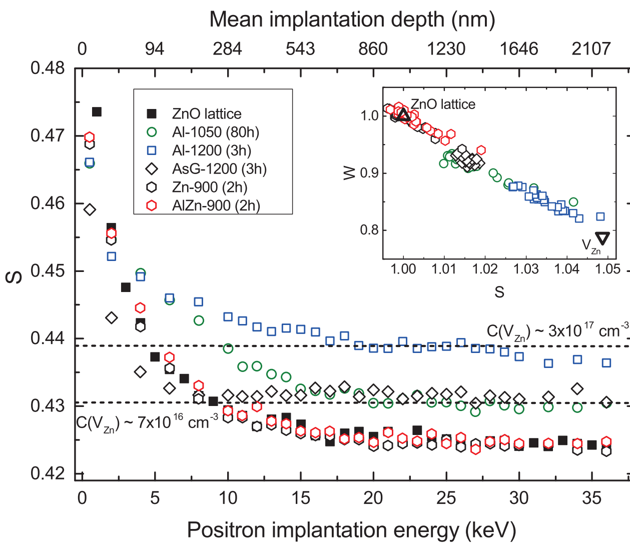

FIG. 2. S parameter vs positron implantation energy for the intentionally doped samples Al-1050, Al-1200, and AlZn-900 and for the undoped reference samples AsG-1200 and Zn-900. The dashed lines show the corresponding concentrations of V_{Zn}, as estimated by Eq. (1). The inset displays the normalized S and W parameters.

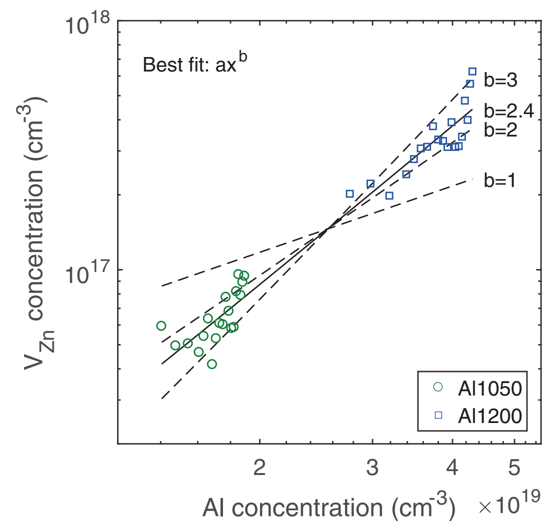

FIG. 3. V_{Zn} concentration vs Al concentration, as measured by PAS and SIMS, respectively. The straight solid line shows the best least-squares fit to the combined data with a slope of $b = 2.4$. Also shown (dotted lines) are the best fits with the constraints $b = 1, 2$, and 3.

in Fig. 3 should be given by the charge state of V_{Zn} at the given condition. The best least-squares power series fit (ax^b) to the experimental data exhibits a slope of $b = 2.4 \pm 0.2$. Also shown in Fig. 3 are the best fits with the constraints $b = 1, 2$, and 3. Here, it should be underlined that also the heat treatment temperature plays a role in the resulting $C_{V_{\mathrm{Zn}}}$, and at a given Al concentration a higher $C_{V_{\mathrm{Zn}}}$ can be expected for the Al-1200 sample than for the Al-1050 one. This is corroborated by the significant value of $C_{V_{\mathrm{Zn}}}$ observed for the (undoped) AsG-1200 control sample (Fig. 2). Hence, the slope of $b = 2.4$ contains also a "thermal contribution" which may account for the slight deviation from a quadratic dependence in Fig. 3. Accordingly, the data in Fig. 3 strongly suggest that -2 is the prevailing charge state of V_{Zn} in the intentionally doped samples.

B. Dopant diffusion vs Fermi level position

The relation between V_{Zn}^{2-} and the Al concentration (Fig. 3) encourages investigation of the Al diffusion at different Fermi level positions, i.e., tuning the availability of V_{Zn}^{2-} in the bulk ZnO. Similar to that observed for Al, Ga doping has been shown to yield highly conductive ZnO samples [34–36]. In addition, the diffusion of Ga in ZnO has been demonstrated to exhibit characteristic boxlike depth profiles similar to those observed for Al [4,25,37], although holding a slightly higher diffusivity.

Figure 4 shows the Al and Ga concentration vs depth distributions for the predoped sample (see Table I) after sequential heat treatments (30 min) from 700 °C to 1150 °C. At 850 °C, in-diffusion of Al becomes detectable. The characteristics of the Al diffusion profiles in Fig. 4 deviate strongly from those in Fig. 1 and those previously reported in Ref. [4], where steeper slopes at the diffusion fronts were observed. It can be noted that the about two orders of magnitude higher concentration of Al in the deposited film, compared to that in the bulk, merely indicates that the ambient conditions (vacuum/argon) during deposition cause supersaturation of Al in the heavily Al doped film. Furthermore, Ga migrates from the bulk to the film/bulk interface already at 700 °C and into the Al-doped film with an apparent solid solubility of 3–4 × 10^{19} cm^{-3} for $T_c \geqslant 800$ °C. Moreover, at 800 °C–900 °C the Ga diffusion profiles resemble that of a complementary error function [erfc($-x$), with x being the distance from the interface], i.e., an analytical solution of Fick's law for diffusion in a semi-infinite solid with a constant diffusion source.

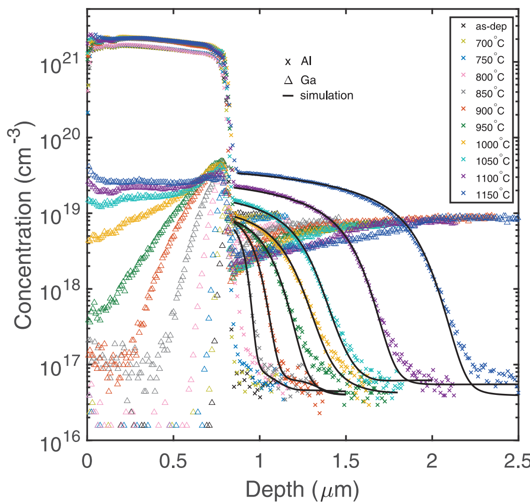

FIG. 4. Experimental Al (crosses) and Ga (triangles) concentrations vs depth distribution of the predoped sample sequentially heat treated for 30 min from 700 °C to 1150 °C. The solid lines show the best fit to the experimental Al diffusion profiles (from 850 °C).

As the temperature is increased above 1000 °C, the shape of the Al profiles in Fig. 4 exhibit an increased flattening in the shoulder region. This occurs when the bulk surface concentration (apparent solid solubility) of Al exceeds the predoped level of Ga in the bulk (1 × 10^{19} cm^{-3}). Below this level, which will be referred to as the "isoconcentration regime," the Al bulk surface concentration at all the different temperatures (850 °C–1000 °C) approximately equals the predoped level of Ga. Interestingly, in this regime the in-diffusion of Al is associated with an equal out-diffusion of Ga, such that the total content of dopants (Al+Ga) within the in-diffused region is maintained. This represents an isoconcentration regime that for true tracer diffusion conditions results in diffusion without an electrochemical potential gradient present, thus yielding erfc-like profiles [38]. However, in our case, with similar but not identical dopants, such an approach slightly overestimates the experimental profiles (not shown). The slightly more mobile Ga dopants [25] diffuse out of the bulk (to the film), and a net loss of total dopants occurs in the bulk (deep end of the Al profiles) after Al in-diffusion (compare the Ga concentration at depths beyond the Al tail before and after diffusion). This gives a contribution to the electrochemical potential gradient and a small (retarded) deviation from an erfc behavior. Not surprisingly, this non-erfc behavior becomes even more pronounced above the isoconcentration regime ($T_c > 1000$ °C), where the apparent Al solubility is well above the background concentration of Ga, resulting in a larger gradient in the electrochemical potential.

1. Reaction diffusion model

From the above discussion, both Al and Ga need to be considered in order to account for the experimental Al diffusion data in Fig. 4. As previously shown for both Al and Ga in undoped ZnO [4,25,39], their diffusion can be explained via a mechanism invoking Al-/Ga-vacancy pairs. The pairs form and break up according to the following reactions:

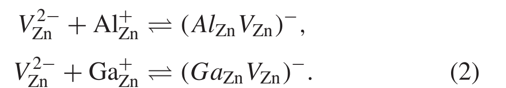

$$V_{\mathrm{Zn}}^{2-} + \mathrm{Al}_{\mathrm{Zn}}^{+} \rightleftharpoons (Al_{\mathrm{Zn}} V_{\mathrm{Zn}})^{-},$$
$$V_{\mathrm{Zn}}^{2-} + \mathrm{Ga}_{\mathrm{Zn}}^{+} \rightleftharpoons (Ga_{\mathrm{Zn}} V_{\mathrm{Zn}})^{-}. \quad (2)$$

In our reaction diffusion (RD) modeling, the deposited film of highly Al doped ZnO at the bulk crystal surface is considered as a source of $(\mathrm{Al}_{\mathrm{Zn}} V_{\mathrm{Zn}})^-$ pairs. That is, already formed $(\mathrm{Al}_{\mathrm{Zn}} V_{\mathrm{Zn}})^-$ pairs are injected into the bulk, and their flux is treated as a boundary condition in the simulations. As discussed in our previous report on Ga diffusion in ZnO [25], this assumption is corroborated by several theoretical and experimental results in the literature for both Al- and Ga-doped ZnO [4,10,11,21,40]. DFT calculations predict a low formation energy of $(\mathrm{Al}_{\mathrm{Zn}} V_{\mathrm{Zn}})^-$ and $(\mathrm{Ga}_{\mathrm{Zn}} V_{\mathrm{Zn}})^-$ pairs in highly n type samples under conditions comparable to

those in the present experiments [4,21,40]. This prediction is supported by electron paramagnetic resonance spectroscopy measurements [11], revealing that $(\mathrm{Al_{Zn}}V_{\mathrm{Zn}})^-$ prevails over V_{Zn} and $\mathrm{Al_{Zn}}$ in electron-irradiated Al-containing (10^{17} cm^{-3}) ZnO. Moreover, in a study using synchrotron x-ray absorption measurements combined with DFT [40] it was evidenced that the $(\mathrm{Al_{Zn}}V_{\mathrm{Zn}})^-$ pair is responsible for the suppressed net carrier concentration in highly Al doped ZnO samples. Based on these arguments, a high steady-state concentration of $(\mathrm{Al_{Zn}}V_{\mathrm{Zn}})^-$ pairs is expected to prevail in the Al-doped film. We can write the following full system of reaction-diffusion equations, with time t and position x:

$$\frac{\partial C_{(Al_{\mathrm{Zn}}V_{\mathrm{Zn}})^-}}{\partial t} = D_{(Al_{\mathrm{Zn}}V_{\mathrm{Zn}})^-}\frac{\partial^2 C_{(Al_{\mathrm{Zn}}V_{\mathrm{Zn}})^-}}{\partial x^2} - \frac{\partial C_{Al^+_{\mathrm{Zn}}}}{\partial t},$$
$$\frac{\partial C_{(Ga_{\mathrm{Zn}}V_{\mathrm{Zn}})^-}}{\partial t} = D_{(Ga_{\mathrm{Zn}}V_{\mathrm{Zn}})^-}\frac{\partial^2 C_{(Ga_{\mathrm{Zn}}V_{\mathrm{Zn}})^-}}{\partial x^2} - \frac{\partial C_{Ga^+_{\mathrm{Zn}}}}{\partial t}, \quad (3)$$

with

$$\frac{\partial C_{Al^+_{\mathrm{Zn}}}}{\partial t} = \nu C_{(Al_{\mathrm{Zn}}V_{\mathrm{Zn}})^-} - 4\pi R_c D_{V^{2-}_{\mathrm{Zn}}} C_{Al^+_{\mathrm{Zn}}} C_{V^{2-}_{\mathrm{Zn}}},$$
$$\frac{\partial C_{Ga^+_{\mathrm{Zn}}}}{\partial t} = \nu C_{(Ga_{\mathrm{Zn}}V_{\mathrm{Zn}})^-} - 4\pi R_c D_{V^{2-}_{\mathrm{Zn}}} C_{Ga^+_{\mathrm{Zn}}} C_{V^{2-}_{\mathrm{Zn}}}. \quad (4)$$

Here, $R_c = 1$ nm is the effective radius for capturing V^{2-}_{Zn} by $\mathrm{Al_{Zn}}$ or $\mathrm{Ga_{Zn}}$, while $\nu = \nu_0 e^{-[E_b + E_m(V^{2-}_{\mathrm{Zn}})]/k_B T}$ is the dissociation rate of the dopant-vacancy pair, with E_b being the binding energy of the dopant-vacancy pair, $E_m(V^{2-}_{\mathrm{Zn}})$ being the migration barrier of V^{2-}_{Zn}, k_B being the Boltzmann constant, and T being the temperature in degrees Kelvin. In the simulations, we assume an attempt frequency $\nu_0 = 10^{13}$ s^{-1} for the dissociation, i.e., the characteristic oscillation frequency of the lattice, and use $E_b(\mathrm{Al_{Zn}}V_{\mathrm{Zn}})^- = 1.31$ eV and $E_b(\mathrm{Ga_{Zn}}V_{\mathrm{Zn}})^- = 1.25$ eV, as previously predicted from theory [39].

At the interface between the highly n type deposited film and the bulk crystal surface, the abrupt change in the Al dopant distribution gives rise to an electric field and thus energy band bending. The effect of a spatially varying Fermi level upon dopant diffusion has previously been shown to cause an additional drift component for all defects involved in the diffusion process, resulting in an enhancement in the dopant diffusion by a factor between 1 (intrinsic) and 2 (far extrinsic) [41]. However, in a previous report of dopant diffusion [42], this effect was shown to have negligible importance for dopant diffusion at extrinsic conditions, and any drift component to the diffusion has therefore been omitted in the present work.

As indicated in Refs. [4,25], the transport capacity/coefficient of V^{2-}_{Zn} is much higher than that of the dopant-vacancy pair ($C_{V^{2-}_{\mathrm{Zn}}} D_{V^{2-}_{\mathrm{Zn}}} \gg C_{(X_{\mathrm{Zn}}V_{\mathrm{Zn}})^-} D_{(X_{\mathrm{Zn}}V_{\mathrm{Zn}})^-}$ for $X \in \{\mathrm{Al, Ga}\}$) and is the reason for the abrupt diffusion fronts observed for Al/Ga in undoped ZnO (see Fig. 1 and Refs. [4,25]). This means that, at steady-state conditions, the distribution of V^{2-}_{Zn} will effectively be controlled only by the charge neutrality of the system,

$$n = C_{\mathrm{Al}^+_{\mathrm{Zn}}} + C_{\mathrm{Ga}^+_{\mathrm{Zn}}} - C_{(\mathrm{Al_{Zn}}V_{\mathrm{Zn}})^-} - C_{(\mathrm{Ga_{Zn}}V_{\mathrm{Zn}})^-} - 2C_{V^{2-}_{\mathrm{Zn}}}. \quad (5)$$

Further, as outlined in Ref. [4], the concentration of V^{2-}_{Zn} hinges on both the local Fermi level position and temperature:

$$C_{V^{2-}_{\mathrm{Zn}}}(\epsilon_F, T) = \frac{\rho}{2} e^{-\frac{E_{f,0}(V^{2-}_{\mathrm{Zn}}) - 2\epsilon_F}{k_B T}}, \quad (6)$$

where $\rho/2$ is the number of lattice sites in the zinc sublattice and $E_{f,0}(V^{2-}_{\mathrm{Zn}})$ is the formation energy of V^{2-}_{Zn} where the local Fermi level ϵ_F is positioned at the valence band maximum. ϵ_F can be approximated as

$$\epsilon_F(n, T) = E_c(T) + k_B T \ln\left(\frac{n}{N_c(T)}\right), \quad (7)$$

where $E_c(T)$ is the position of the conduction band edge relative to the valence band edge (i.e., the band gap $E_g = E_c$) and $N_c(T)$ is the conduction band effective density of states. The narrowing of the band gap, from 3.3 eV at room temperature, as a function of increasing temperature is taken as $\Delta E_g = 80.5 - 0.52T$ (meV), as extrapolated from band-gap measurements in the temperature range 100 °C–500 °C by Hauschild *et al.* [43]. Combining Eqs. (6) and (7) gives the concentration of V^{2-}_{Zn} as a function of the charge carrier concentration and temperature:

$$C_{V^{2-}_{\mathrm{Zn}}}(n, T) = \frac{\rho}{2} e^{-\frac{E_{f,0}(V^{2-}_{\mathrm{Zn}}) - 2E_c(T)}{k_B T}} \left(\frac{n}{N_c(T)}\right)^2. \quad (8)$$

This implies that the diffusion of Al and Ga is described by solving the semilinear diffusion equations of the dopant-vacancy pairs [Eq. (3)], with their association and dissociation rates described by Eq. (4) and with the concentration of V^{2-}_{Zn} given by Eq. (8). Note that, solving Eq. (8) requires a value of the formation energy of V^{2-}_{Zn} when ϵ_F is at the valence band maximum ($E_{f,0}(V^{2-}_{\mathrm{Zn}})$). For this, we are guided by estimates from previous DFT reports [14,21,22,39] and set $E_{f,0}(V^{2-}_{\mathrm{Zn}}) = 7.4$ eV. Hence, using Eq. (8), depth profiles of $C_{V^{2-}_{\mathrm{Zn}}}$ can be estimated numerically if $n(x)$ is known. We note further that, as long as the transport capacity of V^{2-}_{Zn} is higher than that of the dopant-vacancy pair, $E_m(V^{2-}_{\mathrm{Zn}})$ is not needed to solve the full system of differential equations [Eqs. (3), (4), (5), and (8)]. This was shown in Ref. [25] for Ga diffusion, where $E_m(V^{2-}_{\mathrm{Zn}})$, which is inherent in both ν and $D_{V^{2-}_{\mathrm{Zn}}}$, cancels at these conditions of the transport capacities.

2. Al diffusion energetics

The results of the reaction-diffusion simulations giving the best fit to the experimental Al profiles are shown as solid lines in Fig. 4. The corresponding extracted diffusivities vs the inverse absolute temperature are given in Fig. 5, and similarly, the extracted solubilities are depicted in Fig. 6. Both the diffusion parameters for the Al-vacancy pair and the effective Al diffusion are presented, where the former are extracted directly from the reaction-diffusion equations. For the latter, the apparent Al solid solubility, denoted by C^S_{Al}, is taken as the measured concentration of Al at the bulk surface $C_{\mathrm{Al}}(x_{\mathrm{bulk}} = 0)$, and the effective Al diffusivity is deduced as follows; provided that the Al atoms mainly dissolve substitutionally at the zinc site (with $C_{\mathrm{Al_{Zn}}} \gg C_{\mathrm{Al_{Zn}}V_{\mathrm{Zn}}}$) and that $(\mathrm{Al_{Zn}}V_{\mathrm{Zn}})^-$ is the predominant Al diffusing species, the effective diffusivity

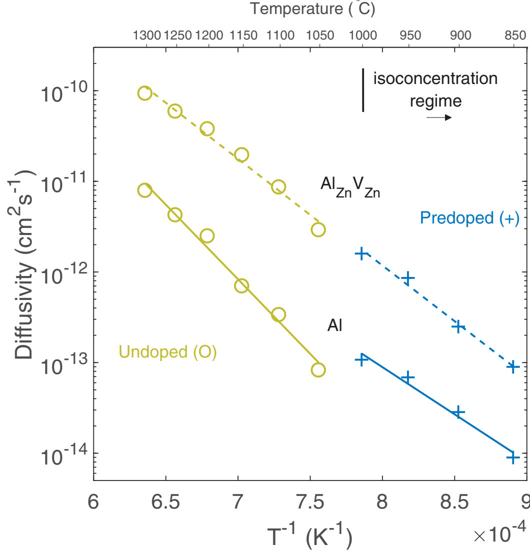

FIG. 5. Apparent diffusivities vs inverse absolute temperature of the $\mathrm{Al_{Zn}}V_{\mathrm{Zn}}$ pair in undoped ZnO (from Ref. [4], circles) and in predoped ZnO (crosses). Also shown are the effective diffusivity values D_{Al} (solid lines), as estimated from Eq. (9). For the predoped sample, only diffusivities in the isoconcentration regime (i.e., below 1050 °C) are included.

of Al under local equilibrium conditions can be expressed by (cf. [41,44,45])

$$D_{\mathrm{Al}} = \frac{C^S_{\mathrm{Al_{Zn}}V_{\mathrm{Zn}}} D_{\mathrm{Al_{Zn}}v_{\mathrm{Zn}}}}{C^S_{\mathrm{Al_{Zn}}}}. \tag{9}$$

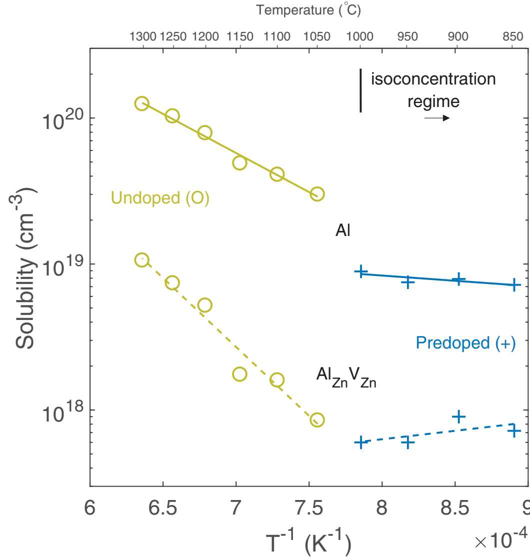

FIG. 6. Apparent solubilities vs inverse absolute temperature of the $\mathrm{Al_{Zn}}V_{\mathrm{Zn}}$ pair in undoped ZnO (from Ref. [4], circles) and in predoped ZnO (crosses). Also shown are the apparent Al solid solubility values $C^S_{Al} = C_{Al}(x_{\mathrm{bulk}} = 0)$ (solid lines), as measured by SIMS. For the predoped sample, only solubilities in the isoconcentration regime (i.e., below 1050 °C) are shown.

TABLE II. Diffusivity and solubility values for $\mathrm{Al_{Zn}}V_{\mathrm{Zn}}$ and Al in undoped ZnO [4] and predoped ZnO (isoconcentration regime), as found from the least-squares best fit of the extracted values in Figs. 5 and 6.

Process	Undoped E_m, E_a, E_f (eV)	Undoped D_0, C^S_0 (cm^2 s^{-1}, cm^{-3})	Predoped E_m, E_a, E_f (eV)	Predoped D_0, C^S_0 (cm^2 s^{-1}, cm^{-3})
$D_{\mathrm{Al_{Zn}}V_{\mathrm{Zn}}}$	2.5 ± 0.2	8×10^{-3}	2.4 ± 0.2	8×10^{-3}
D_{Al}	3.3 ± 0.2	3×10^{-1}	2.0 ± 0.3	2×10^{-5}
$C^S_{\mathrm{Al_{Zn}}V_{\mathrm{Zn}}}$	1.9 ± 0.2	1×10^{25}	-0.2 ± 0.3	7×10^{16}
C^S_{Al}	1.1 ± 0.1	3×10^{23}	0.1 ± 0.1	3×10^{19}

Here, $C^S_{\mathrm{Al_{Zn}}}$ is taken as the apparent solid solubility C^S_{Al} as measured by SIMS, and $C^S_{\mathrm{Al_{Zn}V_{Zn}}}$ is extracted from the simulations at $x_{\mathrm{bulk}} = 0$. For comparison, previous experimental data of Al diffusion in undoped ZnO [4] have been remodeled using the simulation parameters as described above, and the corresponding values are included in Figs. 5 and 6 (circles). As seen in Fig. 6, the predoped sample reveals apparent solubilities with almost no temperature dependence in the interval 850 °C–1000 °C (isoconcentration regime). As implied above, this weak temperature dependence arises because the sample is predoped to concentrations above the equilibrium solid solubility limit of Al at 1000 °C and below. Table II lists all the extracted activation energies and preexponential factors deduced from Figs. 5 and 6.

The migration activation energy for the Al-vacancy pair in the isoconcentration regime is found to be $E_{\mathrm{m}}(\mathrm{Al_{Zn}}V_{\mathrm{Zn}})^- = 2.4$ eV (see Fig. 5 and Table II). Within the uncertainties given in Table II, this is identical to that found in undoped ZnO (2.5 eV). Indeed, since the migration activation energy of the pair represents only the barrier required for Al to jump to an already associated V_{Zn}, no influence by the Fermi level position is anticipated. This result supports the validity of our simulation and model and the DFT values used as input. Further, the overall activation energy E_a for the diffusion of Al in the predoped sample (isoconcentration regime) is found to be, within the uncertainties given in Table II, similar to the migration barrier of the pair. This is a consequence of the similar temperature dependences of $C^S_{\mathrm{Al_{Zn}V_{Zn}}}$ and C^S_{Al} [see Eq. (9)]. In contrast, for the undoped sample $E_a(\mathrm{Al})$ is 0.8 eV higher than $E_{\mathrm{m}}(\mathrm{Al_{Zn}}V_{\mathrm{Zn}})^-$, reflecting the higher $E_f(V^{2-}_{\mathrm{Zn}})$ in this more resistive sample. Also notice that D_{Al} is higher in the predoped ZnO, which is a result of the reduced $E_f(V^{2-}_{\mathrm{Zn}})$.

In the simulations for the undoped sample, we have used a prefactor for $D_{V^{2-}_{\mathrm{Zn}}}$ of $D_0(V^{2-}_{\mathrm{Zn}}) = 10^{-2}$ cm^2/s, which reflects the crystal geometry of ZnO and assumes no migration or formation entropy contribution. However, it was recently demonstrated by Azarov *et al.* [46] that Ga doping ZnO strongly enhances the Zn self-diffusion in ZnO and, in particular, that $D_0(V^{2-}_{\mathrm{Zn}})$ scales with the Ga concentration. Accordingly, we have used a slightly higher value (by a factor of ∼10) for $D_0(V^{2-}_{\mathrm{Zn}})$ in the simulations for the predoped sample (1.2×10^{-1} cm^2/s). As a result, the two $D_{\mathrm{Al_{Zn}}V_{\mathrm{Zn}}}$ lines in Fig. 5 align (as anticipated) and support an entropy contribution of $2.5k_B$ for the diffusion of V^{2-}_{Zn} in the predoped sample.

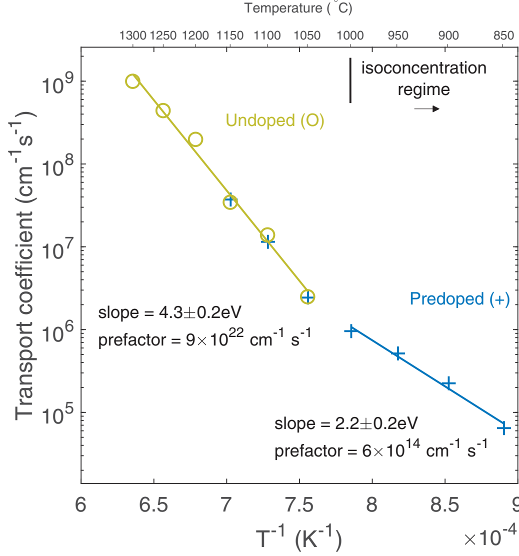

FIG. 7. Comparison of the transport coefficients vs inverse absolute temperature for Al in undoped ZnO (Ref. [4], circles) and in predoped ZnO (crosses).

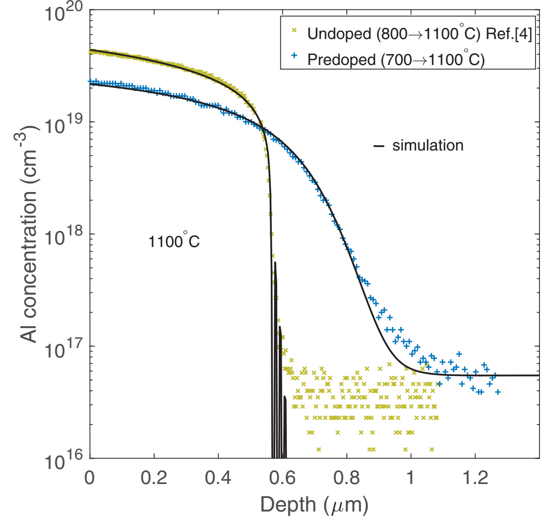

FIG. 8. Comparison of the experimental Al diffusion profiles at 1100 °C in two samples with different donor background concentrations, undoped ($\sim 3 \times 10^{13}$ cm^{-3}, Ref. [4]) and predoped (1×10^{19} cm^{-3}). For clarity, the deposited films have been excluded, and the film-bulk interface has been set to zero at the abscissa. The temperature intervals indicate the prehistory of the sequential 30-min heat treatments in steps of 50 °C.

Figure 7 shows the Arrhenius behavior of the Al transport coefficients/capacity ($C^S_{\mathrm{Al_{Zn}}V_{\mathrm{Zn}}} D_{\mathrm{Al_{Zn}}V_{\mathrm{Zn}}}$ or $C^S_{\mathrm{Al_{Zn}}} D_{\mathrm{Al}}$) for the undoped and predoped samples. Within the isoconcentration regime, the transport coefficients reveal a pronounced increase compared to the expected and extrapolated data for the undoped sample at similar temperatures. This can be explained by the fact that the exponential decrease in $C^S_{\mathrm{Al_{Zn}}}$ with ϵ_F [$E_f(\mathrm{Al}^+_{\mathrm{Zn}})$ is proportional to ϵ_F] is overruled by the squared exponential increase in D_{Al} with ϵ_F [$E_f(V^{2-}_{\mathrm{Zn}})$ has a -2 dependence on ϵ_F]. Hence, their product increases as ϵ_F moves towards the conduction band minimum. On the other hand, above the isoconcentration regime the transport capacity of Al in the predoped sample is comparable to that in the undoped sample (Fig. 7). This is somewhat unexpected when considering the different diffusion characteristics of Al in the undoped and predoped samples illustrated in Fig. 8, where we compare the profiles after the 1100 °C anneal. One reason for this similarity in transport coefficient may be that the in-diffusion of Al is not controlled by the actual Al solid solubility but rather limited by the rate of transport of Al from the deposited film into the bulk crystal at high temperatures. This may in turn be interpreted in terms of a restriction in the formation of $(\mathrm{Al_{Zn}}V_{\mathrm{Zn}})^-$ pairs in the film and/or an interfacial barrier.

The demonstrated Fermi level dependence of the Al diffusion strongly suggests that the diffusion of Al is mediated by V_{Zn}. Other diffusion mechanisms may possibly result in similar profiles; however, the most likely alternative candidates can arguably be ruled out based on our experimental results. For instance, if the diffusion of interstitial Al prevailed in the bulk, either (i) as a vacancy-assisted dissociation process or (ii) through kick out by interstitial Zn, an enhanced Al diffusivity at increased ϵ_F is not expected. In both such cases, the increased ϵ_F would likely cause the effective diffusivity of Al to decrease due to (i) a high concentration of V_{Zn} traps or (ii) a low concentration of interstitial zinc available to kick out substitutional Al. Moreover, Al diffusion proceeding through a direct interstitial mechanism can also be excluded as it would yield erfc-like profiles with no dependence on ϵ_F.

IV. SUMMARY

We have studied the influence of Al doping on the formation of V_{Zn} in single-crystalline ZnO by using a combination of SIMS and PAS analysis. Conversely, we have also investigated how the supply of zinc vacancies affects the diffusion of Al, which is performed by introducing Ga as a background donor dopant. The concentration of V_{Zn} is found to hold a quadratic dependence on the Al-doping concentration, evidencing the prevailing -2 charge state of V_{Zn} in n-ZnO. Further, the diffusion of Al is well described at different donor background concentrations using a reaction-diffusion model, which also accounts for the diffusion and redistribution of the Ga background donors. In predoped ZnO, the Al diffusion is strongly influenced by the high free-charge-carrier concentration (Ga donors) and gives rise to Al vs depth profiles that are very different from those in undoped ZnO. The effective diffusivity of Al is enhanced in the predoped sample, which is attributed to the higher abundance of the mediating V^{2-}_{Zn}. Using state-of-the-art DFT results from the literature [39] as input in the reaction-diffusion simulations, we obtain a migration barrier of the $(\mathrm{Al_{Zn}}V_{\mathrm{Zn}})^-$ pair of 2.4 ± 0.2 eV. This value is extracted independently from the two different experiments using undoped and predoped samples, respectively. The value is also in close agreement with results from previous DFT predictions [39] (2.55 eV).

ACKNOWLEDGMENTS

We thank V. Prozheeva and N. Segercrantz for assistance with the PAS measurements and H. N. Riise for the growth of sputter-deposited films. Financial support from the Research Council of Norway for funding of the Norwegian PhD Network on Nanotechnology for Microsystems (Grant No. 221860/F40), DYNAZOx-project (Grant No. 221992), Salient (Grant No. 239895), the University of Oslo, and the Norwegian Micro- and Nano-Fabrication Facility (NorFab Grant No. 197411/V30) is gratefully acknowledged.

[1] T. M. Børseth, J. S. Christensen, K. Maknys, A. Hallén, B. G. Svensson, and A. Y. Kuznetsov, Superlattices Microstruct. **38**, 464 (2005).
[2] N. H. Nickel, Phys. Rev. B **73**, 195204 (2006).
[3] K. M. Johansen, J. S. Christensen, E. V. Monakhov, A. Y. Kuznetsov, and B. G. Svensson, Appl. Phys. Lett. **93**, 152109 (2008).
[4] K. M. Johansen, L. Vines, T. S. Bjørheim, R. Schifano, and B. G. Svensson, Phys. Rev. Appl. **3**, 024003 (2015).
[5] A. Y. Azarov, K. E. Knutsen, P. T. Neuvonen, L. Vines, B. G. Svensson, and A. Y. Kuznetsov, Phys. Rev. Lett. **110**, 175503 (2013).
[6] A. Y. Azarov, A. Hallén, X. L. Du, P. Rauwel, A. Y. Kuznetsov, and B. G. Svensson, Br. J. Appl. Phys. **115**, 073512 (2014).
[7] A. Azarov, L. Vines, P. Rauwel, E. Monakhov, and B. G. Svensson, Br. J. Appl. Phys. **119**, 185705 (2016).
[8] P. T. Neuvonen, L. Vines, V. Venkatachalapathy, A. Zubiaga, F. Tuomisto, A. Hallén, B. G. Svensson, and A. Y. Kuznetsov, Phys. Rev. B **84**, 205202 (2011).
[9] J.-i. Nomoto, M. Konagai, K. Okada, T. Ito, T. Miyata, and T. Minami, Thin Solid Films **518**, 2937 (2010).
[10] D. C. Look, K. D. Leedy, L. Vines, B. G. Svensson, A. Zubiaga, F. Tuomisto, D. R. Doutt, and L. J. Brillson, Phys. Rev. B **84**, 115202 (2011).
[11] J. E. Stehr, K. M. Johansen, T. S. Bjørheim, L. Vines, B. G. Svensson, W. M. Chen, and I. A. Buyanova, Phys. Rev. Appl. **2**, 021001 (2014).
[12] D. C. Look, J. W. Hemsky, and J. R. Sizelove, Phys. Rev. Lett. **82**, 2552 (1999).
[13] A. F. Kohan, G. Ceder, D. Morgan, and C. G. Van de Walle, Phys. Rev. B **61**, 15019 (2000).
[14] A. Janotti and C. G. Van de Walle, Phys. Rev. B **76**, 165202 (2007).
[15] D. G. Thomas, J. Phys. Chem. Solids **3**, 229 (1957).
[16] C. Bhoodoo, A. Hupfer, L. Vines, E. V. Monakhov, and B. G. Svensson, Phys. Rev. B **94**, 205204 (2016).
[17] L. Vines and A. Kuznetsov, in *Oxide Semiconductors*, Semiconductors and Semimetals Vol. 88 (Elsevier/Academic, San Diego, 2013), p. 67.
[18] L. Vines, E. V. Monakhov, R. Schifano, W. Mtangi, F. D. Auret, and B. G. Svensson, Br. J. Appl. Phys. **107**, 103707 (2010).
[19] K. M. Johansen, A. Zubiaga, I. Makkonen, F. Tuomisto, P. T. Neuvonen, K. E. Knutsen, E. V. Monakhov, A. Y. Kuznetsov, and B. G. Svensson, Phys. Rev. B **83**, 245208 (2011).
[20] A. Janotti and C. G. Van de Walle, J. Cryst. Growth **287**, 58 (2006).
[21] D. O. Demchenko, B. Earles, H. Y. Liu, V. Avrutin, N. Izyumskaya, Ü. Özgür, and H. Morkoç, Phys. Rev. B **84**, 075201 (2011).
[22] Y. K. Frodason, K. M. Johansen, T. S. Bjørheim, B. G. Svensson, and A. Alkauskas, Phys. Rev. B **95**, 094105 (2017).
[23] F. Tuomisto, V. Ranki, K. Saarinen, and D. C. Look, Phys. Rev. Lett. **91**, 205502 (2003).
[24] F. Tuomisto, K. Saarinen, D. C. Look, and G. C. Farlow, Phys. Rev. B **72**, 085206 (2005).
[25] T. N. Sky, K. M. Johansen, H. N. Riise, B. G. Svensson, and L. Vines, Br. J. Appl. Phys. **123**, 055701 (2018).
[26] W. Lin, K. Ding, Z. Lin, J. Zhang, J. Huang, and F. Huang, Cryst. Eng. Commun. **13**, 3338 (2011).
[27] F. Tuomisto and I. Makkonen, Rev. Mod. Phys. **85**, 1583 (2013).
[28] S. Valkealahti and R. M. Nieminen, Appl. Phys. A **32**, 95 (1983).
[29] S. Valkealahti and R. M. Nieminen, Appl. Phys. A **35**, 51 (1984).
[30] H. E. Hansen and U. Ingerslev-Jensen, J. Phys. D **16**, 1353 (1983).
[31] V. Prozheeva, K. M. Johansen, P. T. Neuvonen, A. Zubiaga, L. Vines, A. Y. Kuznetzov, and F. Tuomisto, Mater. Sci. Semicond. Process. **69**, 19 (2017).
[32] A. Zubiaga, F. Tuomisto, V. A. Coleman, H. H. Tan, C. Jagadish, K. Koike, S. Sasa, M. Inoue, and M. Yano, Phys. Rev. B **78**, 035125 (2008).
[33] F. Tuomisto, in *Semiconductors and Semimetals*, Oxide Semiconductors, Vol. 88 (Academic, San Diego, 2013), Chap. 2, pp. 39–65
[34] H. Y. Liu, V. Avrutin, N. Izyumskaya, M. A. Reshchikov, Ü. Özgür, and H. Morkoç, Phys. Status Solidi RRL **4**, 70 (2010).
[35] T. Minami, Semicond. Sci. Technol. **20**, S35 (2005).
[36] D. C. Look, K. D. Leedy, D. H. Tomich, and B. Bayraktaroglu, Appl. Phys. Lett. **96**, 062102 (2010).
[37] T. Nakagawa, I. Sakaguchi, M. Uematsu, Y. Sato, N. Ohashi, H. Haneda, and Y. Ikuhara, Jpn. J. Appl. Phys. **46**, 4099 (2007).
[38] E. Antoncik, J. Electrochem. Soc. **142**, 3170 (1995).
[39] D. Steiauf, J. L. Lyons, A. Janotti, and C. G. V. de Walle, APL Mater. **2**, 096101 (2014).
[40] J. T-Thienprasert, S. Rujirawat, W. Klysubun, J. N. Duenow, T. J. Coutts, S. B. Zhang, D. C. Look, and S. Limpijumnong, Phys. Rev. Lett. **110**, 055502 (2013).
[41] P. M. Fahey, P. B. Griffin, and J. D. Plummer, Rev. Mod. Phys. **61**, 289 (1989).
[42] E. Antoncik, Phys. Status Solidi A **149**, 557 (1995).
[43] R. Hauschild, H. Priller, M. Decker, J. Brückner, H. Kalt, and C. Klingshirn, Phys. Status Solidi C **3**, 976 (2006).
[44] M. Uematsu, Br. J. Appl. Phys. **82**, 2228 (1997).
[45] H. Bracht, Phys. Rev. B **75**, 035210 (2007).
[46] A. Azarov, V. Venkatachalapathy, Z. Mei, L. Liu, X. Du, A. Galeckas, E. Monakhov, B. G. Svensson, and A. Kuznetsov, Phys. Rev. B **94**, 195208 (2016).

Paper IV

The Interaction between Lithium Acceptors and Gallium Donors in Zinc Oxide
T. N. Sky, K. M. Johansen, Y. K. Frodason, B. G. Svensson, and L. Vines
J. Appl. Phys. 124, 245702 (2018)

JOURNAL OF APPLIED PHYSICS 124, 245702 (2018)

The interaction between lithium acceptors and gallium donors in zinc oxide

T. N. Sky,[a)] K. M. Johansen, Y. K. Frodason, B. G. Svensson, and L. Vines
Department of Physics/Center for Materials Science and Nanotechnology, University of Oslo, P.O. Box 1048 Blindern, N-0316 Oslo, Norway

(Received 26 September 2018; accepted 6 December 2018; published online 26 December 2018)

Diffusion of lithium (Li) in uniformly gallium (Ga)-doped monocrystalline bulk zinc oxide (ZnO) is studied over a wide temperature range (500–1150 °C) and is demonstrated to be dictated by the distribution of Ga. Below 800 °C, the indiffusion of Li from a Li-doped ZnO sputtered film into n^+ single crystalline ZnO yields an abrupt and compensated Li-doped box region with the Li concentration matching the free-electron concentration, in accordance with several previous experimental and theoretical reports. However, experimental observations of Li-diffusion at higher temperatures reveal a dissociative diffusion mechanism for heat treatments up to 1150 °C. By employing a reaction-diffusion model that includes both Li and Ga, a dissociation energy of 4.6 eV is obtained from the experimental Li diffusion data. This is in excellent agreement with theoretical results for the dissociation of $(Li_{Zn}Ga_{Zn})^0$ (4.8 eV) into Li_i^+ and $(Ga_{Zn}V_{Zn})^-$ and suggests that this neutral and stable acceptor-donor pair prevails in Li- and Ga-doped ZnO. *Published by AIP Publishing.*
https://doi.org/10.1063/1.5063326

I. INTRODUCTION

The behavior of lithium (Li) in crystalline zinc oxide (ZnO) has been studied for many decades, with the first report on experimental Li diffusion as early as 1960.[1] Both donor and acceptor properties of Li were observed early on and it was suggested that Li substituting Zn (Li_{Zn}^-) and interstitial Li (Li_i^+) was the identity of the acceptor and donor states, respectively.[1] This amphoteric behavior of Li is now well established based on more recent experimental[2–4] and theoretical[5,6] results. Li has been shown to primarily reside on the Zn site in n-type ZnO,[4] demonstrating the self-compensating effect of Li, with Li_{Zn}^- being favorable when the Fermi level (ϵ_F) is close to the conduction band minimum (CBM) and under oxygen rich conditions, while Li_i^+ would prevail for ϵ_F close to the valence band maximum (VBM) and under Zn-rich conditions.

Li diffusion in ZnO has previously been studied at temperatures up to 600 °C by Lander[1] and Knutsen *et al.*[7] under Zn-rich and O-rich conditions, respectively. In both reports, the diffusion of Li was described by assuming Li_i^+ to be the mobile species, while Li_{Zn}^- was considered immobile in the studied temperature range. The model assumed a kick-out mechanism between substitutional Zn by mobile Li_i^+ into stable Li_{Zn}^- and highly mobile Zn_i^{2+} (the migration barrier of 0.55 eV[8]), with extracted Li_i^+ migration barriers of 0.98 eV[1] and 1.34 eV[7] reported for the two studies, respectively.

Theoretical results by Carvalho *et al.*[6] using hybrid functional calculations reported an ionization energy of 0.6–1.1 eV for Li_{Zn}^-, while a migration barrier of 0.6–0.7 eV for the diffusion of Li_i^+ was found. In addition, they further suggested that under O-rich conditions, the dominant diffusion process corresponds to a dissociative mechanism requiring a substantial activation energy. However, such a diffusion mechanism would be observed at higher temperatures than that previously reported.

In this work, we have used secondary ion mass spectrometry (SIMS) and hybrid density functional theory (DFT) to study the diffusion of Li into the single crystal Ga-doped bulk ZnO containing very low residual Li concentration in the as-grown state. The background concentration of Ga donors made it possible to investigate the diffusion of Li at Fermi-level positions close to CBM, i.e., wherein the interstitial configuration is expected to be highly unfavorable. Unlike previously reported experiments on Li diffusion in ZnO, the present study addresses the diffusion mechanisms of Li diffusion in the temperature range of 850–1150 °C, evidencing a dissociative mechanism that has not previously been shown experimentally. The results demonstrate that the diffusion of Li is controlled by the concentration and distribution of Ga, resulting in a close to one-to-one ratio between the Li and Ga concentrations at moderate temperatures. Combining the experimental SIMS results with hybrid DFT results using a reaction-diffusion type model,[9,10] the diffusion of Li is evidenced to proceed by a dissociative donor-vacancy assisted diffusion mechanism, where mobile Li_i^+ reacts with more stable $(Ga_{Zn}V_{Zn})^-$ pairs to produce neutral $(Li_{Zn}Ga_{Zn})^0$ pairs. A dissociation energy barrier of 4.6 eV is extracted in the modelling of the experimental data, which is in excellent agreement with the theoretical predictions of 4.8 eV for the dissociation of $(Li_{Zn}Ga_{Zn})^0$.

II. METHODS

A. Experimental

A thin film of Li-doped ZnO ($\sim 2 \times 10^{20}$ cm^{-3}) was deposited onto a hydrothermally grown single crystalline ($000\bar{1}$-oriented) bulk ZnO wafer, containing an as-grown uniform Ga concentration of 1×10^{19} cm^{-3} with a measured charge carrier concentration of 8×10^{18} cm^{-3}. The as-grown

[a)]t.n.sky@fys.uio.no

bulk wafers were obtained from the authors of Ref. 11, produced/grown using a modified hydrothermal method, resulting in a low residual Li concentration ($< 1 \times 10^{15}\,\mathrm{cm}^{-3}$). The deposition of the Li-rich thin film was carried out in a Semicore magnetron sputtering system using a Li-doped ZnO target ($Zn_{0.95}Li_{0.05}O$) with a purity of 99.95%, resulting in a 0.3 μm thick Li-doped ZnO film. After the deposition, the wafer was cleaved into two smaller samples (labelled A and B) by the use of a Rofin PowerLine E-25 SHG laser cutter. Sample A was sequentially heat treated for 15 min from 500 °C up to 800 °C in stages of 50 °C, while sample B received a similar procedure but at higher temperatures (850–1150 °C) and for longer times (30 min). A Cameca IMS7f Secondary Ion Mass Spectrometer (SIMS) equipped with a O_2 primary ion beam source was used to record the concentration vs depth profiles of Li and Ga. Absolute concentration values were obtained by measuring Li and Ga implanted reference samples, ensuring less than $\pm 10\%$ error in accuracy. For depth calibration, the sputtered crater depths were determined by a Dektak 8 stylus profilometer and a constant erosion rate was assumed.

B. Theoretical

First-principles calculations were performed by using the Heyd-Scuseria-Ernzerhof (HSE)[12] hybrid functional and the projector augmented wave method,[13–15] as implemented in the VASP code.[16,17] The fraction of the screened Hartree-Fock exchange was set to $\alpha = 37.5\%$,[18] which yields a bandgap (3.42 eV) and lattice parameters ($a = 3.244$ Å and $c = 5.194$ Å) that are in excellent agreement with experimental values.[19,20] All defect calculations were performed using a plane-wave energy cutoff of 500 eV, a special k-point at $k = (\frac{1}{4}, \frac{1}{4}, \frac{1}{4})$, and a 96-atom-sized wurtzite supercell.[21] Defect formation energies were calculated by following the well established formalism outlined in Refs. 22 and 23. For instance, the formation energy of Li_{Zn} in charge-state q is given by

$$E_f(\mathrm{Li}_{\mathrm{Zn}}^q) = E_{\mathrm{tot}}(\mathrm{Li}_{\mathrm{Zn}}^q) - E_{\mathrm{tot}}^{\mathrm{bulk}} + \mu_{\mathrm{Zn}} - \mu_{\mathrm{Li}} + q\epsilon_{\mathrm{F}}, \quad (1)$$

where $E_{\mathrm{tot}}(\mathrm{Li}_{\mathrm{Zn}}^q)$ and $E_{\mathrm{tot}}^{\mathrm{bulk}}$ denote the total energy of the defect-containing and pristine supercells, and μ_{Zn} and μ_{Li} are the chemical potential of the removed Zn- and added Li-atom, respectively. For charged defects, we applied the anisotropic[24] Freysoldt-Neugebauer-Van de Walle finite-size correction.[25,26] Oxygen rich conditions are considered, where μ_{Zn} corresponds to the total energy per the bulk metallic Zn atom plus the formation enthalpy of ZnO, i.e., $\mu_{\mathrm{Zn}} = E_{\mathrm{tot}}(\mathrm{Zn}) + \Delta H_f(\mathrm{ZnO})$. The solubility of Li is limited by the formation of Li_2O, and under oxygen rich conditions $\mu_{\mathrm{Li}} = E_{\mathrm{tot}}(\mathrm{Li}) + \frac{1}{2}\Delta H_f(\mathrm{Li_2O})$. Similarly, the solubility of Ga is limited by the formation of Ga_2O_3 and thus $\mu_{\mathrm{Ga}} = E_{\mathrm{tot}}(\mathrm{Ga}) + \frac{1}{2}\Delta H_f(\mathrm{Ga_2O_3})$.

III. RESULTS AND DISCUSSION

A. Li diffusion at moderate temperatures

Figure 1 shows the Li and Ga concentration vs depth profiles for the sample isocronally heat treated (15 min) at temperatures in the range 500–800 °C, as measured by SIMS. Already at 500 °C, Li starts to migrate from the 0.3 μm thick Li-doped ZnO film into the Ga-doped ZnO bulk. At these temperatures, Ga is practically immobile (cf. Ref. 10) showing only a slight out-diffusion to the film at 800 °C. The concentration of Li in the plateau of the very distinct box-like Li diffusion profiles is about 8–9$\times 10^{18}\,\mathrm{cm}^{-3}$ for all temperatures. Treatments up to 600 °C show a gradual increase in the effective diffusion length. However, at temperatures between 650 °C and 800 °C, only a small increase in the effective diffusion length is observed, indicating a depletion of mobile Li in the film. Furthermore, above 700 °C, a tail start to develop in the deep end of the Li box-profiles, indicative of a different process emerging at higher temperatures. This unfortunately limits the possibility to extract reliable diffusion parameters. However, the general diffusion behavior of Li at moderate temperatures (Fig. 1) is in accordance with that observed in previous reports,[1,7] where the diffusion of Li was explained to proceed by fast diffusing Li_i^+, while Li_{Zn}^- is practically immobile below 600 °C. In particular, it was found in Ref. 7 that the characteristic level at which the concentration of Li changes abruptly was correlated with the background concentration of ionized donors. Indeed, the experimental results presented in Fig. 1 strongly support this notion and further demonstrate that in the presence of a background doping of Ga, the diffusion of Li follows the concentration and distribution of Ga.

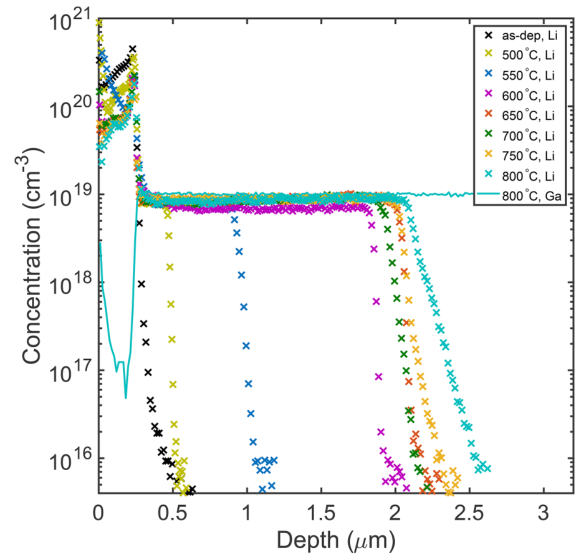

FIG. 1. Experimental Li and Ga concentration vs depth profiles of sample A isochronally heat treated (15 min) at temperatures 500–800 °C.

Experimental and theoretical studies of the amphoteric behavior of Li reported in the literature[2–6] show that high doping levels of Li lead to a highly compensated material. Indeed, the Li-doped ZnO film is shown to be highly resistive by 4-point probe measurements, with Li as the primary impurity. This suggests the presence of both Li_{Zn}^- and Li_i^+ in the film. Mobile Li_i^+ will diffuse into the n-type bulk; however, Li_i^+ will be highly unfavorable and is expected to convert into a more energetically favorable configuration, e.g., the substitutional Zn-site,

ensuring continued indiffusion from the film. Moreover, Fig. 1 suggests that Li is trapped by a defect stable up to ~750 °C after entering the bulk crystal, in good agreement with previous experiments.[1,7]

B. Li diffusion above 800 °C

Figure 2(a) shows the Li and Ga concentrations vs depth profiles for sample B after isochronal heat treatments (30 min) in the temperature range 850–1150 °C. After the 850 °C treatment, Li shows similar distinct box-like diffusion behavior as that observed for sample A above (Fig. 1). Note that the total amount of indiffused Li in sample B at 850 °C is higher (~1 μm deeper profile) than that observed for sample A at the same temperature (Fig. 1). The reason for this difference may be attributed to an outdiffusion of Li from the deposited film due to a longer accumulated diffusion time in sample A compared to sample B. Nevertheless, this difference will not affect our analysis below. Increasing the temperature above 950 °C clearly reveals that Li starts to redistribute, and the profiles extend over 20 μm into the bulk after the 1150 °C treatment. As shown in Fig. 2(b), the integrated concentration of Li within the indiffused profiles is effectively maintained at all temperatures, demonstrating that no additional influx of Li occurs from the film (or the outflux from the bulk) after the initial 850 °C treatment. This ensures a clear boundary condition, making it highly suitable to apply diffusion modelling.

Interestingly, the evolution of the Ga distribution within the initial indiffused box-region [Fig. 2(a)] shows a correlation to that of the Li distribution, or rather vice versa. The redistribution of Ga is observed for treatments exceeding 850 °C, in accordance with previous results[10] reporting a migration barrier of 2.4 eV for $(Ga_{Zn}V_{Zn})^-$ in ZnO. In addition to the out diffusion of Ga causing a gradient in the Ga distribution toward the film, Ga also forms a distinct pattern at the interface between the Li doped and undoped bulk material. This is particularly prominent after the 950 °C and 1000 °C treatments [see the redistribution at 3–4 μm shown in Fig. 2(c)], before it disappears again at higher temperatures. These features may be indicative of the presence of a considerable potential gradient across the Li-rich and Li-lean regions, as previously suggested for Li-doped ZnO.[7]

1. *Theoretical predictions of prevalent defects*

To get an overview of likely defect configurations that may be responsible for the initial Li "trapping" and subsequent apparent dissociation at higher temperatures, theoretical calculations using comparable conditions (oxygen-rich) were conducted. Figure 3(a) shows the formation energy vs the Fermi-level position (ϵ_F) for relevant defects, as obtained from hybrid DFT calculations. As can be seen, Li_i^+ is highly unfavorable under n-type conditions (ϵ_F close to CBM) and will readily convert into any of the more energetically favorable configurations Li_{Zn}^- or $(Li_{Zn}Ga_{Zn})^0$, if encountering either V_{Zn}^{2-} or $(Ga_{Zn}V_{Zn})^-$, respectively. The calculated stability of these substitutional Li-related defects is shown in Fig. 3(b), where the removal energy E_r and dissociation energy E_d of Li_{Zn}^- and $(Li_{Zn}Ga_{Zn})^0$ are given as a function of

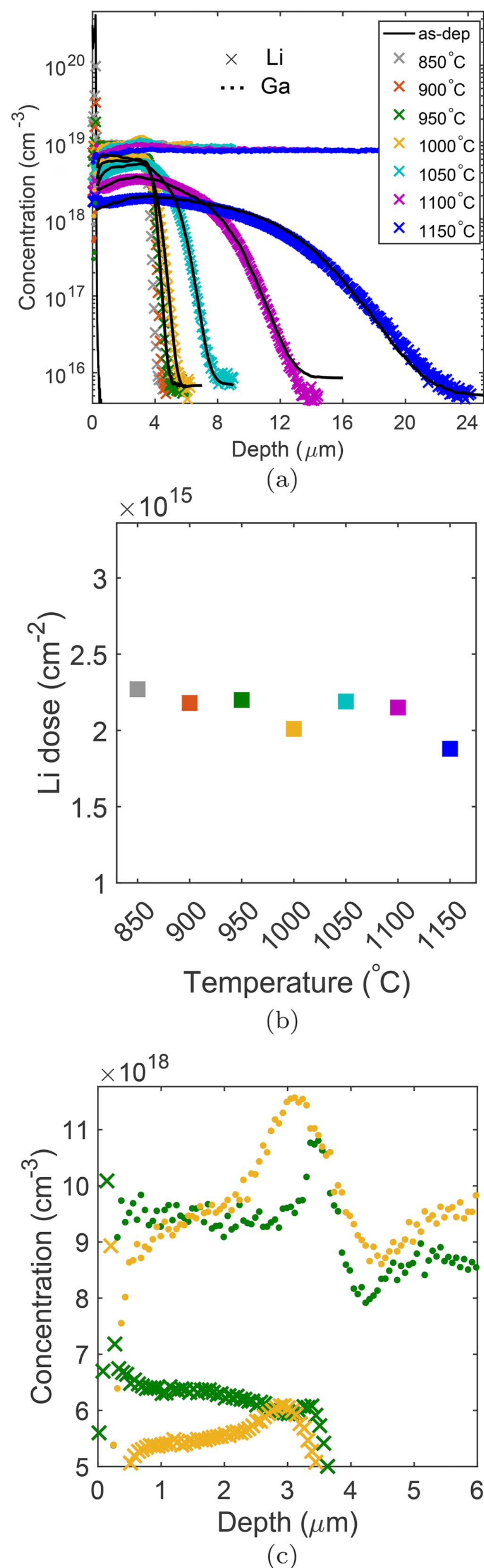

FIG. 2. (a) Experimental Li and Ga concentration vs depth profiles of sample B isochronally heat treated (30 min) at temperatures 850–1150 °C. The solid lines show the best fit of the reaction-diffusion model [Eq. (2)]. The integrated Li concentration within the Li depth profiles is shown in (b), and (c) shows a zoomed view of the junction region for the 950 and 1000 °C profiles (others excluded for clarity).

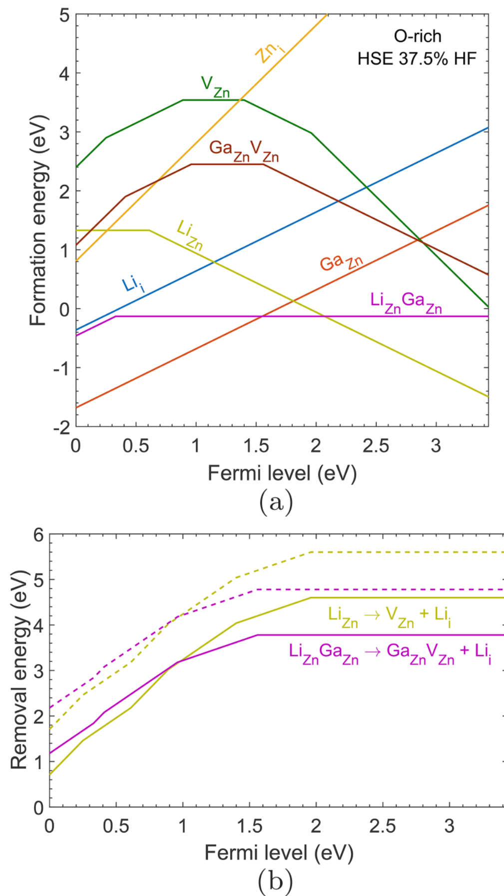

FIG. 3. (a) Predicted formation energies as a function of Fermi-level position for typical defects present in Li- and Ga-doped ZnO. (b) The resulting energy required to remove Li from the Zn-site to the interstitial site, with or without Ga_{Zn}^+ as a next nearest neighbor, as represented by the solid lines. The dotted lines show the overall dissociation energy, which include the migration barrier of ~ 1 eV for the diffusion of Li_i^+.

ϵ_F. Here, E_r is defined as the energy required to convert the substitutional Li to an interstitial position, but not completely dissociate, which also necessitates the inclusion of the smallest migration barrier for the involved constituents, i.e., the migration of either Li_i, V_{Zn}, or $Ga_{Zn}V_{Zn}$. From Fig. 3(b), $E_r(Li_{Zn}^-) = 4.6\,eV$ and $E_r[(Li_{Zn}Ga_{Zn})^0] = 3.8\,eV$ in the n-type ZnO, with the respective E_d being ~ 1 eV higher when considering the previously reported migration barrier of Li_i^+ (see Ref. 1), provided that Li_i^+ leave behind the V_{Zn}-related defect. It is interesting to note that, at highly compensated conditions (ϵ_F pinned close to mid-bandgap), $(Li_{Zn}Ga_{Zn})^0$ is the most energetically favorable configuration. However, the dominating trap for Li_i^+ strongly depends on the availability of the isolated vacancy vs the donor-vacancy pair.

2. Reaction diffusion model

Motivated by the above indications of V_{Zn}^{2-} or $(Ga_{Zn}V_{Zn})^-$ being involved in the diffusion of Li, the experimental diffusion data in Fig. 2(a) have been analyzed using a reaction-diffusion model[9,10,27] assuming a dissociative diffusion mechanism. The diffusion of Li assisted by V_{Zn}-related defects (X) can be described by reaction-diffusion equations (see, e.g., Refs. 9, 10, and 27–31 for a similar and general treatment)

$$\frac{\partial C_X}{\partial t} = K C_{V_{Zn}} C_{Li_i} - \nu C_X,$$
$$\frac{\partial C_{Li_i}}{\partial t} = D_{Li_i}\frac{\partial^2 C_{Li_i}}{\partial x^2} - \frac{\partial C_X}{\partial t}, \tag{2}$$

where $\nu = \nu_0 e^{-E_d(X)/k_B T}$ is the dissociation rate for X [i.e., either Li_{Zn}^- or $(Ga_{Zn}Li_{Zn})^0$], with ν_0 being the attempt frequency (on the order of $\sim 10^{13}\,s^{-1}$) and $E_d(X)$ the activation energy for dissociation of X. In Eq. (2), the reaction constant $K = 4\pi R_c D_{Li_i}$ is the formation rate of X, where R_c is the coulomb force assisted effective reaction radius set to 1 nm, and $D_{Li_i} = 2\times10^{-2}\exp(-0.98\,eV/k_BT)\,cm^2\,s^{-1}$ is the diffusivity of interstitial Li, as obtained by Lander,[1] and is used as a fixed parameter in the simulations. In Eq. (2), it is assumed that the formation of V_{Zn}^{2-} is the limiting process for the formation of $(Ga_{Zn}V_{Zn})^-$, i.e., $(Ga_{Zn}V_{Zn})^-$ forms instantaneously after the formation of V_{Zn}^{2-} at the studied temperatures, due to the high concentration of Ga_{Zn}^+. Thus, the diffusion model is not sensitive to whether Li is captured by V_{Zn}^{2-} or $(Ga_{Zn}V_{Zn})^-$. In the simulations, C_X is determined from the preceding Li-profile with the integrated concentration of the Li being constant, as seen in Fig. 2(b). That is, the flux of Li_i at the interface is set to zero (except for the 1150 °C, where a slight outdiffusion has been considered).

In order to solve the above RD equations [Eq. (2)], a value for $C_{V_{Zn}}(x,t)$ is required. Profiles of $C_{V_{Zn}}(x,t)$ can be estimated from DFT estimates of the V_{Zn}^{2-} formation energy in Fig. 3(a). That is, the distribution of V_{Zn}^{2-} can be expressed as[9,27]

$$C_{V_{Zn}}(x,t) = N_s e^{-[E_f(V_{Zn}^{2-})/k_BT]}\left(\frac{n(x,t)}{N_c(T)}\right)^2, \tag{3}$$

where N_s is the number of substitutional zinc lattice sites, $n = C_{Li_i} - 2C_{V_{Zn}} + C_{Ga_{Zn}}$ accounts for the net charge carrier concentration of the system with $C_{Ga_{Zn}} \approx C_{Ga} - C_X$, and N_c is the effective density of states in the conduction band. This implies that an instantaneous equilibrium of $C_{V_{Zn}}$ is established and governed by ϵ_F. The vacancy formation energy can then be expressed as $E_f(V_{Zn}^{2-}) = E_{f,0}(V_{Zn}^{2-}) - 2\epsilon_F$, where $E_{f,0}(V_{Zn}^{2-})$ is the formation energy at the valence band edge, set to 6.9 eV in our simulations as obtained from Fig. 3(a) and also guided by previous DFT reports.[21,32–34] For a more detailed discussion of the reaction-diffusion model used in this work, see Refs. 9, 10, and 27.

The considerations above leave only the dissociation rate ν as the unknown fitting variable to solve Eq. (2). Figure 4 shows the extracted ν vs the inverse absolute temperature, obtained from the best fits of the experimental data in Fig. 2(a). This results in a dissociation energy of 4.6 ± 0.2 eV with a prefactor of $\nu_0 = 5\times10^{15}\,s^{-1}$ for the diffusion of Li. Using the relation for Gibb's free energy $G = H - TS$, with an enthalpy H and entropy S, the dissociation rate can be expressed as $\nu = \nu_0 e^{-G/k_BT} = \Gamma_0 e^{S/k_B} e^{-H/k_BT}$, where $\Gamma_0 \approx 10^{13}\,s^{-1}$ is the characteristic frequency of the lattice. Thus, the high value obtained for ν_0 may suggest a contribution from the entropy (S) for the dissociation process. In this

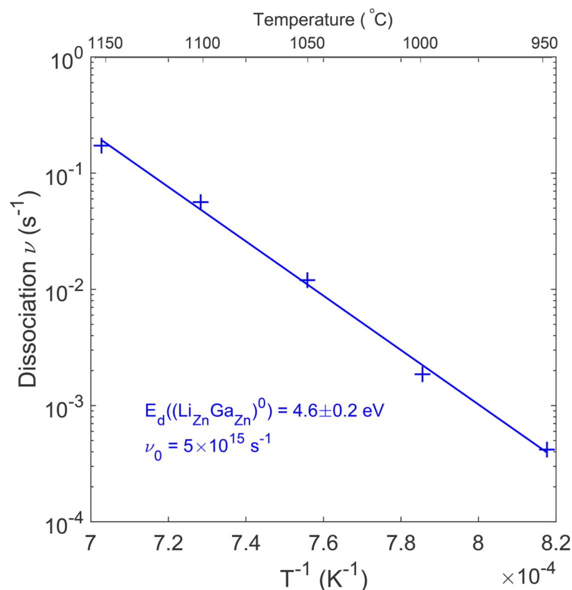

FIG. 4. Dissociation frequencies $\nu_{Li_{Zn}Ga_{Zn}}$, as a function of the inverse absolute temperature.

regard, previous experimental studies of Ga-doped ZnO[27,35] show that Ga-doping strongly enhances the Zn self-diffusion in ZnO and, in particular, that the diffusion prefactor scales with the Ga-concentration. These results, supported by the present study, indicate that the presence of Ga in the ZnO lattice affects the vibrational entropy, thus enhancing the diffusivity of both intrinsic- and impurity related defects. It can also be mentioned that theoretical studies of silicon carbide have previously shown that the entropy contribution for self-diffusion is significant at high temperatures ($\sim 0.6T_m$, where T_m is the melting temperature),[36] suggesting that such effects may also be important for other material systems at comparable conditions.

By comparing the extracted value of 4.6 ± 0.2 eV (Fig. 4) with the DFT results in Fig. 3(b), this excludes the possibility that Li_{Zn}^- is the dissociating defect, as this would imply a migration barrier for either Li_i or V_{Zn} that is close to zero (i.e., the dissociation energy is the sum of the removal and migration barriers). On the other hand, this result is in excellent agreement with the sum of the migration barrier of Li_i^+ of ~ 1 eV and the energy barrier of 3.8 eV as found from the DFT results in Fig. 3(b) for the removal of Li from $(Li_{Zn}Ga_{Zn})^0$. Hence, we conclude that $(Li_{Zn}Ga_{Zn})^0$ is the dominating Li-related defect in Li- and Ga-doped ZnO.

IV. CONCLUSION

Diffusion of Li in the single crystal Ga-doped ZnO is experimentally demonstrated to depend on the concentration and distribution of Ga. Indiffusion of Li at temperatures from 500 °C up to 800 °C from a Li-doped ZnO deposited film into n^+ ZnO yields an abrupt and compensated Li-doped box region with a Li concentration matching the as-grown free-electron concentration. The diffusion of Li is well described by employing a reaction-diffusion model that accounts for the presence of both Li and Ga. Using previous experimental results[1] for the Li_i^+ migration barrier, we obtain an activation energy of 4.6 ± 0.2 eV with a prefactor of $\nu_0 = 5 \times 10^{15}$ s^{-1} for the dissociation process mediating for the Li diffusion. This is in excellent agreement with our DFT results predicting an energy of 4.8 eV for the dissociation of $(Li_{Zn}Ga_{Zn})^0$ into Li_i^+ and $(Ga_{Zn}V_{Zn})^-$, thus evidencing $(Li_{Zn}Ga_{Zn})^0$ to be the assisting defect for the dissociative diffusion of Li.

ACKNOWLEDGMENTS

We thank H. N. Riise for the growth of the sputter-deposited film. Financial support from the Research Council of Norway for funding of the FUNDAMENT (No. 151131, Fripro Toppforsk program), DYNAZOx-project (No. 221992), Salient (No. 239895), the University of Oslo, and the Norwegian Micro- and Nano-Fabrication Facility (No. NorFab 245963) are gratefully acknowledged.

[1] J. J. Lander, J. Phys. Chem. Solids **15**, 324 (1960).
[2] P. T. Neuvonen, L. Vines, A. Y. Kuznetsov, B. G. Svensson, X. Du, F. Tuomisto, and A. Hallén, Appl. Phys. Lett. **95**, 242111 (2009).
[3] L. Vines, E. V. Monakhov, R. Schifano, W. Mtangi, F. D. Auret, and B. G. Svensson, J. Appl. Phys. **107**, 103707 (2010).
[4] K. M. Johansen, A. Zubiaga, I. Makkonen, F. Tuomisto, P. T. Neuvonen, K. E. Knutsen, E. V. Monakhov, A. Y. Kuznetsov, and B. G. Svensson, Phys. Rev. B **83**, 245208 (2011).
[5] M. G. Wardle, J. P. Goss, and P. R. Briddon, Phys. Rev. B **71**, 155205 (2005).
[6] A. Carvalho, A. Alkauskas, A. Pasquarello, A. K. Tagantsev, and N. Setter, Phys. Rev. B **80**, 195205 (2009).
[7] K. E. Knutsen, K. M. Johansen, P. T. Neuvonen, B. G. Svensson, and A. Y. Kuznetsov, J. Appl. Phys. **113**, 023702 (2013).
[8] D. G. Thomas, J. Phys. Chem. Solids **3**, 229 (1957).
[9] K. M. Johansen, L. Vines, T. S. Bjorheim, R. Schifano, and B. G. Svensson, Phys. Rev. Appl. **3**, 024003 (2015).
[10] T. N. Sky, K. M. Johansen, H. N. Riise, B. G. Svensson, and L. Vines, J. Appl. Phys. **123**, 055701 (2018).
[11] W. Lin, K. Ding, Z. Lin, J. Zhang, J. Huang, and F. Huang, CrystEngComm **13**, 3338 (2011).
[12] A. V. Krukau, O. A. Vydrov, A. F. Izmaylov, and G. E. Scuseria, J. Chem. Phys. **125**, 224106 (2006).
[13] P. E. Blöchl, Phys. Rev. B **50**, 17953 (1994).
[14] G. Kresse and J. Hafner, J. Phys. Condens. Matter **6**, 8245 (1994).
[15] G. Kresse and D. Joubert, Phys. Rev. B **59**, 1758 (1999).
[16] G. Kresse and J. Hafner, Phys. Rev. B **47**, 558 (1993).
[17] G. Kresse and J. Furthmüller, Phys. Rev. B **54**, 11169 (1996).
[18] F. Oba, A. Togo, I. Tanaka, J. Paier, and G. Kresse, Phys. Rev. B **77**, 245202 (2008).
[19] D. C. Reynolds, D. C. Look, B. Jogai, C. W. Litton, G. Cantwell, and W. C. Harsch, Phys. Rev. B **60**, 2340 (1999).
[20] J. Albertsson, S. C. Abrahams, and Å. Kvick, Acta Cryst. B **45**, 34 (1989).
[21] Y. K. Frodason, K. M. Johansen, T. S. Bjørheim, B. G. Svensson, and A. Alkauskas, Phys. Rev. B **95**, 094105 (2017).
[22] S. B. Zhang and J. E. Northrup, Phys. Rev. Lett. **67**, 2339 (1991).
[23] C. Freysoldt, B. Grabowski, T. Hickel, J. Neugebauer, G. Kresse, A. Janotti, and C. G. Van de Walle, Rev. Mod. Phys. **86**, 253 (2014).
[24] Y. Kumagai and F. Oba, Phys. Rev. B **89**, 195205 (2014).
[25] C. Freysoldt, J. Neugebauer, and C. G. Van de Walle, Phys. Rev. Lett. **102**, 016402 (2009).
[26] H.-P. Komsa, T. T. Rantala, and A. Pasquarello, Phys. Rev. B **86**, 045112 (2012).
[27] T. N. Sky, K. M. Johansen, B. G. Svensson, and L. Vines, "Influence of Fermi level position on vacancy-assisted diffusion of aluminum in zinc oxide," Phys. Rev. B (to be published).
[28] E. Antoncik, Appl. Phys. A **56**, 291 (1993).
[29] H. Bracht, Phys. Rev. B **75**, 035210 (2007).
[30] M. Uematsu, J. Appl. Phys. **82**, 2228 (1997).
[31] U. M. Gosele, Ann. Rev. Mater. Sci. **18**, 257 (1988).

[32]A. Janotti and C. G. Van de Walle, Phys. Rev. B **76**, 165202 (2007).
[33]D. O. Demchenko, B. Earles, H. Y. Liu, V. Avrutin, N. Izyumskaya, Ü. Özgür, and H. Morkoç, Phys. Rev. B **84**, 075201 (2011).
[34]D. Steiauf, J. L. Lyons, A. Janotti, and C. G. Van de Walle, APL Mater. **2**, 096101 (2014).
[35]A. Azarov, V. Venkatachalapathy, Z. Mei, L. Liu, X. Du, A. Galeckas, E. Monakhov, B. G. Svensson, and A. Kuznetsov, Phys. Rev. B **94**, 195208 (2016).
[36]E. Rauls, T. Frauenheim, A. Gali, and P. Deák, Phys. Rev. B **68**, 155208 (2003).

Paper V

Local homoepitaxy of zinc oxide thin films by magnetron sputtering
H. N. Riise, V. S. Olsen, A. Azarov, A. Galeckas, T. N. Sky, B. G. Svensson, and E. Monakhov, Thin Solid Films, 601 (2016)

Thin Solid Films 601 (2016) 18–21

Contents lists available at ScienceDirect

Thin Solid Films

journal homepage: www.elsevier.com/locate/tsf

Local homoepitaxy of zinc oxide thin films by magnetron sputtering

H.N. Riise *, V.S. Olsen, A. Azarov, A. Galeckas, T.N. Sky, B.G. Svensson, E. Monakhov

Department of Physics, Center for Materials Science and Nanotechnology, University of Oslo, P.O. Box 1048, Blindern, N-0316 Oslo, Norway

ARTICLE INFO

Article history:
Received 1 June 2015
Received in revised form 22 August 2015
Accepted 11 September 2015
Available online 25 September 2015

Keywords:
Radio Frequency magnetron sputtering
Zinc oxide
Local homoepitaxy
Epitaxial growth

ABSTRACT

High quality zinc oxide (ZnO) thin films have been deposited on c-axis oriented (Zn-face) hydrothermally grown single crystal ZnO substrates by employing Radio Frequency magnetron sputtering at variable sputtering power densities. Structural and optical properties of the thin films show that at low sputtering power densities, the thin films grow homoepitaxially with a low defect density, while the higher impact energy of depositing atoms and ions at higher sputtering power densities induces damage to the growing film, and a strained, off-axis growth results. The surface morphology of the films reveals a 3D growth mode, and the observed homoepitaxy hence occurs locally inside the grains, i.e. local homoepitaxy.

© 2015 Elsevier B.V. All rights reserved.

1. Introduction

Zinc Oxide (ZnO) has been extensively studied for the past 25 years [1], and a significant driving force in this research has been the potential realization of blue Light Emitting Diodes and lasers based on excitonic photon emission. At least two considerable obstacles must be hurdled before such devices can materialize, namely p-type ZnO and inexpensive epitaxial growth of ZnO. Homoepitaxial growth of ZnO has been demonstrated on several occasions [2,3,4,5], but most reports involve the use of Molecular Beam Epitaxy or Metal-Organic Vapor Phase Epitaxy [6] techniques which are expensive and do not readily scale to industrial volumes. Sputter deposition is a common technique for large volume fabricating of ZnO thin films, and it provides a low-cost and reliable means for thin film deposition. However, sputter deposited ZnO films are commonly polycrystalline and grown on foreign substrates, leading to significant strain and small crystallites [7]. The presence of grain boundaries and strain fields inhibits charge carrier transport [8], and optoelectronic devices based on polycrystalline ZnO will hence suffer from low quantum efficiencies. Homoepitaxial sputter deposition of ZnO can overcome the challenges of both low quality films and upscaling [9,10], and in this work we investigate the characteristics of Radio Frequency (RF) magnetron sputter deposited homoepitaxial ZnO films as a function of the target power density applied during growth.

2. Experimental details

Highly resistive, c-axis oriented, hydrothermally (HT) grown single crystal ZnO substrates ($\rho \sim 1.4\cdot10^3$ Ωcm, 20 × 20 × 0.5 mm^3 in size) purchased from Tokyo Denpa Co., Ltd. were cut into sample sizes of approximately 5 × 5 × 0.5 mm^3 using a diamond scriber. Each sample was ultrasonically cleaned in acetone (5 min), isopropanol (5 min) and deionized water (5 min) and blown dry with N_2 immediately before being loaded into the magnetron sputtering chamber (Semicore Equipment Inc. Tri-axis Multi Source Sputtering System). The chamber was evacuated to a pressure $<2.7 \times 10^{-4}$ Pa and the ZnO substrate was subsequently heated to 400.0 ± 0.4 °C by four heating lamps situated underneath the substrate and kept at this temperature for 30 min prior to deposition. During deposition a constant Ar flow of 50.0 ± 0.2 SCCM was kept leading to a process pressure of 0.93 ± 0.01 Pa, while a nominally undoped 3″ ceramic ZnO target (99.99% purity) with a 10 ± 0.5 cm distance and 17 ± 1 ° inclination angle to the substrate was Radio Frequency (RF) sputtered at different power densities of 0.22, 0.67, 1.11, 1.54, 1.97 and 2.41 (±0.02) W/cm^2. The target was pre-sputtered for 10 min before the shutters were opened, and the ZnO substrate was rotated at 12 rpm to improve film thickness uniformity. As a result of a previous study investigating the influence of the substrate surface polarity on the homoepitaxial sputter deposition of ZnO, the ZnO thin films were deposited on single crystal Zn-face ZnO [11]. RCA cleaned Silicon (Si) was also loaded into the chamber and used for thickness estimation of the deposited films; photoresist (PR) was applied to half of the ZnO thin film deposited on Si, the exposed film was etched by 1:20 HCl:H_2O (vol%) and after removing the PR by acetone, the film thickness was measured by surface stylus profilometry (Veeco Dektak 8). However, the growth rate on Si and ZnO may differ significantly, and the Sodium (Na) concentration as a function of depth of the thin films grown on ZnO was used to determine their thickness. The Na distribution was ascertained by Secondary Ion Mass Spectrometry (SIMS) using a Cameca IMS 7f microanalyzer with 10 keV O_2^+-ions as the primary beam. The depth of the sputtered crater

* Corresponding author.
E-mail address: h.n.riise@fys.uio.no (H.N. Riise).

http://dx.doi.org/10.1016/j.tsf.2015.09.043
0040-6090/© 2015 Elsevier B.V. All rights reserved.

was measured by a Veeco Dektak 8 stylus profilometer and used to convert sputtering time to depth (assuming a uniform and time-independent erosion rate). A Na implanted reference sample was used to translate the measured signal to concentration.

Structural characteristics of the films were investigated by X-Ray Diffraction (XRD) using a Bruker AXS D8 Discover with Cu $K_{\alpha1}$ radiation ($\lambda = 1.54056$ Å) and Rutherford Backscattering Spectrometry in channeling mode (RBS/C) using a 1 MV tandem ion accelerator (National Electrostatics Corporation) with 1.6 MeV $^4He^+$ ions incident along the [0001] direction of ZnO backscattered into a detector set at an angle of 165° relative to the incident beam direction. Optical properties were determined by Photoluminescence (PL) spectroscopy employing a 325 nm wavelength continuous wave He–Cd laser with an output power of 10 mW as an excitation source while emission was collected by a microscope and directed to a fiber optic spectrometer (Ocean Optics USB4000, spectral resolution 2 nm). Atomic Force Microscopy (Veeco Dimension 3100) was utilized for surface morphology imaging.

3. Results

The measured thin film thicknesses and deposition rates from SIMS and etching evaluations are summarized in Fig. 1.

In the figure, the deposition durations of the individual samples are graphically presented on the top axis of the figure. The durations were selected in an attempt to maintain a constant film thickness and are related to the sputtering power densities by

$$Duration = \frac{219.3}{Power\ density}.$$

However, as can be seen in Fig. 1, the deposition rate on bulk ZnO does not appear to be proportional to the sputtering power and has a more complex dependence.

Fig. 2 displays the data obtained from RBS/C measurements for all the samples in the present study.

The dotted line corresponds to the sample deposited at 0.22 W/cm ^{2} measured in a random orientation (this random orientation spectrum is representative of the random orientation spectra of all the other samples in the study) while the full lines represent the measurements made in channeling orientation. The surface minimum yield of the samples deposited at 0.22 and 0.66 W/cm ^{2} is around 2%, a value matching the surface minimum yields of HT [12] and seeded vapor transport [13] grown single crystal ZnO indicating the same crystal perfection for the thin films as the substrate. The samples also show a linearity of the RBS yield with increasing channel number, indicating a good interface between the substrate and the film. This contrasts the spectra of the samples deposited at 1.11, 1.54, 1.97 and 2.41 W/cm ^{2} which all show a kink in the RBS yield around the expected thin film thicknesses (around Zn depth of 500 nm) revealing an offset in the [0001] direction of the films compared to the substrates. The higher RBS yields of the high sputtering power density films also show that more structural defects are present compared to that in the two low sputtering power density films.

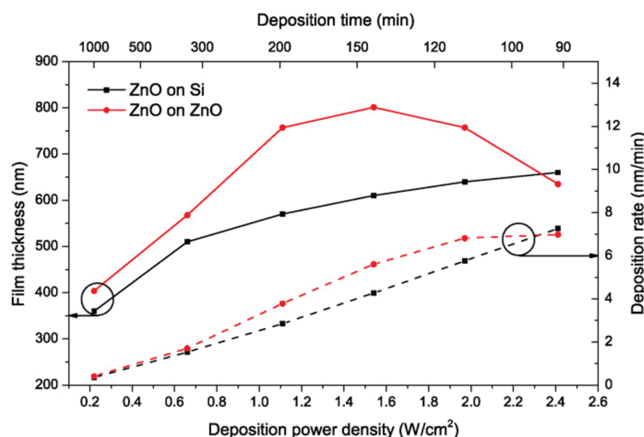

Fig. 1. ZnO thin film thickness (solid line) and deposition rate (dashed line) as a function of deposition power density. The top axis displays the deposition duration.

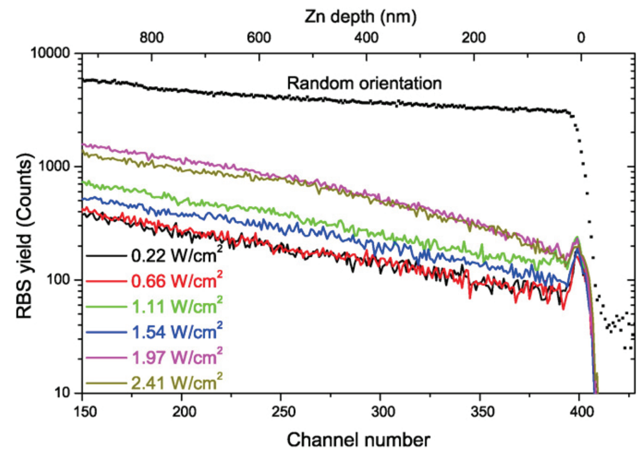

Fig. 2. RBS spectra of the investigated films. The low RBS yield of samples deposited at 0.22 W/cm ^{2} and 0.66 W/cm ^{2} indicate highly perfect and lattice matched thin films.

A similar conclusion can be made from analyzing the XRD results in Fig. 3, where locked coupled scans (Fig. 3(a)) and rocking curve scans (Fig. 3(b)) of the (0002) reflection of ZnO are shown. As for RBS/C, the sample deposited at 0.22 W/cm^2 has a crystal quality which matches the substrate (cf. the overlap of the substrate peak and the 0.22 W/cm ^{2} peak of Figs. 3(a) and (b)). At higher sputtering power densities, (i) the emergence of side peaks in the locked coupled scans evidencing strained thin film growth, and (ii) the increasing full width at half maximum (FWHM) of the rocking curves (46 arcsec for 0.22 W/cm ^{2} compared to 94 arcsec for 2.41 W/cm ^{2}), both corroborate the higher RBS yield of the high sputtering power density films. Further, the asymmetry of the rocking curve peaks at high sputtering power densities indicate an offset of the [0001] direction of the films compared to the substrate.

Indirect confirmation of the trends seen in RBS/C and XRD is provided by PL spectra of the Near Band Edge (NBE) emission region (Fig. 4) of the samples.

The intensity of the exciton peak of ZnO is highest and the FWHM of the peak is lowest for the sample deposited at 0.22 W/cm ^{2} while both parameters gradually degrade as the power density is increased. A higher NBE emission efficiency generally implies lower defect levels since a lower concentration of defect related non-radiative pathways promotes the radiative NBE emission. Thus PL results suggest that the defect densities in the thin films increase with the sputtering power density.

The results from RBS/C, XRD and PL all support that the crystal structure of the thin film deposited at 0.22 W/cm ^{2} is the same as that of the substrate, with no interface defects and a very low dislocation density. However, these techniques probe the sample in the c-direction of ZnO, i.e. in the growth direction of the films, and do not disclose information in the lateral dimension. An AFM image from the surface of the sample deposited at 0.22 W/cm ^{2} (Fig. 5) reveals small grains indicating that the film has not grown by a Frank–van der Merwe type growth mode (step-flow growth), but rather a Volmer–Weber growth mode or possibly Stranski–Krastanov growth mode (3D growth).

An XRD ϕ scan of the (1015) reflection of the film (not shown) exhibits double peaks separated by an angle less than 5° indicating that

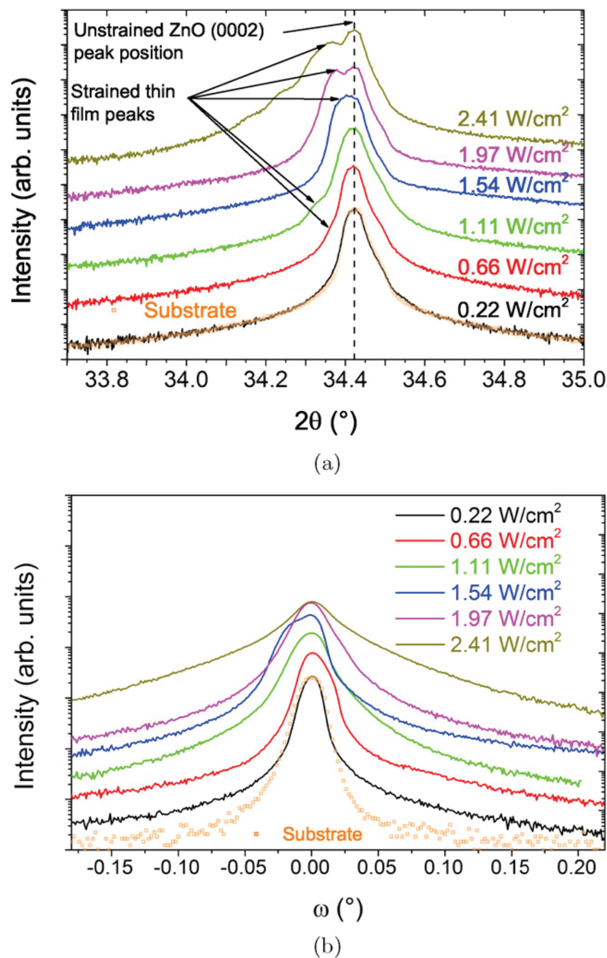

Fig. 3. In (a), XRD locked coupled scans of the (0002) reflection of ZnO reveal strained thin film growth at higher sputtering power densities while in (b), XRD rocking curve scans indicate a higher dislocation density and a tilt in the growth direction at higher sputtering power densities.

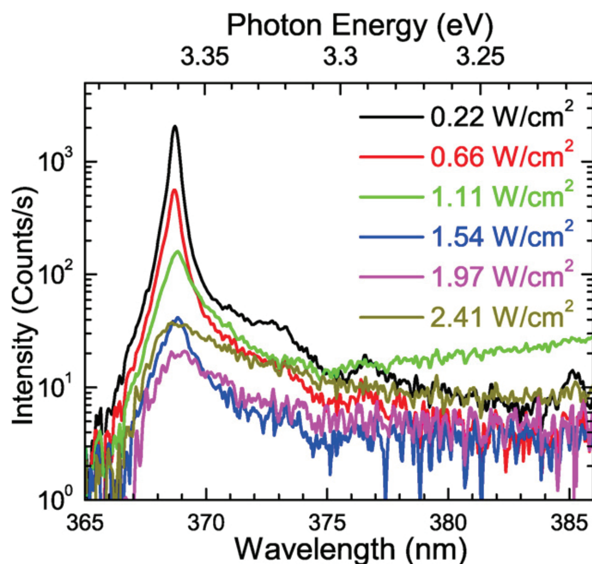

Fig. 4. PL spectra of ZnO films measured at 10 K. The excitonic emission around 365 nm is most pronounced for low sputtering power densities corroborating XRD and RBS/C.

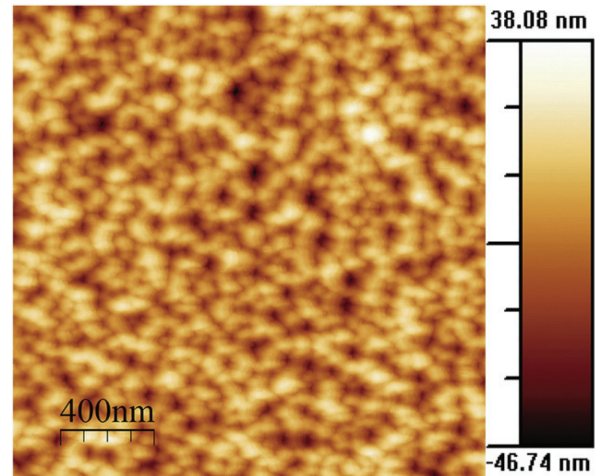

Fig. 5. AFM image of the sample deposited at 0.22 W/cm ^{2} revealing a 3D growth mode of the film. The Z-scale is given by the color scale on the right hand side of the figure.

the grains are rotated with respect to each other but with low angle grain boundaries. Notice also the hexagonal ordering of the grains in Fig. 5, which implies nucleation at lattice points on the surface of the substrate. The grain morphology and hexagonal ordering are retained at higher sputtering power densities albeit with an increasing lateral grain size.

4. Discussion

There is compelling experimental evidence, seen by RBS/C, XRD and PL, that the sputter deposited thin films indeed adopt the crystal structure of the ZnO substrate, at least at low sputtering power densities. At the same time, the thin films exhibit grain structures and a 3D growth mode as evidenced from AFM and phi scans; the data hence reveal that the homoepitaxy of the films occurs in local domains (grains) growing in columns along the [0001] direction, i.e. local homoepitaxy. With increasing sputtering power density, the lateral size of these grains grows, implying that atoms adsorbed on the surface (adatoms) have a higher mobility as the sputtering power density is increased. Accordingly, they are able to diffuse further distances on the surface and are more likely to attach to an already existing grain. The increasing grain size with sputtering power density indicates that the deposition energies are kept below the subplantation regime where the adatom mobility decreases since the impinging species are implanted a few atomic layers below the surface where they are immobile [14]. At low sputtering power densities, the adatoms have relatively low energies and surface mobilities, and are not able to diffuse far on the surface, leading to smaller grains. A high surface mobility of the adatoms promotes Frank–van der Merwe growth and high sputtering power densities do offer such a characteristic. However, the higher energy of the impinging atoms and ions introduces damage to the growing film, e.g. dislocations, strain and tilt of growth direction with respect to the substrate. Evidence of sputtering damage to the films at high sputtering power densities can be seen in Fig. 1 where the deposition rate saturates for the samples deposited at 1.97 and 2.41 W/cm^2 (an effect not seen for the ZnO thin films deposited on Si substrates) indicating resputtering of the deposited films.

5. Conclusions

ZnO thin films were deposited on HT grown ZnO single crystal substrates using RF Magnetron sputtering at elevated temperature. The films exhibit excellent crystal quality, with close lattice match between

the thin films and the substrate at low sputtering power densities. At higher sputtering power densities, damage is induced by the sputtered ions and atoms, and strained, mis-oriented growth results. From AFM imaging, a 3D growth mode is revealed indicating that the homoepitaxy observed for low sputtering power densities by RBS/C and XRD measurements occurs locally within the individual, columnar grains.

Acknowledgments

This work was performed within the Norwegian Research Centre for Solar Cell Technology (project number 460976), a Centre for Environment-friendly Energy Research cosponsored by the Norwegian Research Council (grant number 193829), and research and industry partners in Norway. Dr. V. Venkatachalapathy is gratefully acknowledged for his valuable help in interpreting the XRD data.

References

[1] Transparent conductive zinc oxide: basics and applications in thin film solar cells, in: K. Ellmer, A. Klein, B. Rech (Eds.), Springer Series in Materials Science, Springer, Verlag Berlin Heidelberg, 2008, http://dx.doi.org/10.1007/978–3–540–73612–7.

[2] D.C. Look, D.C. Reynolds, C.W. Litton, R.L. Jones, D.B. Eason, G. Cantwell, Characterization of homoepitaxial p-type ZnO grown by molecular beam epitaxy, Appl. Phys. Lett. 81 (10) (2002) 1830–1832, http://dx.doi.org/10.1063/1.1504875.

[3] I. Bisotto, C. Granier, S. Brochen, A. Ribeaud, P. Ferret, G. Chicot, J. Rothman, J. Pernot, G. Feuillet, Residual doping in homoepitaxial zinc oxide layers grown by metal organic vapor phase epitaxy, Appl. Phys. Express 3 (2010), 095802, http://dx.doi.org/10.1143/APEX.3.095802.

[4] H. Kato, M. Sano, K. Miyamoto, T. Yao, Homoepitaxial growth of high-quality Zn-polar ZnO films by plasma-assisted molecular beam epitaxy, Jpn. J. Appl. Phys. 42 (Part 2) (2003) L1002–L1005, http://dx.doi.org/10.1143/JJAP.42.L1002.

[5] S. Heinze, A. Krtschil, J. Bläsing, T. Hempel, P. Veit, A. Dadgar, J. Christen, A. Krost, Homoepitaxial growth of ZnO by metalorganic vapor phase epitaxy in two-dimensional growth mode, J. Cryst. Growth 308 (1) (2007) 170–175, http://dx.doi.org/10.1016/j.jcrysgro.2007.07.024.

[6] R. Triboulet, J. Perriere, Epitaxial growth of ZnO films, Prog. Cryst. Growth Charact. Mater. 47 (2003) 65–138, http://dx.doi.org/10.1016/j.pcrysgrow.2005.01.003.

[7] U. Özgür, Y.I. Alivov, C. Liu, A. Teke, M.A. Reshchikov, S. Dogan, V. Avrutin, S.J. Cho, H. Morkoç, A comprehensive review of ZnO materials and devices, J. Appl. Phys. 98 (4) (2005), 041301http://dx.doi.org/10.1063/1.1992666.

[8] K. Ellmer, G. Vollweiler, Electrical transport parameters of heavily-doped zinc oxide and zinc magnesium oxide single and multilayer films heteroepitaxially grown on oxide single crystals, Thin Solid Films 496 (2006) 104–111, http://dx.doi.org/10.1016/j.tsf.2005.08.269.

[9] A. Bikowski, K. Ellmer, A comparative study of electronic and structural properties of polycrystalline and epitaxial magnetron-sputtered ZnO:Al and $Zn_{1-x}Mg_xO$:Al Films — origin of the grain barrier traps, J. Appl. Phys. 114 (2013), 063709http://dx.doi.org/10.1063/1.4817376.

[10] I.-S. Kim, S.-H. Jeong, B.-T. Lee, Growth and characterization of high quality homoepitaxial ZnO films by RF magnetron sputtering, Semicond. Sci. Technol. 22 (2007) 683–686, http://dx.doi.org/10.1088/0268–1242/22/6/017.

[11] R. Schifano, L. Vines, A. Azarov, V. Venkatachalapathy, H. N. Riise, B. G. Svensson, K. Chan, J. Wong-Leung, Single crystal homoepitaxial ZnO films grown by RF-magnetron sputtering, Unpublished.

[12] A.Y. Azarov, A. Hallen, X.L. Du, P. Rauwel, A.Y. Kuznetsov, B.G. Svensson, Effect of implanted species on thermal evolution of ion-induced defects in ZnO, J. Appl. Phys. 115 (2014), 073512http://dx.doi.org/10.1063/1.4866055.

[13] E. Rita, E. Alves, U. Wahl, J. Correia, T. Monteiro, M. Soares, A. Neves, M. Peres, Stability and luminescence studies of Tm and Er implanted ZnO single crystals, Nucl. Instrum. Methods Phys. Res., Sect. B 242 (1) (2006) 580–584, http://dx.doi.org/10.1016/j.nimb.2005.08.106.

[14] Y. Lifshitz, R. Edrei, A. Hoffman, E. Grossman, G. Lempert, J. Berthold, B. Schultrich, H. Jäger, Surface roughness evolution and growth mechanism of carbon films from hyperthermal species, Diam. Relat. Mater. 16 (2007), 17711776, http://dx.doi.org/10.1016/j.diamond.2007.07.019.